Laboratory Assessment of Scour Evolution Around Engineered Logjams in Gravel Bed Rivers

A Thesis Presented for the

Master of Science

Degree

The University of Tennessee, Knoxville

Adam Thomas Merook

May 2018

Acknowledgements

First, I wish to thank my adviser Dr. Thanos Papanicolaou for his wealth of experience, knowledge, and patience through the completion of this project. His mentorship has assisted in a multitude of ways, and I did not know that I would learn this much when setting out on this task. Second, I wish to thank those at HSL who spent many hours helping me understand and grow as an experimentalist, most of all Dr. Achilleas Tsakiris and Micah Wyssman. Third, I wish to thank Sevin Mohammadi and the resident undergraduates who were always around to lend a hand when needed and were genuinely curious about the project as they assisted in experiments and data analysis. Last, I wish to give my full gratitude to my friends, family, and colleagues who provided advice, encouragement, and a sounding board for all of my ideas. I could not have finished without them.

Abstract

Engineered logjams (ELJs) are permeable flow deflection structures increasingly utilized by transportation and river restoration practitioners to stabilize banklines, protect roadways, and improve aquatic habitat. Localized flow acceleration near hydraulic structures causes clearwater bed scour at ELJs; prediction of associated scour extents is needed to ensure structure and river stability. Although many studies focus on sand-bed scour approximations at the maximum equilibrium condition, increasing focus is being given to scour processes in non-uniform beds, at permeable structures, and for scour evaluations prior to equilibrium. Critical needs still lie, however, in relating the simultaneous evolution of scour, velocity, and bed shear stress in non-uniform beds at permeable ELJ installations. The overarching goal of this research is to provide a fundamental understanding of the scour hole evolution around a permeable ELJ structure in gravel bed rivers under clearwater conditions. The study shows that the ELJ structure deflects conical scour hole formation away from the structure nose. The scour hole evolution rate is found to be governed by the interlocking of particles (i.e. the gradation of particles affects interlocking). This research utilizes non-intrusive flow and scour measurement techniques providing aerial velocity and scour volume information around the ELJ. The basis of this study is the hypothesis that the rate of scour evolution is not only dictated by the gradation of particles, but also by the feedback between the gravel-bed matrix, the structure, and the flow. It is the three-way interaction that is encapsulated in the development of a decay function that relates shear stress decay with scour hole development. Analysis of the decay function informs the development of a parametric function for maximum scour depth estimation. The overall findings of this research can guide future efforts of practitioners to determine critical conditions for clearwater scour and ultimately the life-expectancy of these structures. More research is needed to extend estimation of scour under live-bed conditions in gravel-bed rivers for permeable structures, while also enhancing the proposed scour evolution formula to incorporate measure of turbulent strength around the structure for the area, intensity, and frequency of key vortical structure developing around an ELJ structure.

Table of Contents

1. Introduction 1
   - 1.1. Definition and use of engineered logjams 1
   - 1.2. Critical needs in research 4
   - 1.3. Critical literature review 5
   - 1.4. Interactions between structure and flow 6
   - 1.5. Interactions between flow and sediment 7
   - 1.6. Research limitations 9
2. Study overview 11
   - 2.1. Scope 11
   - 2.2. Objectives 11
3. Flume set-up 12
   - 3.1. Infrastructure and construction 12
   - 3.2. Flow quality 16
4. Case study of the prototype ELJ 22
   - 4.1. Prototype hydrologic and bathymetric information 22
   - 4.2. Prototype mobile bed sediment 26
   - 4.3. Prototype ELJ architecture 28
5. Physical model design 32
   - 5.1. Model mobile bed sediment 32
   - 5.2. Model dolotimber design 34
6. Experimental methodology 42
   - 6.1. Critical condition 42
   - 6.2. Clearwater experimental procedure 42
   - 6.3. Frozen bed velocity measurements 43
   - 6.4. Sonar continuous depth measurements 48
   - 6.5. Semi-continuous velocity measurements 50
7. Results 55
   - 7.1. Qualitative flow structure 55
   - 7.2. Equilibrium scour hole geometry 55
   - 7.3. Sonar continuous depth measurements 58
   - 7.4. Frozen bed velocity measurements 58
   - 7.5. Semi-continuous velocity measurements 58
8. Discussion 65
   - 8.1. Decay function formulation 65
   - 8.2. Formulation of gravel bed scour equation 66
9. Conclusions 71
   - 9.1. Observations 71
   - 9.2. Future work 71

Bibliography 73

Appendix 86

- Appendix A: Prototype dolotimber ELJ details 87
- Appendix B: Model dolotimber ELJ details 94
- Appendix C: Equilibrium clearwater scour results 96
- Appendix D: LSIV results 101
- Appendix E: Decay function calculations 118

Vita 119

List of Tables

Table 4.1. Hydrologic evaluation of Skagit River flood frequency.

Table 4.2. Prototype flow conditions for 2-year and 10-year events.

Table 4.3. Prototype log component volumes respective of dolotimber type.

Table 4.4. Prototype ballast component volumes respective of dolotimber type.

Table 4.5. Prototype dolo component volumes from dimensioned construction drawings.

Table 4.6. Prototype ELJ3 layering detail.

Table 4.7. Prototype ELJ3 component breakdown and porosity.

Table 7.1. Abbreviated test condition and scour results from Trials 1-5.

Table 7.2. Comparison table of ADV and LSIV velocity magnitudes at same location.

Table 8.1. Measurements of scour depth and shear stress over duration of experiment.

Table 8.2. Summary table of model results related to prototype scour conditions and results.

Table 8.3. By-trial model testing conditions and associated results**.**

Table A.1. Prototype ELJ1 layering detail.

Table A.2. Prototype ELJ2 layering detail.

Table A.3. Prototype Revetment 1 layering detail.

Table A.4. Prototype Revetment 2 layering detail.

Table A.5 Prototype Revetment 3 layering detail**.**

Table A.6. Prototype Revetment 1 component breakdown and porosity.

Table A.7. Prototype Revetment 2 component breakdown and porosity.

Table A.8. Prototype Revetment 3 component breakdown and porosity.

Table A.9. Prototype ELJ1 component breakdown and porosity.

Table A.10. Prototype ELJ2 component breakdown and porosity.

Table B.1. Calculations of structure component percentage between prototype and model for ELJ1.

Table B.2. Calculation of structure component percentage between prototype and model for ELJ2.

Table B.3. Calculation of model revetment porosity with proxy gravel.

Table C.1. Summary table of scour equilibrium conditions for sonar trial.

Table C.2. Summary table of scour equilibrium conditions for infrared trial.

Table E.1. Decay function calculations.

List of Figures

Figure 1.1. Standard concrete dolo, with textured surface. Human for scale (NHC, 2010).

Figure 1.2. Bankline ELJ, with inclusion of logs and other LWM (NHC, 201).

Figure 1.3. Illustration of developed vortical microstructures near a bridge abutment (after Kwan, 1988).

Figure 3.1. Plan view of flume centrifugal pump.

Figure 3.2. Flume control panel featuring digital displays and adjustment toggles.

Figure 3.3. Flume inlet with rectangular grates and cobble bed entrance to promote uniform flow.

Figure 3.4. Series of steel rods mounted on top of motorized tailgate for finer control of resistance.

Figure 3.5. Outlet step and sediment basket at end of test section.

Figure 3.6. Overhead trolley mounted to flume rails for mounting instrumentation.

Figure 3.7. Platform constructed in ELJ test section.

Figure 3.8. Platform constructed in ELJ test section, installed.

Figure 3.9. Gravel revetment with wire mesh support.

Figure 3.10. Clear plexiglass flume walls allow for side- and aerial-view optical access.

Figure 3.11. Dimensioned plan view of flume model setup.

Figure 4.1. Cross-sections taken from bathymetric GIS data for hydraulic calculations.

Figure 4.2. Prototype stage-discharge relationship at ELJ3.

Figure 4.3. HydroCalc software used to establish stage-discharge relationship at ELJ3.

Figure 4.4. Prototype grain size distribution (Cardno Entrix, 2011).

Figure 4.5. Construction plans for prototype ELJs and revetments (Cardno Entrix, 2011).

Figure 5.1. Grain size distribution comparison between model and prototype.

Figure 5.2. Dolotimber male mold design.

Figure 5.3. Dolotimber mold curing and splitting.

Figure 5.4. Filed final model dolos.

Figure 5.5. Model dolotimber configurations used in stacked matrix.

Figure 5.6. Model dolotimber matrix layout for ELJ3.

Figure 5.7. Oblique view of constructed ELJ3 model.

Figure 5.8. Plan-view of constructed model test section.

Figure 6.3. Frozen flat-bed bathymetry in gravel bed for ADV measurements.

Figure 6.4. Frozen scour bathymetry in gravel bed for ADV measurements.

Figure 6.5. Verification comparison of point gage and sonar results for equilibrium scour hole.

Figure 6.6. Profile view of sonar location relative to ELJ and developed scour hole.

Figure 6.7. Hot water reservoir for supply during IR data collection.

Figure 6.8. Continuous, uniform hot water seeding during IR data collection.
Figure 6.9. IR camera mount for plan-view data collection at ELJ3.
Figure 6.10. Example of surface velocity vectors at one point in scour evolution.
Figure 7.1. Model ELJ3 dye test illustrating location of down flow, primary vortex, and wake vortices.
Figure 7.2. Model ELJ3 dye test illustrating shear layer formation and main core flow.
Figure 7.3. Model ELJ3 dye test showing down and porous flows that travel to wake area.
Figure 7.4. Raw and processed sonar depth returns for Trial 6 for (a) Probe 1, (b) Probe 2, (c) Probe 3, and (d) Probe 4.
Figure 7.5. Sonar data for temporal monitoring during scour evolution compared with point gage scour hole transect at equilibrium.
Figure 7.6. Measured ADV streamwise velocity values (cm/s) at select locations in test section pre-scour.
Figure 7.7. Measured ADV streamwise velocity values (cm/s) at select locations in test section at scour equilibrium.
Figure 7.8. Relative velocity distributions from IR and side-view of scour evolution (AU in m/s).
Figure 8.1. Decay Function of wall shear stress around permeable ELJs in gravel bed**.**
Figure 8.2. Decay function of wall shear stress around permeable ELJs in gravel bed including data of Li and Guo (2016).
Figure 8.3. Prototype discharge-stage relationship at ELJ3.
Figure C.1. Location of point gauge measurements in scour test section used in volume calculations.
Figure C.2. Scour contour plots of Trials 1 in ELJ test section.
Figure C.3. Scour contour plots of Trial 2 in ELJ test section.
Figure C.4. Scour contour plots of Trial 3 in ELJ test section.
Figure C.5. Scour contour plots of Trials 4 in ELJ test section.
Figure C.6. Scour contour plots of Trial 5 in ELJ test section.
Figure C.7. Scour contour plot of sonar trial in ELJ test section.
Figure C.8. Scour contour plot of IR trial in ELJ test section.
Figure D.1. LSIV results at 2.5 minutes elapsed.
Figure D.2. LSIV results at 6.25 minutes elapsed.
Figure D.3. LSIV results at 9.75 minutes elapsed.
Figure D.4. LSIV results at 13.5 minutes elapsed.
Figure D.5. LSIV results at 17 minutes elapsed.
Figure D.6. LSIV results at 21.25 minutes elapsed.
Figure D.7. LSIV results at 25.5 minutes elapsed.
Figure D.8. LSIV results at 30 minutes elapsed.

Figure D.9. LSIV results at 35 minutes elapsed.
Figure D.10. LSIV results at 40 minutes elapsed.
Figure D.11. LSIV results at 44 minutes elapsed.
Figure D.12. LSIV results at 50 minutes elapsed.
Figure D.13. LSIV results at 57 minutes elapsed.
Figure D.14. LSIV results at 65 minutes elapsed.
Figure D.15. LSIV results at 72 minutes elapsed.
Figure D.15. LSIV results at 80 minutes elapsed.
Figure D.16. LSIV results at 90 minutes elapsed.

Abbreviations

ADV	Acoustic doppler velocimetry
CFD	Computational fluid dynamics
ELJ	Engineered logjam
gpm	Gallon per minute
HP	Horsepower
LDV	Laser doppler velocimetry
LSIV	Large scale image velocimetry
LWM	Large woody materials
MTA	Multiple-transducer array
NHC	Northwest Hydraulic Consultants
PIV	Particle image velocimetry
RCO	Washington State Recreation and Conservation Office
RMSE	Root mean square error
USDA	United States Department of Agriculture
WSDOT	Washington State Department of Transportation

1. Introduction

1.1. Definition and use of engineered logjams

Traditional methods of river restoration and streambank erosion mitigation have relied on extensive vegetative plantings (Fetherston et al., 1995; Justice et al., 2017; Schultz et al., 1995), soil bioengineering (Eubanks and Meadows, 2002; Finney, 1993; Lewis 2000), and structural installation measures (Frissell and Nawa, 1992; Rosgen, 2001; Thompson, 2002) to prevent bank erosion and resulting channel migration that threatens important nearby infrastructure (roads, levees, etc.). Of these practices, the most common is the application of large riprap linings on streambank surfaces to anchor down substrate and dissipate erosive energy (Blodgett, 1986; Robinson, 2002; Shields et al., 1995). Although this approach has shown previous success, there are several negative effects on aquatic life associated with the construction and degradation of riprap lined revetments. Initial installation sometimes requires the driving of piles or other invasive techniques that introduce excessive noise into aquatic habitat (Bagočius, 2015). These riprap installations lack the natural resonance properties of organic riparian vegetation, with related construction activities inducing hearing loss and stress on aquatic life (Reyff, 2017; Smith, 2004). As well, these invasive techniques at times require dewatering that must be orchestrated in a way that does not interrupt seasonal spawning runs or similar migratory behavior (United States Department of Agriculture (USDA), 2007a). Economically, the riprap installations often prove to be more expensive over time as they require repeated repair after seasonal high flow events (Abbe et al., 1997; Cardno Entrix, 2011). Many of the installations do not solve the underlying problem of elevated velocity and shear stress at the bankline; many seek only to stop erosion by armoring the underlying substrate. When flows exceed the design velocity, the riprap mobilizes, causing increased erosion, bankline migration, increased turbidity, and destabilization of local gravel-beds that are paramount in the spawning cycle of egg-laying fish (e.g. salmon) native to gravel-bed rivers (Allen and Flecker, 1993; Kimmerer and Allan, 1982; Meffe, 1984; Montgomery, 1996; USDA, 2007b).

In an attempt to mimic natural rivers and utilize native components, a growing number of researchers and practitioners are utilizing wooden components and engineered logjams (ELJs) as a design alternative in streambank stabilization (Abbe et al., 1997; Bolton et al., 1998; Castro and Sampson, 2001). ELJs utilize interlocking components of wood, gravel, thatch, and root wads referred to as large woody materials (LWM) in order to form a porous barrier to flow that increases organic content in waterways and fortifies sensitive banks or channel bars. Unlike riprap and other solely concrete structures, ELJs limit acoustic resonance for local fish and increase quantity of interstitial spacing for biological growth and aquatic

habitat restoration, while simultaneously anchoring erodible channel features that would otherwise be degraded (Cedarholm et al., 1997; D'Aoust and Millar, 1999; House and Crispin, 1990). However, as many of these ELJ structures rely on their interlocking features for rigidity rather than their self-weight, many ELJs must also be constructed using driven piles in dewatered or diverted channels to sufficiently stack and key-in all elements securely (D'Aoust and Millar, 2000). Failure to do say may result in structural damage if a large storm event passes before sediments and other riparian materials have an opportunity to settle and bind the ELJ components. To combat these current deficiencies and provide a more longstanding solution, stream restoration practitioners have partnered with state departments and federal research initiatives to create an innovative new method for bank protection that integrates LWM with concrete "dolos" to create a multi-component dolotimber structure that provides both aquatic habitat and cost-savings while minimizing erosion (Figure 1.1). A standard dolo, sometimes also referred to as "dolosse", is an unreinforced pre-cast concrete, jack-like structure weighing over 8 tons and having protruding dimensions exceeding 8 feet; they are self-settling, interlocking, log-like structures that are heavy and have arm-like elements (Abbe et al., 2011). These dolos are stable and resist overturning, instead settling deeper into the substrate during local erosion rather than rolling or entraining like riprap. Due to their immense weight and arm-like protrusions, combinations of interlocking logs, root wads, and cobble ballasts can be combined to create complex habitat full of interstitial spacing that promotes ecological growth (Figure 1.2). The surface of the concrete dolos was painted and roughened to imitate tree bark in order to promote microbiological growth and diverse biota. The dolos were pre-cast and cured off-site by a specialty contractor such that the concrete was inert at the time of installation. As well, Cardno Entrix (2011) confirmed that no heavy metal components were used in the concrete mix. As well, utilizing these natural structural components in a modular manner decreases need for invasive construction practices (i.e. driving piles, dewatering) and unnatural building materials (i.e. riprap, steel) by allowing for in-stream installations via crane or excavator and utilization of local materials for improved habitat integration that may not be achieved otherwise with the use of traditional logjams designs. These design considerations overall yield substantial cost-savings related to materials, time, and permitting efforts (Abbe et al., 1997).

The Washington State Department of Transportation (WSDOT), in coordination with Native American entities, local governments, and conservation groups, has employed ELJs for bank protection and channel stabilization along highways and river crossings, while also installing them in areas to improve aquatic habitat in sensitive areas of predominantly gravel-bedded streams. Examples include installations in the Lower Cle Elum River to recruit natural wood downstream of Cle Elum Dam (Kittitas Conservation Trust, 2008), bank stabilization along the Hoh River bordering US 101 (Ward, 2006), the South Fork

Figure 1.1. Standard concrete dolo, with textured surface recreating natural roughness. Human for scale (Cardno Entrix, 2011).

Figure 1.2. Bankline ELJ, with inclusion of logs and other LWM (Cardno Entrix, 2011).

Nooksack for Chinook salmon spawning habitat restoration (Washington State Recreation and Conservation Office (RCO), 2011), the Lower Elwha River to restore critical salmon habitat (RCO, 2000), and the Cowlitz River to combat bank retreat and preserve remaining forest areas (Hall and Moler, 2006). These installations represent the growing implementation of ELJ construction standards and best management practices, evolving from a predominantly "experimental" methodology to an established bankline protection and river restoration practice. Installations at Germany Creek (Wild Fish Conservancy Northwest, 2012) and the Lower Puyallup River (Abbe et al., 2011) specifically exemplify the efficacy of the dolotimber ELJ design. Evaluations of these installations determined that they stabilized banklines near crucial transportation corridors (Abbe et al., 1997; McHenry et al., 2007; Montgomery and Abbe, 2006), increased the quantity and complexity of aquatic habitat by improving interstitial spacing and increasing natural wood in waters (Abbe and Montgomery, 1996; Abbe et al, 1997; Fetherston, 1995; McHenry et 1l., 2007), and allowed for potential of native floodplain riparian vegetation to re-root and accumulate wood (Abbe and Montgomery, 1996; Latterell, 2005). These structures, though debated on their aesthetic contribution to rivers, have garnered a growing amount of public attention and curiosity, signaling that these creative structures may be utilized in an increasing number of river restoration where applicable (Hall and Moler, 2006).

1.2. Critical needs

A literature review by Papanicolaou et al., (2017) and a publication from the National Academy of Science (Ettema et al., 2011) on clearwater scour identify the following critical research gaps;

(1) There is lacking depth of research on scour in gravel-bed rivers around hydraulic structures compared to the wealth of studies completed in sand beds. Current formulas predicting scour evolution around hydraulic structures are mostly applicable in sand-bed rivers, and, to a lesser extent, for cohesive sediment beds. These formulas tend to over-predict the volume of scour hole as they do not account for the interlocking developed between gravel-bed particles. Also, the existing formulas do not consider the near-bed turbulence that is manifested atop a gravel bed and the role of turbulence on the entrainment and pick-up of particles. This work will address this critical need by developing a scour formula that is applicable for clearwater scour prediction in gravel-bed rivers.

(2) The majority of scour measurements in any river bed type is done incrementally in time and usually performed at a fixed location. There is a very limited number of continuous measurements of scour volume evolution that is scour volume change with respect to time (Guan et al., 2016 or latest pub). This research will address this limitation by performing continuous measurement of scour hole evolution using

an array of mini-sonar probes. This mini-sonar technology works in laboratory settings at a minimal flow depth of 3 cm and relates sonar beam frequency to distance.

(3) There are limited flow measurements in the vicinity of the toe of a hydraulic structure. The majority of those measurements are focused at a single point and provide the average properties of velocity and stress. There is a need to perform aerial measurements using the particle image velocimetry technology (PIV). The PIV technology encapsulates the flow field within the scour hole area. Synchronizing this aeriel flow measurement with the mini-sonar scour hole measurement will provide unique insights of the feedbacks between scour hole, flow, and structure on a continuous basis. In this study, we use the state of the art infrared (IR) technology to capture flow field changes with time and analyze the IR images with the large-scale image velocimetry (LSIV) software developed at the Iowa Institute of Hydraulic Research (IIHR).

(4) Most of current scour hole formulas predict a maximum depth at what is usually presumed to be the equilibrium condition. However, very few formulas can predict the volume scoured at different time increments and relate this information to the decay of the shear stress. Li (2014) has shown that as the scour hole evolves, the bed shear stress acting on a particle reduces as form roughness increases. This study, for the first time, provides a decay function for the bed shear stress and compares the gradient of the function for the bed shear stress with the gradient of the scour volume with time.

These critical needs are discussed below in Section 1.3 in greater detail.

1.3. Critical literature review

Although there have been numerous studies completed discussing flow around different hydraulic structures spanning back throughout the 20th Century, thematic focus is shifting from considering only time-averaged flow relationships to a more complete temporal scour evolution accounting for the non-uniformity and unsteady nature of flows as it relates to fluctuations in bed shear stress, scour capacity, and scour volume over time (Fox et al., 2005; Kuhnle et al., 2002; Oliveto and Hager 2002; Raudkivi and Ettema, 1983; Whitehouse, 1997). While a larger fraction of these studies primarily consider these spatiotemporal changes in sand -sized mobile beds (Coleman et al., 2003; Dey and Barbhuiya, 2004; Giri and Shimizu, 2005), a growing number of experiments are highlighting temporal scour depth evolution in mobile bed consisting of non-uniform sediment sizes and different particle densities to more closely capture the non-uniform particle size, grain interlocking, and bed armoring that predominates gravel bedded rivers (Barbhuiya and Dey , 2004; Kothyari et al., 1992; Kuhnle, 1993; Landers and Mueller, 1996; Raudkivi, 1986; Raudkivi and Ettema, 1983; Su and Lu, 2016). Furthermore, reliable scour depth prediction equations are often formulated around established construction practices like regularly-shaped,

impermeable bridge piers and abutments (Melville, 1993; Melville and Coleman, 2000). Many experiments focused on scour depth around irregularly-shaped structures (especially those with increased volumes of voids and wooden components) are simplistic in nature, limiting the direct comparability to complex field installations containing hundreds of elements in dozens of modular installations (Beschta, 1983; Cherry and Beschta, 1989; Svoboda and Russell, 2011; Wallerstein et al., 2001). Two primary causes for inaccuracies of scour depth predictions in gravel-bedded rivers around permeable ELJ structures include: 1) the mischaracterization of flow fields around ELJs due to oversimplifying experimental assumptions, and 2) the focus on the geomorphologic equilibrium state without enough consideration of the temporal evolution of scour depth and volume that may lead to costly overdesign.

An increasing number of studies have focused on the distribution of velocity near hydraulic structures (Ahmed and Rajaratnam, 2000; Dey and Barbhuiya, 2005), with some computational fluid dynamics (CFD) simulations having successfully characterized velocity and shear stress around these structures (Lai et al., 2017; Li and Guo, 2016). However, the geometric dolotimber irregularities, structure permeability, and gravel substrate associated with the dolotimber ELJs present new challenges for physical and numerical modeling to properly characterize the effects of roughness, porosity, and drag as they effect scour evolution (Fox et al., 2005; Galisdorfer et al., 2014; Manners et al., 2007; Shields and Gippel, 1995).

Once these structures are more accurately characterized in physical models and the scour phenomenon over time is addressed in greater detail, it is expected that numerical models may be developed with increasing complexity and accuracy and will further develop scour formulas that do not underestimate scour depth around these permeable hydraulic structures.

The sections that follow below elaborate on the current knowledge on interactions of flow, structures, and sediment while also detailing the current experimental limitations.

1.4. Interaction of structure and flow

Quantitative studies on hydraulic structures at river banks (weirs, barbs, and traditional ELJs) have been completed to further understanding on how flow interacts with structures of different shape, relative submergence, and porosity (Bennett et al., 2015; Koken & Constantinescu, 2014; Leu et al., 2008). Ultimately, it has been established that the primary flow structures pertinent to the understanding of flow around a dolotimber ELJ include the main core, the shear layer, and the wake region (Fox et al., 2005). Other works (Barbhuiya and Dey, 2003; 2004; Koken and Constantinescu, 2014) have described in great detail the microstructures of flow around bankline hydraulic structures in these regions as a system of vortices and eddies that develop on the upstream section, the structure tip, and behind the structure. Back

eddies form on the upstream face of the structure as flow is deflected backwards and downward towards the bed in a diving manner. The diving energy from this interaction merges with the acceleration of flow around the structure to form the primary/horseshoe vortices in the main core region that results in jettisoned stream tubes focused at the structure toe and associated scour potential (Koken and Constantinescu, 2014; Coleman at al., 2003). Secondary vortices may occur outside of the primary vortex as the constricted streamlines near the structure interact with the bulk streamlines further into the channel, creating a shear layer against the predominant primary vortex (Melville and Coleman, 2000). Downstream of the structure, wake vortices are prominent as flow is separated at both the upstream and downstream corners of the abutment (Barbhuiya and Dey, 2004). An illustration of these microstructures forming near an abutment can be seen in Figure 1.3.

These flow structure become increasingly complex, however, when considering the permeable nature of dolotimber-based ELJs and the protruding elements that alter roughness and localized acceleration (Abbe et al. 1997; Cardno Entrix, 2011; Shields and Gippel, 1995). The interstitial spacing allows for some smaller amount of flow to travel through the ELJ itself, decreasing the magnitude of backwater effects and velocity stagnation relative to that of an impermeable structure of the same geometry. As well, the increase in roughness (and therefore drag) associated with protruding dolotimber arms and log extensions can disrupt the localized acceleration in the vicinity of the ELJ. This decrease in adverse pressure gradient, paired with the dampening of localized acceleration, may inhibit the erosive power of the horseshoe/primary vortex created by downflow on the upstream side of the ELJ (Koken and Constantinescu, 2014). This decrease in primary vortex strength also leads to weakening of the antagonistic secondary vortex and decreased flow separation responsible for the wake vortices, resulting in reduced shear stress and sediment deposition downstream of the structure (Barbhuiya and Dey, 2004; Bennett et al., 2015; Manners et al., 2007; Shields et al., 2001).

1.5. Interaction of flow and sediment

The processes of sediment transport and fluid dynamics are highly interdependent; inherent properties of both sediment and flow create an interactive relationship between hydrology, hydraulics, and dynamic geomorphology. Initially, sediment transport relationships were experimentally defined by relating flow properties (viscosity, density, depth) and channel properties (bed sediment size, channel slope) to deterministically forecast sediment transport. The key parameters, called the boundary Reynolds number and the Shields criterion, compared the ratio of bed shear stress to submerged particle weight per unit area against the ratio of bed sediment diameter to viscous sublayer thickness (Rouse, 1939; Shields, 1936). Over time, data was added and summarized for larger, non-uniform particle distributions in different

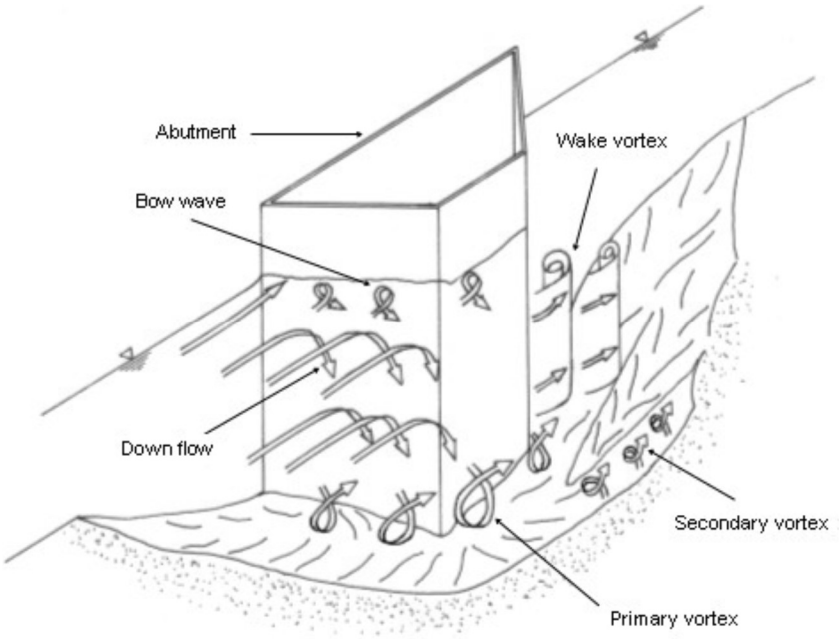

Figure 1.3. Illustration of developed vortical microstructures near a bridge abutment (after Kwan, 1988)

hydraulic regimes (Buffington, 1999; Mantz, 1977; Yalin and Karahan, 1979) and inquiries were made on Shields's experimental procedures (Buffington, 1999; Kennedy, 1995) that called for a more wholistic understanding of sediment transport initiation (Buffington and Montgomery, 1997). In order to build upon the methods and findings of these established deterministic methods of estimating the critical condition, other tools that properly account for the temporal hydraulic factors of intermittent transport (fluctuating velocity and bed shear stress) in which time-averaged velocity and shear stress values underperform (Elhakeem et. al., 2017; Papanicolaou et al., 2001; Papanicolaou et al., 2004). This consideration of scour and bed shear stress co-evolution requires information on the channel bed roughness and critical soil resistance values of the underlying substrate to accurately characterize the bed shear decay function near the ELJ (Li and Guo, 2016; Suaznabar et al., 2014). Furthermore, these exchanges between flow and sediment are increasingly pronounced in the vicinity of a hydraulic structure with regards to varied water surface profiles, three-dimensional (3D) vortical structures, and bed shear stress amplification by a factor of 3-5 near the structure nose (Ahmed and Rajaratnam, 2000; Kothyari ad Raju, 2001; Whitehouse, 1997). The vortices discussed in Section 1.4 affect scour through the down flow initiating the primary vortex, which drives the scour process vertically and longitudinally as the secondary vortex applies lateral resistance to scour hole widening. The wake vortices deposit mobilized sediment in the slower moving section behind the ELJ.

Scour caused by these localized changes in flow structure due to the presence of the structure are termed local scour, while scour caused by geometric changes that decrease the cross-sectional flow area in the channel are termed contraction scour (Melville and Coleman, 2000). It is difficult to differentiate between these two processes as there is no defined method to attribute a percentage of scour depth to either cause individually (Melville and Coleman, 2000; Wallerstein et al., 2003). The simplified term "localized scour" may be used to recognize that both scour processes are occurring simultaneously in the channel where a hydraulic structure cause both local scour while also contracting the channel width. In this study, the term clearwater scour is used for localized scour in which negligible scour in the approach and outlet sections was measured where the scour hole extents were well confined in the test section. Achieving these conditions will be discussed in Chapter 5 for model design. This clearwater scour phenomenon, governed by the interdependent evolution of flow and sediment, was annotated using quasi-simultaneous measurements of surface velocity and scour depth from time of sediment transport initiation through equilibrium to illustrate the bed shear stress decay function in a non-stratified gravel bed at a permeable ELJ structure. This decay function may further inform numerical models for predicting sub-maximum scour depths at discrete points.

1.6. Research limitations

The literature search presented above illustrates the complex nature of flow around different hydraulic structures of varying shape and porosity. While there are some studies focused on the quantitative description of the 3-D nature of flow and turbulent structure around abutments (Barbhuiya and Dey, 2003; Koken and Constantinescu, 2014), porous rock barbs (Fox et al., 2005), and around select permeable logjam configurations (Bennett et al, 2015; Bocchiola, 2011; Manners et al., 2007), greater work is needed to fully understand flow structure in the vicinity of the dolotimber-based ELJs to guide design and modelling as implementation increases (Abbe et al., 2011; Cardno Entrix, 2011). Furthermore, the mischaracterization of dolotimber ELJs as impermeable structures in both hydrodynamic models and scour analyses highlights the necessity of accurate representation of bed shear stress as scour evolves in the complex flow fields found at field installations (Cardno Entrix, 2011; NHC, 2010).

Moreover, the coevolution of scour and bed shear stress over time has been studied experimentally and numerically around bridge piers, abutments, and in the condition of submerged bridge decking causing pressurized flow (Koken and Constantinescu, 2014; Guo, 2011; Li and Guo, 2016). These studies base their bed shear stress decay on discrete experimental measurements of scour depth; flow was stopped in order to take the maximum scour depth and started again as a non-continuous experiment. The non-continuous manner of these studies could introduce errors in the temporal scale of movement in gravel beds as the orientation and degree of particle interlocking may change as flow is lowered and raised over non-uniform beds. These measurements are also only taken at the deepest scour location rather than providing more complete bathymetric information relating depth with scour, as has been done in Fox et al. (2005), Kuhnle et al, 2003; Wallerstein et al. (2003). Although the use of conventional acoustic doppler velocimetry (ADV) and laser doppler velocimetry (LDV) techniques may track velocity changes near the structure at discrete points in evolution, the use of a point gauge for scour hole depth does not allow for concurrent flow and bed measurements over the course of scour evolution. As suggested in Papanicolaou et al. (2017), utilizing a multiple-transducer array (MTA) of continuous depth-reading sonar technology and current particle image velocimetry (PIV) methods would allow for improved mapping of the scour hole bathymetry continuously throughout the test for direct relation of semi-synchronous flow and scour measurements. To the current knowledge of the writer, the only experiments utilizing this continuous scour mapping are tracking bedforms in a mobile sand bed over time using an MTA (Friedrich, 2005; 2006; Guan et al., 2014). Accounting for the interaction between flow and sediment movement in the eroding mobile bed in direct comparison to velocity may improve applicability and accuracy of scour depth estimates due to bed shear stress decay in gravel bed rivers.

2. Study overview

2.1. Scope

The primary goal of this research is to evaluate the complex hydrodynamic conditions associated with the spatiotemporal evolution of scour around a dolotimber ELJ, specifically in a gravel-bed river, using instrumentation for measurements scour depth and localized velocity changes as scour develops. In order to illustrate this coevolution, this study provides unique hydrodynamic information for tests performed at clearwater scour conditions where a series of three porous dolotimber ELJs are anchored into a gravel bankline during mobile-bed experiments. Techniques to continuously measure scour depth during scour evolution were analyzed and related to the volumetric scouring rate in order to temporally predict scour volume. These measurements were paired with periodic, non-invasive velocity measurements to explain the evolution of complex vortical structures as bed bathymetry changes over time. Dimensional analysis is employed to provide a general expression for scour depth as a function of the governing parameters (e.g., flow, median particle size and gradation, and flow depth) at equilibrium clearwater scour condition.

2.2. Objectives

Overall, the specific objectives of this study are: (1) establish generic model for scaling for experimental setup; (2) perform measurements of scour, as well as analysis, and verification of scour depth readings during scour evolution; (3) perform flow measurements, as well as analysis, and verification of semi-continuous surface velocity during scour evolution; (4) formulate a decay function utilizing the measurements of continually changing scour depth and surface velocity to relate co-evolving local bed shear stress to scour hole elevation; and (5) utilize this data and parametric analysis from generic model scaling to develop a generic scour equation that predicts the evolution of the scour hole volume and depth in clearwater conditions for gravel-bed rivers. The results of this study are then discussed with respect to new information and insights provided through the experiments.

3. Flume set-up

3.1. Flume infrastructure and construction

The tests were performed in the Hydraulics and Sedimentation Laboratory (HSL) at the University of Tennessee – Knoxville. The tilt-able, water-recirculating flume, designed by Engineering Laboratory Design, Inc., is 10.0 m long, 0.60 m wide, and 0.50 m deep. The flume slope can be adjusted electronically in 0.1% increments up to 5%, allowing for model design to replicate high gradient streams. Water conveyance from the approximately 4.5 m^3 storage reservoir through the 0.203 m diameter main transmission line to the flume headbox was facilitated by a 60 Hz/208VAC/15 HP Leeson centrifugal pump capable of discharging 100 liters per second/1600 gpm (Figure 3.1). The discharge through the main transmission pipe was measured via a digital magnetic flow meter for monitoring the flow volumetric discharge with accuracy of 0.01 gpm. Pipe velocity was displayed digitally, where calculations of bulk discharge entering the channel were completed during each experimental trial. Figure 3.2 shows the digital display of transmission pipe velocity, flume slope, pump frequency, and the toggles for both flume slope and tailgate height. The upstream end of the flume was fed by a headbox that connects the main transmission pipe from the pump and reservoir to the flume channel. The connection between the headbox and the flume channel includes a series of offset rectangular grates dimensioned approximately 0.75 cm prior to a bed section of large cobble (d_{50} = 25 mm) over the initial 0.5 m length leading to the mobile bed sediment utilized in experiments that lines the length of the flume (Figure 3.3). The combination of the two methods resulted in decreased energy and turbulence induced by the inflow pipe and headbox. Furthermore, the grating influenced rectilinear flow at the model inlet, reducing the role of surface waves and encouraging the expedited formation of uniform flow conditions.

At the flume exit, 5 mm diameter steel rods were installed at 10 mm vertical spacing perpendicular to the flow in order to create a tailgate weir (Figure 3.4). The use of these spaced rods in addition to the solid motorized tailgate weir at the flume exit allowed for greater control on exit resistance, ultimately limiting backwater effects to create a fully developed uniform flow test section for the scour experiments. Flow quality will be discussed in greater detail in the following section. At the outlet section of the flume channel, a plexiglass step raised approximately 0.15 m from the flume floor sets the end limit for the sediment bed and sets the outflow point into a sediment basin with an adjustable tailgate weir (Figure 3.5). The sediment basin was not used during these experiments, though the bed was placed 0.15 m deep in the flume channel behind the plexiglass step. The base flume walls and floor are made of transparent plexiglass, allowing optical access to assess flow quality and observe scour experiments from a side- and aerial-view over the entire flume length. Along the top of the flume was a mounted trolley

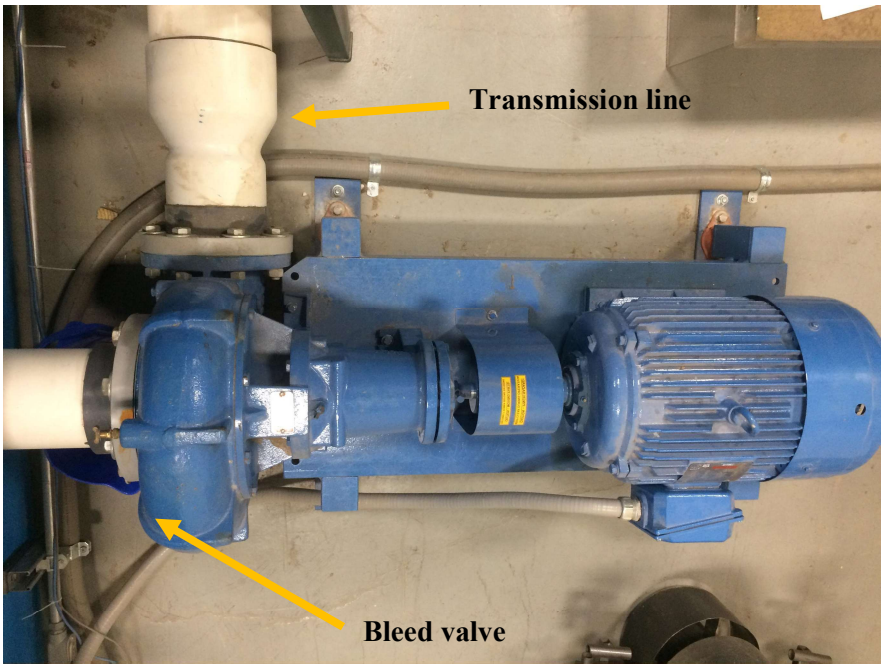

Figure 3.1. Plan view of flume centrifugal pump.

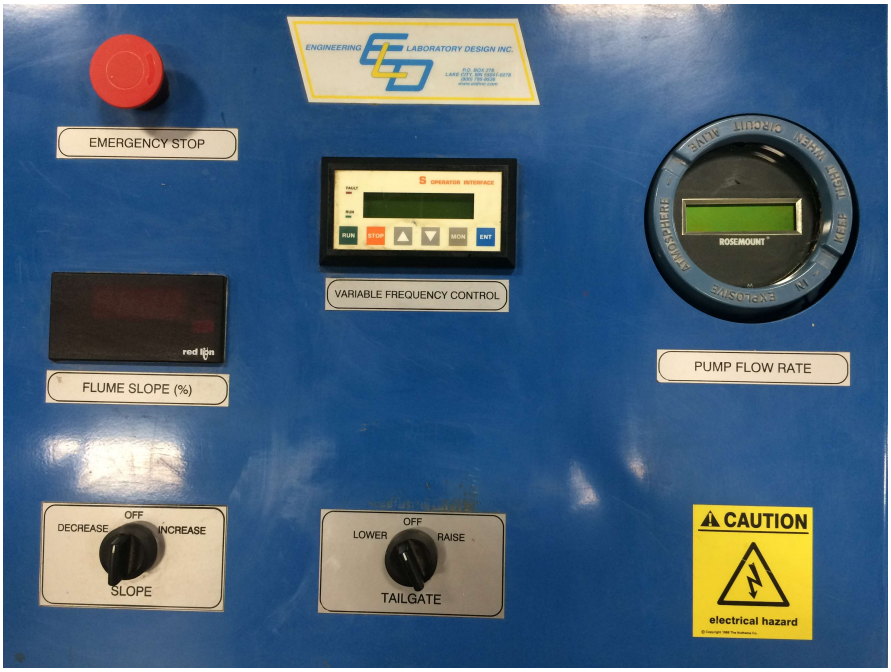

Figure 3.2. Flume control panel featuring digital displays and adjustment toggles.

Figure 3.3. Flume inlet with rectangular grates and cobble bed entrance to promote uniform flow.

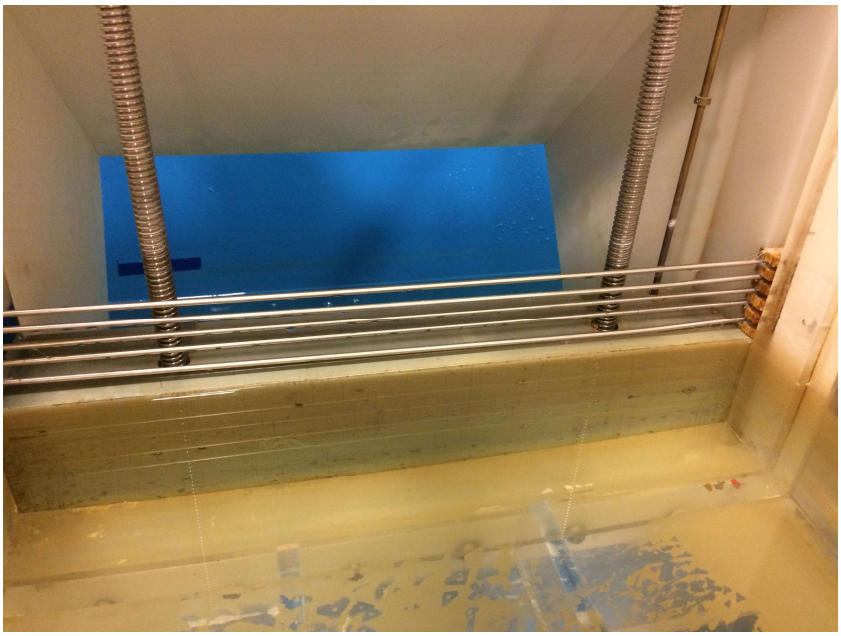

Figure 3.4. Series of steel rods mounted on top of motorized tailgate for finer control of resistance.

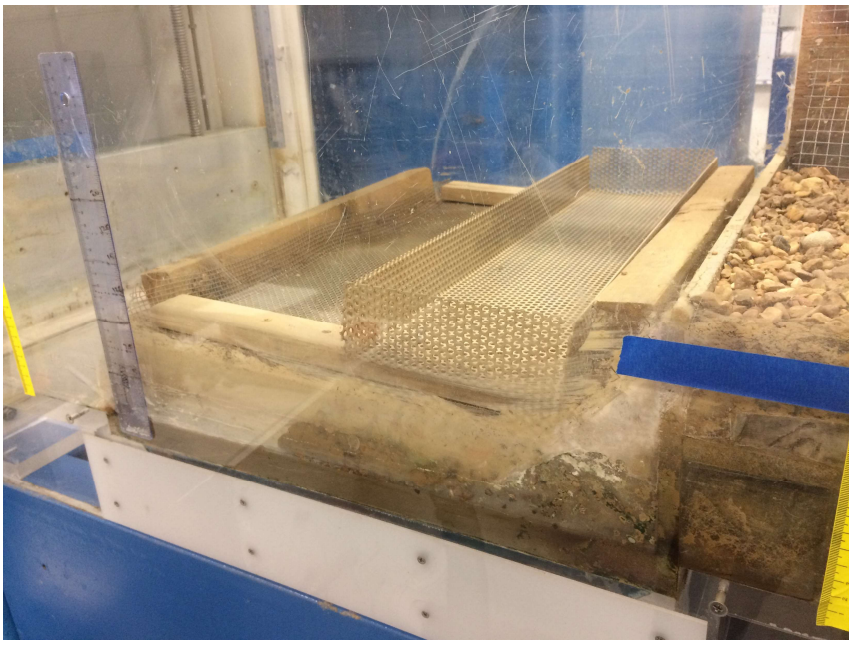

Figure 3.5. Outlet step and sediment basket at end of test section.

that housed the different instruments (ADV, point gage, infrared camera, etc.) utilized throughout the study, allowing for free longitudinal movement along the entire 9 m length. Graded tape on the trolley transverse and along the flume length allowed for a consistent metric measuring grid during each experimental trial (Figure 3.6). To protect the plexiglass sidewalls from scratches and damage, a plastic liner was applied up to the bed depth (15 cm) all along the flume bed. This preserves the optical quality for future use of laser instrumentation and high-accuracy velocimetry methods in this particular flume setup. For further protection, a wooden frame constructed of plywood that is 0.25m x 3.0m and 2.0cm thick, was built along the flume wall opposite of the operator control station in order to create a sturdy base for the gravel revetment structure. This frame also provided a platform on which to secure the ELJ structures. The nose-end sections of these wooden platforms were later removed as ELJs were built into the gravel bed discussed later in Chapter 5 (Figure 3.7, Figure 3.8). Prior to installation, and again after installation, two coats of commercially available waterproofing wood sealant were applied to the plywood base to prevent warping that may otherwise cause geometric channel inconsistencies over time.

Covering the gravel revetment construction is mesh wire with nominal openings of 1.25cm to maintain porosity, secure the gravel structure, and limit the alteration of surface roughness (Figure 3.9). Gravel selection for the revetment structure will be discussed further in Section 5.2 as related to the dolotimber porosity.

3.2. Flow quality

Graded tape rulers were placed vertically at ten locations on the flume wall (approximately 1.0 m spacing) to take detailed water surface profiles at the beginning and end of experiments. Backwater effects caused by the structure resulted in a local depth increase thus, flow uniformity was defined by comparing the flow depths in the inlet section and outlet sections of the flume. The measurement locations were not affected by the structure, allowing for the effects of tailgate height and pump discharge to be balanced for uniform flow. These measurements were facilitated by a thin line of tape run longitudinally along the flume wall measured at 0.15 m from the flume floor to ensure consistency in bed height before each trial (shown in Figure 3.10).

Multiple flow quality checks were made based on established literature to ensure that the flow conditions tested herein are representative of natural river flows. These checks were based upon the final flume dimension design, where some measurements and values will be discussed further in Chapter 5. The test section location, where the ELJ structures were placed, is 7.25 m downstream of the headbox to ensure that flow is fully-developed during all flume trials. To ensure fully developed flow conditions for the case of a rough boundary, the following relation must be satisfied: $\frac{L}{4R_h} = 32$ (Nezu and Nakagawa, 1986),

Figure 3.6. Overhead trolley mounted to flume rails for mounting instrumentation.

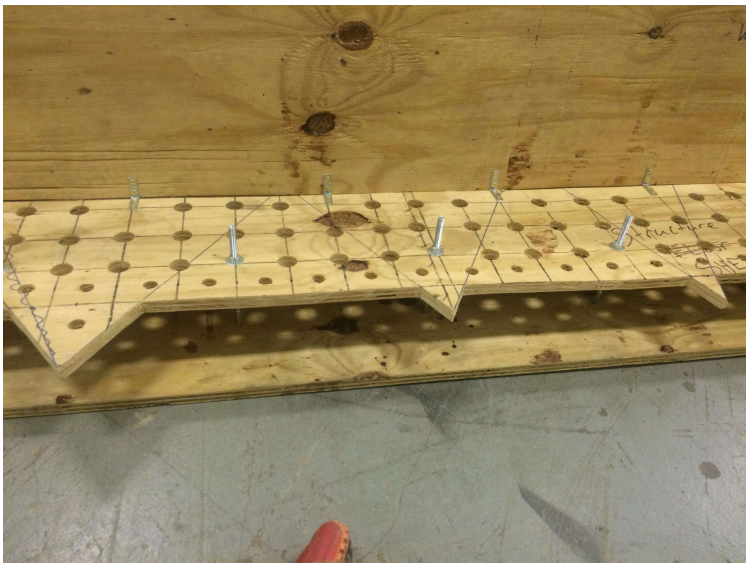

Figure 3.7. Platform constructed in ELJ test section.

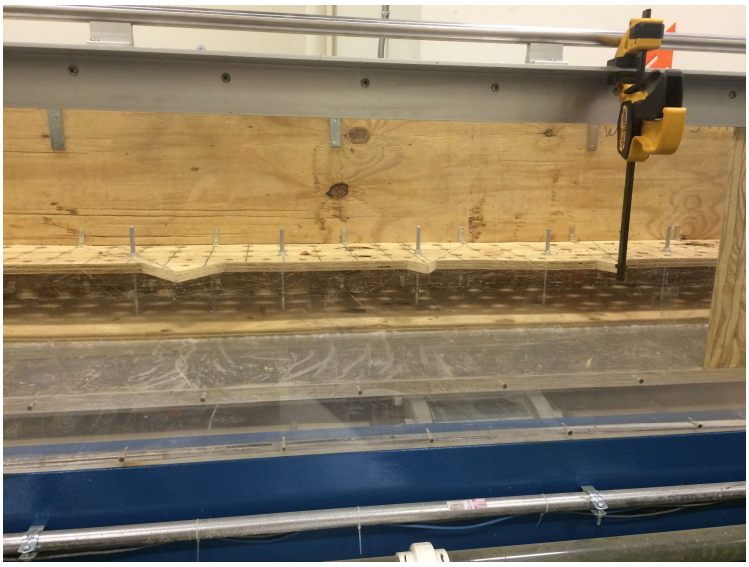

Figure 3.8. Platform constructed in ELJ test section, installed.

Figure 3.9. Gravel revetment with wire mesh support.

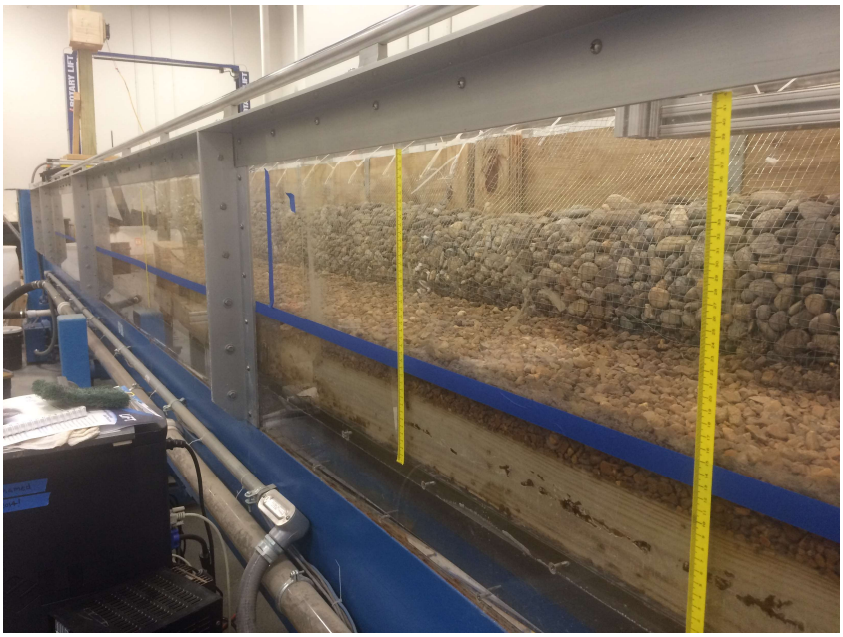

Figure 3.10. Clear plexiglass flume walls allow for side- and aerial-view optical access.

where, L denotes the channel length that fully developed conditions are reached and R_h is the hydraulic radius of the flume cross section. Figure 3.11 shows a dimensioned plan view of the flume and installed ELJ structures used during the experiments. To ensure that the incoming flow is two-dimensional during testing, the ratio of the top width to the average flow depth, B/h, is greater than 5 such that B = 47 cm, h = 8.1 cm, and B/h = 5.8 (Song et al. 1994). The ratio of the average flow depth to the bed roughness, h/d_{50} (8.1 cm/0.081 cm), is greater than 3, so that no surface effects are pronounced during the tests (Bettess 1984). The wall effects are determined to be minimal at a distance of 10 cm from the flume walls (Vanoni and Brooks, 1957).

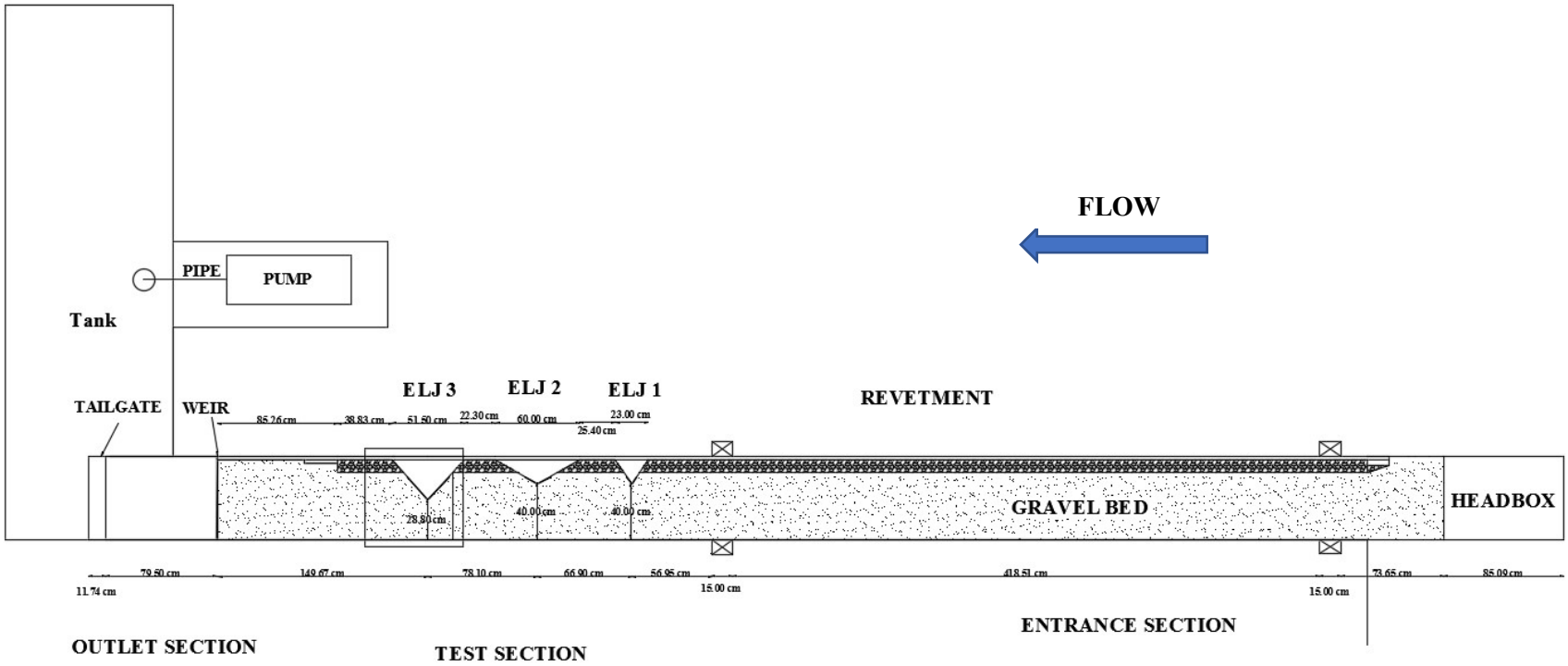

Figure 3.11. Dimensioned plan view of flume model setup.

4. Case study of the prototype ELJ

4.

4.1. Prototype Hydrologic and Bathymetric Information

A hydraulic analysis memorandum was completed by Northwest Hydraulic Consultants. Inc. (NHC) and provided by WSDOT, including bathymetric survey data of the project site at Milepost 100.7 along State Route 20 (SR 20) between Rockport, WA and Concrete, WA` illustrating the most recent bed elevation and water surface elevation available, as well as hydrologic evaluation for reasonable modeling inputs (NHC, 2010). Stage and discharge data were taken from nearby gauges (#12194000, #12193500, #12189500) hosted by the United States Geological Survey (USGS). In conjunction with hydrologic analyses for flood damage reduction and other feasibility studies sponsored by the United States Army Corp of Engineers (USACE), the Federal Emergency Management Agency (FEMA), and Skagit County authorities, discharge data and flow frequencies were calculated for the reach bordering State Route 20 near Milepost 100.7 in the ELJ prototype section (Table 4.1).The stream data was published in the state of Washington Water Resources Records by the USGS and in the cited memorandum (NHC, 2010). The WSDOT sought to evaluate the hydraulic performance of the ELJs at the 2-year and 10-year events, corresponding with bankful and over-bankflow. The discharges of the 2- and 10-year events, as outlined by WSDOT for this project, were 33000 and 55000 cfs, respectively.

Using the provided geographic information system (GIS) bathymetric data, 160 cross sections were taken in ArcGIS along the project reach to ensure high-resolution hydrologic and hydraulic calculations in order to most accurately quantify boundary roughness and flow continuity through the ELJ3 section (Figure 4.1). From this data, it was found that the channel bed slope was approximate 0.0015 ft/ft, the protrusion length of ELJ3 into the main channel was nearly 68 ft, and the channel width considered for flow calculations near ELJ3 was approximately 500 ft.

Included in the hydraulics analysis was a stage discharge relationship established upstream of ELJ5 located mid-channel downstream of ELJ3. This relationship was empirically derived by relating features of known elevation to measured discharge values using images and gauge information (Cardno Entrix, 2011). However, due to the changes in channel bathymetry sections, this relationship was not explicitly useful in the experimental design and a more direct stage-discharge relationship at the ELJ3 location needed to be established in order to equate discharge and flow depth in the prototype.

Using provided cross-sectional GIS data and hydrologic information included in the hydraulic analysis as inputs, a stage-discharge curve (Figure 4.2) was developed at the ELJ3 location using the HydroCalc

Table 4.1. Hydrologic evaluation of Skagit River flood frequency.

Recurrence Interval (Years)	Annual Exceedance Probability (%)	Peak Flows (cfs)	
		WSDOT (2007)	USACE (2010)
2	50	32230	36000
5	20	45990	46200
10	10	55710	55000
25	4	68680	68100
50	2	78810	79300
100	1	89360	92500

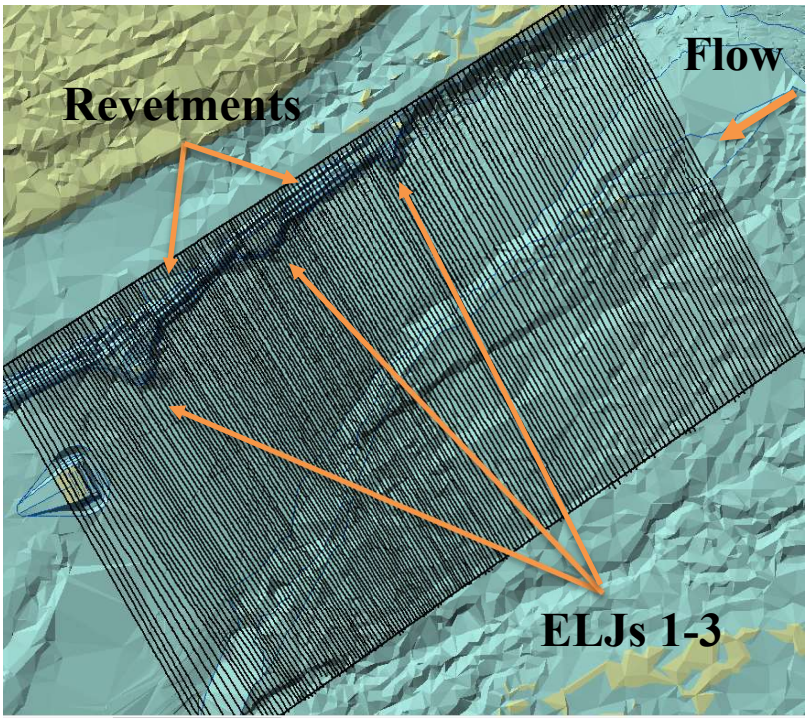

Figure 4.1. Cross-sections taken from bathymetric GIS data for hydraulic calculations.

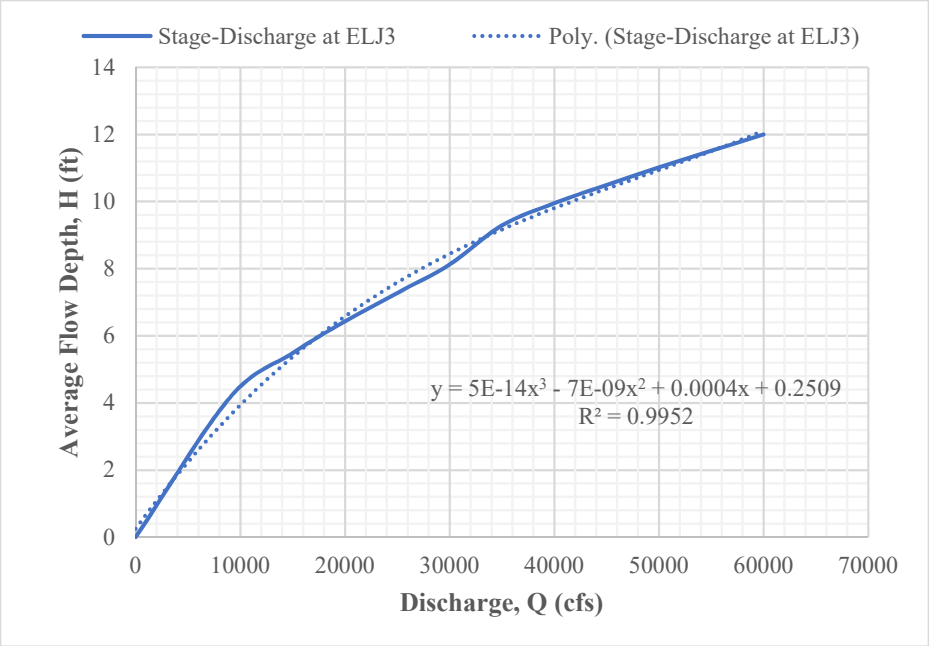

Figure 4.2. Prototype stage-discharge relationship at ELJ3.

software, version 2.0 (Figure 4.3). Developed by NHC., the program calculates normal depth and velocity, Froude number, critical depth, and critical velocity by inputting channel characteristics (shape/cross-section), discharge, Manning's roughness, and the channel slope. The normal depth is calculated from the Manning's equation in English units using discharge, channel geometry, and roughness; the critical depth is associated with a Froude number value of 1 where critical flow is reached. The Manning's roughness coefficient, *n*, is characterized with relation to the median bed particle diameter, d_{50}, by Anderson (1970):

$$n = 0.0395\, d_{50}^{1/6}$$

The Anderson equation was selected as it was developed using similar bed sediment (0.0005 – 1.0 ft diameter) in flume and field data at slopes less than 1% (Rice et al., 1998). Provided with the channel characteristics by WSDOT, the median particle size was determined to be 47 mm in the ELJ test section. This yielded a Manning's *n* value of 0.029 for the prototype channel. This value agrees with the range of 0.023-0.036 for channels containing a gravel bottom and riprap-lined side walls (Chow, 1958). Manning's equation is given by

$$Q = (1.49/n)\, A\, R_h^{2/3}\, S_0^{1/2}$$

$$R_h = A/P_w$$

$$V = Q/A$$

where Q is the fluid discharge, A is the channel cross-sectional area, R_h is the hydraulic radius, P_w is the wetted perimeter, V is the bulk velocity, and S_0 is the energy slope. Manning's Equation was pertinent because it is valid for lowland rivers experiencing steady and uniform flow (Chang 1998). The Froude number, which is the ratio of inertial to gravitational forces in open channel flow, is defined by Sturm (2010) as:

$$Fr = V / \sqrt{(gH)}$$

Where Fr is the Froude number, g is the gravitational constant, and H and the average flow depth. In conjunction with the provided field data and the use of HydroCalc, a table of flow conditions including parameters relevant to scour development for the two events at the prototype location was tabulated using the following equations:

$$\tau_b = \gamma R_h S_0$$

$$u_* = \sqrt{(gHS_0)}$$

$$Re_* = u^* d_{50}/v$$

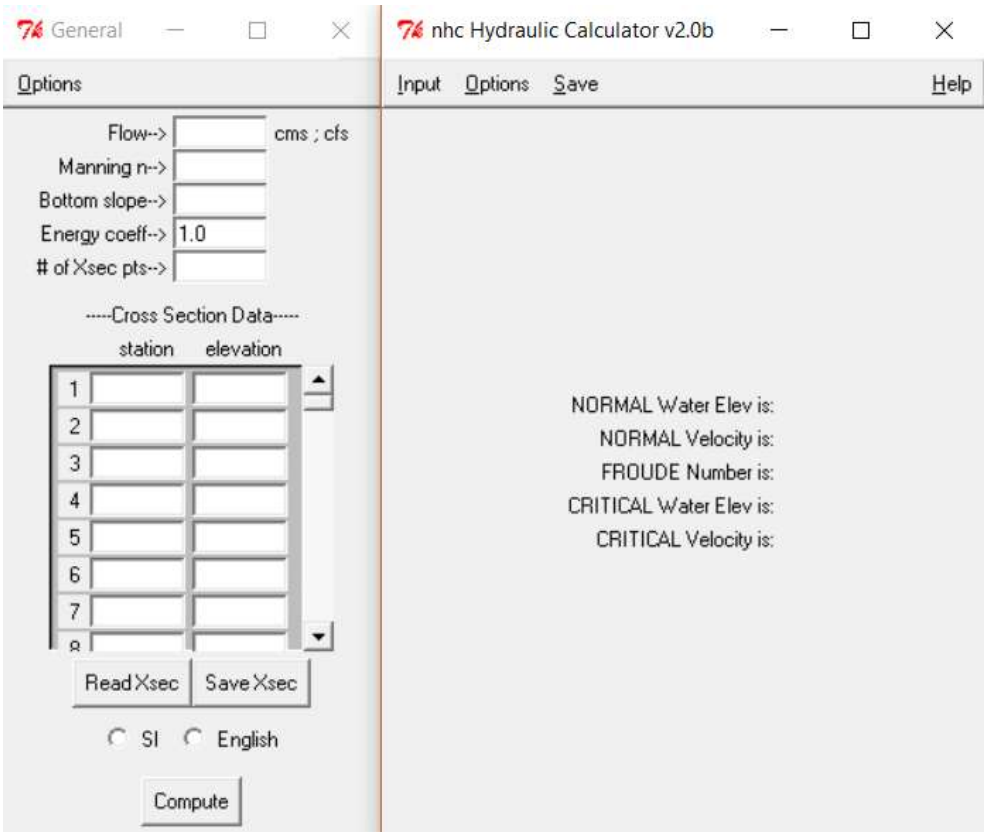

Figure 4.3. HydroCalc software used to establish stage-discharge relationship at ELJ3.

$$Re = VH/v$$

$$\tau_{*=} u_*^2/(1.65*g*d_{50})$$

where $u*$ is the shear velocity, H is the flow depth, Re is the Reynolds number, v is the kinematic viscosity of water, τ_b is the bed shear stress, $\tau*$ is the dimensionless bed shear stress, and γ is the fluid unit weight (Pattison, 2011; Shields, 1936; Sommerfield, 1908; Streeter and Wylie, 1979; Sturm, 2010; Vanoni, 1966; White, 1994). It was determined that at both the 2-and 10-year discharges, flow was subcritical (Fr <1) and turbulent (Re > 4000), as is present in many natural rivers (McQuivey, 1973). Bulk velocity was calculated to be 8 and 9.5 ft/s, shear velocity to be 0.62 and 0.73 ft/s, and bed shear stress to be 0.75 and 1.03 lb/ft^3 for the 2- and 10- year events, respectively. The dimensionless bed shear stress (also known as the Shields criterion) for the 2-year flow was 0.047, while for the 10-year flow was 0.065. As derived in literature, the threshold of motion for non-uniform sediments at τ_c*= 0.03-0.06 was met such that for the lower flow there was only clearwater scour in the vicinity of the ELJ3 structure, and there was likely more general movement in the main channel for the 10-yr event (Brownlie, 1981; Buffington, 1995; Gessler, 1971; Komar, 1987; Neill, 1968; Parker et al., 2003; Shields, 1936; Yalin and Karahan, 1979; Zeller, 1963).

The stage-discharge curve presented includes only data from USGS gauging station #12184700 from the Skagit River at Rockport; thus, the results from the polynomial fit equation may decrease in accuracy when extrapolating outside of these flow conditions.

This stage-discharge data was useful in determining the related flow depth and structure submergence for a given discharge; in conjunction with the construction report, it aided in experimental design for characterizing clearwater and general scour conditions. Table 4.2 summarizes the prototype flow and channel conditions for the 2-year and 10-year events for use in model design in Chapter 5.

4.2. Prototype mobile bed sediment

In order to facilitate initial scour depth estimates, two Wolman (1954) pebble counts were performed at the project site to characterize the grain size distributions both for the surface and subsurface (WSDOT, 2010). Subsurface sizes were recorded at ELJ5 downstream of ELJ3 and were used to determine bed configuration before armoring had happened. The surface estimates near ELJ3 were used for this study as they pertained directly to the location and scour conditions sought to be modeled (Figure 4.4). From this data, key particle sizes of d_{16}, d_{50}, and d_{84} were determined to be 33, 47 and 71 mm, respectively. These represent the 16th, 50th, and 84th percent finer grain diameters. The geometric standard deviation of the distribution, σ_g, is used to express sorting in terms of the geometric mean.

Table 4.2. Prototype flow conditions for 2-year and 10-year events.

Parameter	Symbol	Units	Event	
			2yr	10yr
Discharge	Q	ft^3/s	33000	55000
Water temperature	T	°F	55	55
Kinematic viscosity	v	ft^2/s	1.21E-05	1.21E-05
Fluid unit weight	γ	lb/ft^3	62.41	62.41
Reach length	L	ft	1500	1500
Channel bed slope	S_0	[]	0.0015	0.0015
Median sediment diameter	d_{50}	ft	0.1542	0.1542
Flow depth	H	ft	8	11
Depth-average bulk velocity	V	ft/s	8	9.5
Reynolds number	Re	[]	5.29E+06	8.64E+06
Modeled flow width	W	ft	374	374
Froude number	Fr	[]	0.498	0.505
Wetted perimeter	P_w	ft	533.5	543.6
Cross sectional area	A	ft^2	4201.2	5750.5
Hydraulic radius	R_h	ft	7.9	10.6
Friction velocity	u^*	ft/s	0.622	0.729
Particle Reynolds number	Re_*	[]	7.92E+03	9.29E+03
Bed shear stress	τ_b	lb/ft^2	0.75	1.03
Dimensionless bed shear stress	τ^*	[]	0.047	0.065

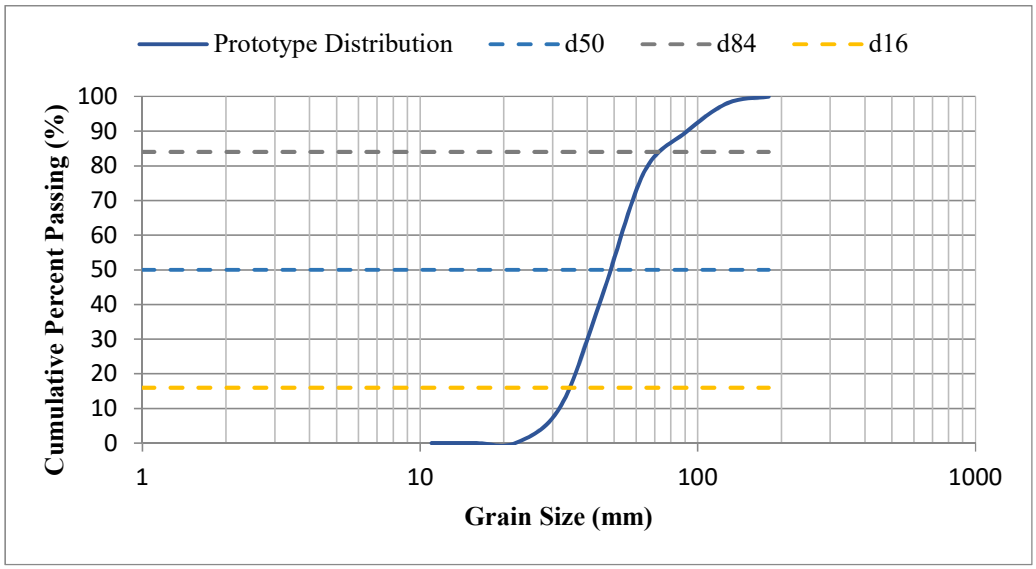

Figure 4.4. Prototype grain size distribution (Cardno Entrix, 2011).

Using the equation provided in Sturm (2010),

$$\sigma_g = \sqrt{(d_{84}/d_{16})}$$

the geometric standard deviation of the prototype surface gravel bed was calculated to be 1.47, representing a fairly uniform (well-sorted) bed composition. The particle specific gravity was reported to be 2.65.

4.3. Prototype ELJ architecture

The prototype installation included four ELJ structures that protruded from the bank to deflect velocity away from the bankline, protecting the roadway surface (Figure 4.5). A fifth ELJ (ELJ5) was situated on a bar/island that further directed flow into the main channel and away from the side channel. Revetments were stationed downstream of protruding ELJs to stabilize the bank and prevent intermediary erosion, further protecting the roadway. The ELJs were designed with launchable toes such that could deform as scour holes developed while maintaining their structural integrity. Both the ELJs and the revetments incorporated LWM, constituting high percentages of the structures. These components were discussed previously in Section 1.1. Although it was not expressly communicated what species of tree was used in the structures, Mosher and Lunnum (2003) indicate that based on local availability and the desired acoustic properties, either Douglas Fir or Sitka Spruce were the most likely species. Using the provided construction documentation from Cardno Entrix (2011), the ELJs and revetment configurations were dissected to perform a volumetric analysis of their component in order to match them in the physical flume model. For this project, 15 different types of dolotimber configurations were created by differing size and number of logs, location, and orientation to promote interlocking, structural stability, wood and sediment recruitment, and habitat creation.. The components and their volumetric contributions (logs, gravel ballasts, dolos) of ELJ3 are summarized below in Tables 4.3-4.5. Each ELJ and revetment were built in layers, stacking the irregularly shaped dolotimber modules on top of one another in an interlocking manner. Table 4.6 details the stacking of components in ELJ3, while Table 4.7 illustrates the component breakdown and porosity calculations. Detailed calculations of the other ELJs and revetments can be found in Appendix A. This decomposition and layering detail was used to design model dolotimber and ELJ structures that could closely mimic the porosity, roughness characteristics, and geometric footprint of the prototype installation (Chapter 5). The prototype was designed by Cardno Entrix in accordance with WSDOT standards (WSDOT, 2010a; 2010b; 2010c; 2003).

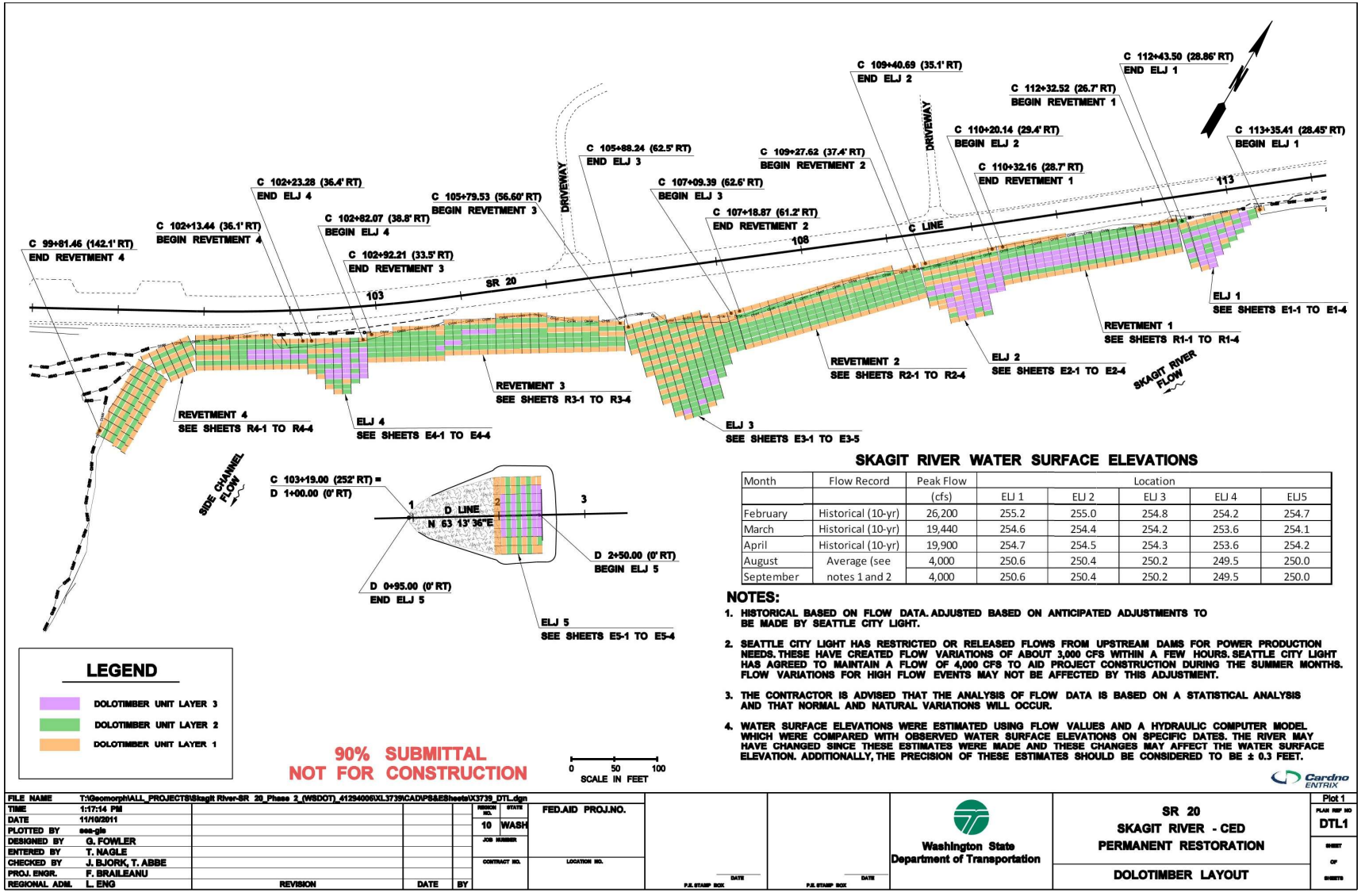

Figure 4.5. Construction plans for prototype ELJs and revetments (Cardno Entrix, 2011).

Table 4.3. Prototype log component volumes respective of dolotimber type.

Type	Prototype Log Description	Volume (ft^3)
a	24" DIA Log, 20' Long	62.83
b	18" DIA Log, 20' Long	35.34
c	18" DIA Log, 10' Long	17.67
d	18" DIA Log, 7' Long	12.37
e	16" DIA Log, 25' Long	34.91
f	16" DIA Log, 20' Long	111.70
g	12" DIA Log, 25' Long	78.54
h	12" DIA Log, 20' Long	62.83
i	6" DIA Log, 20' Long	15.71
j	16" DIA, 20' Long	111.70
l	6 - 4" DIA,18' Long	9.42
	5 - 8" DIA, 18' Long	31.42
	5 - 12" DIA, 18' long	70.69
	Racking Logs	111.53
m	18" DIA Log, 18' Long	31.81
n	4" DIA Log, 20' Long	1.75
o	8" DIA Log, 20' Long	6.98
p	12" DIA Log, 20' Long	15.71

Table 4.4. Prototype ballast component volumes respective of dolotimber type.

Type	Ballas Component Description	Volume (ft^3)
T	8" streambed cobble	31.42
	70-4" DIA logs/bundle, 11' long	67.20
	26-6" DIA logs/bundle, 20' long	102.10
W	8" streambed cobble	62.83
V	8" streambed cobble	25.13
P	8" streambed cobble	94.25
P	LOGS 3-3.8' DIA ballasted racking bundles (log # for three bundles)	201.59
V	LOGS 1-3.8' DIA ballasted racking bundle	42.76
W	LOGS 2-3.8' DIA Ballasted racking bundle (log # for two bundles)	134.39

Table 4.5. Prototype dolo component volumes from dimensioned construction drawings.

Component	Volume (ft^3)
Trunk	21.21
Fluke	75.68
Total	96.89

Table 4.6. Prototype ELJ3 layering detail.

ELJ 3				
Layer 1				
Dolo Type	**Count**	**Dolo (Y/N)**	**Log**	
			Type	**Count**
A	5	Y	a	1
			b	1
B	91	Y	c	3
I	0	Y	c	2
			g	1
Layer 2				
Dolo Type	**Count**	**Dolo (Y/N)**	**Log**	
			Type	**Count**
B	24	Y	c	3
N	2	Y	c	2
T	0	Ballasted Bundle		
E	18	Y	h	1
			d	2
S	10	Y	e	1
J	4	Y	f	1
Q	7	Y	e	1
L	7	N	Racking Logs	
O	21	Y	d	2
W	7	Ballasted Bundle		
Layer 3				
Dolo Type	**Count**	**Dolo (Y/N)**	**Log**	
			Type	**Count**
H	0	Y	g	1
I	0	Y	c	2
			g	1
L	1	N	Racking Logs	
S	3	Y	e	1
J	2	Y	f	1

Table 4.7. Prototype ELJ3 component breakdown and porosity.

ELJ 3 Prototype			
Component	**Volume (ft^3)**	**Percent Structure Volume (%)**	
Cobble	440	1.4	
Logs	12024	39.3	
Dolos	18118	59.2	
Total Solids	30582	**Porosity**	72.0
Total Volume	109312		

5. Physical model design

5.1. Mobile bed sediment

The flume floor was covered with rounded aggregate freely laid to maintain a uniform bed height and roughness while minimizing compaction. Flume size limitations prevented traditional geometric scaling ratio satisfaction; this would require small sand or clay to be used in the model bed These materials would not behave the same as a cohesionless, interlocking bed sediment like gravel. Dynamic scaling was done with respect to dimensionless bed shear stress, which is reliant on particle density and size. Following literature on the designation of gravel particles compared to sand and cobble, the desired dimensionless bed shear stress ratios were achieved within our experimental limitations using the described model gravel while also allowing illustrating the phenomenon of particle interlocking and in gravel bed rivers. The naturally worn gravel, provided by Harrison Aggregates in Knoxville, TN, had a median sediment diameter (d_{50}) of 8.12 mm. This lies within the accepted range of 2 – 64 mm as the median bed particle size to be designated as a grave-bed stream by the USDA Forest Service (Bunt and Abt, 2001). The 0.15 m thick active layer of washed river gravel was found to be of an adequate depth for achieving maximum scour by enveloping the upper levels of a number of clear-water scour equations and adding a factor of safety (e.g., Ghodsian and Tehrani, 2001; Melville, 1993). Due to the reported over prediction of scour depths in flume studies (e.g. Cardoso and Bettess, 1999; Kuhnle et al., 2002; Richardson and Richardson, 1993) and forecasted flow depths of future experiments at elevated flow conditions, the mobile bed depth was deemed acceptable clearwater scour experiments around a permeable structure. The bed gravel grain size distribution was conducive to achieving dimensionless bed shear stress magnitudes, τ_*, necessary for clearwater scour within the experimental limitations of the flume infrastructure, as well as maintaining similar prototype and model geometric standard deviations, σ_g (Figure 5.1), where the 84th and 16th percentile of particle sizes are represented as d_{84} and d_{16}, respectively.

$$\sigma_g = \sqrt{(d_{84}/d_{16})}$$

$$\Phi = -log_2(\text{diameter in mm})$$

$$\sigma_\varphi = \frac{\varphi_{84} - \varphi_{16}}{2}$$

Both the prototype and model sediments were well-sorted based on the phi-scale sorting index of particle size with geometric standard deviations of 1.46 and 1.47, respectively (Parker and Wilcock, 1993); discussed in the methods Chapter 6, great care was taken to ensure thorough bed mixing prior to each experiment such that representative particle interlocking took place to closely mimic the prototype.

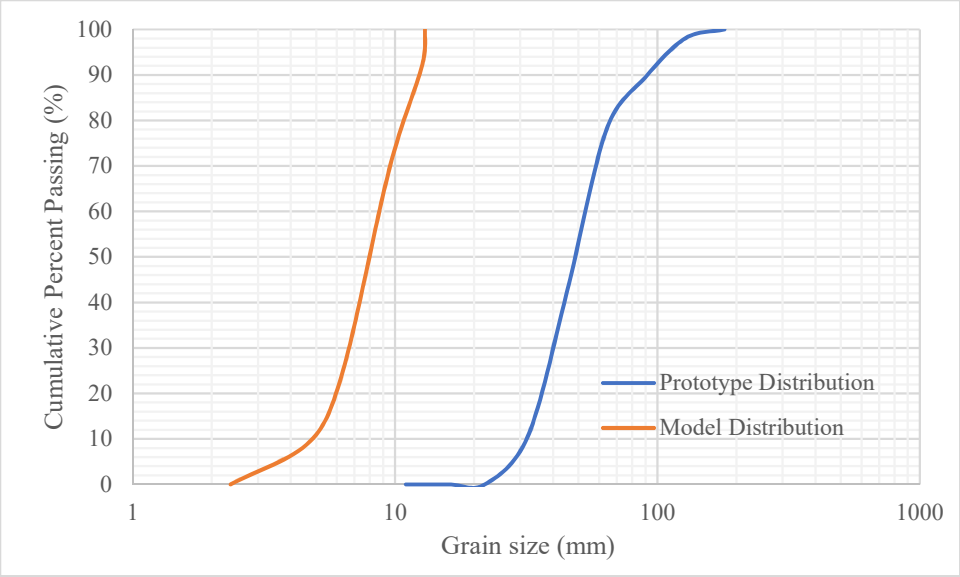

Figure 5.1. Grain size distribution comparison between model and prototype.

5.2. Model ELJ design and construction

The first three ELJs (ELJ1-ELJ3) were selected for the model, as the effects of ELJ4 in the prototype secondary channel would likely have little effect on the scour evolution around ELJ3. The first three revetments were included in the model, whereas the fourth revetment in the side channel was disregarded. Also, ELJ5 was not modeled due to experimental limitations of flume size where wall effects, flow constriction, and simplified bathymetry may significantly affect scour evolution at the model ELJ3. The inclusion of ELJ5 may be revisited in future studies at a larger flume that can address these concerns.

The model dolos were made by fabricating a female silicone mold that was filled with a sieved ready-mix concrete then left to cure overnight. The molds were created by cutting and rolling aluminum sheeting into a 3.8 cm dimensioned cylinder that was then fastened in an orthogonal manner to a notched cylinder to create the 3-D structure seen in Figure 5.2. These proxy structures were coated with motor lubricant and used as male molds for the female casts. The proxy structures were then placed in 5 cm x 5 cm x 5 cm silicone ice-cube trays, over which silicone caulking was applied in order fully submerge the proxy dolo (Figure 5.3). Motor lubricant was again applied to the inside edges of the tray. After curing for approximately 8 hours, the silicone molds were removed from the tray and split at a 45° angle for easier removal. Great care was taken during the removal process, as the sieved concrete mixed prove to be noticeably more brittle in this application. Once removed, the dolos were filed down to match shape and surface roughness of the prototype dolos as described in Chapter 1 (Figures 5.4).

Commercially available wooden dowels were then cut and fastened to the dolos to mimic the prototype LWM and complete the dolotimber structures. Pine dowels were selected in order to replicate the acoustic properties exhibited in the prototype log components, most likely comprising of Douglas fir logs (Littell et al., 2010). The model dolotimber structures were sized iteratively based on the relative dimensions of protrusion length and structure height, porous capacity in structure volume, and the weight of each modular dolotimber; the dolotimbers needed to be heavy enough so that they did not float and strong enough such that they did not artificially crack after repeated use and thereby alter model porosity. Of the 15 dolotimber configurations used in the prototype design (different combinations of log lengths, ballast composition, and number of logs per dolo), only three were focused on for applications in the physical model (Figure 5.5). These three configurations constituted over 90% of the total dolotimbers used, allowing for reasonable assumption that structure roughness and porosity would be still be achievable with this simplification (Cardno Entrix, 2011).

The two key design criteria used for design and assembly of the model ELJ were the structure porosity and the relative proportions of dolotimber components (dolo and logs). In order to calibrate scour

Figure 5.2. Dolotimber male mold design.

Figure 5.3. Dolotimber mold curing and splitting.

Figure 5.4. Filed final model dolos.

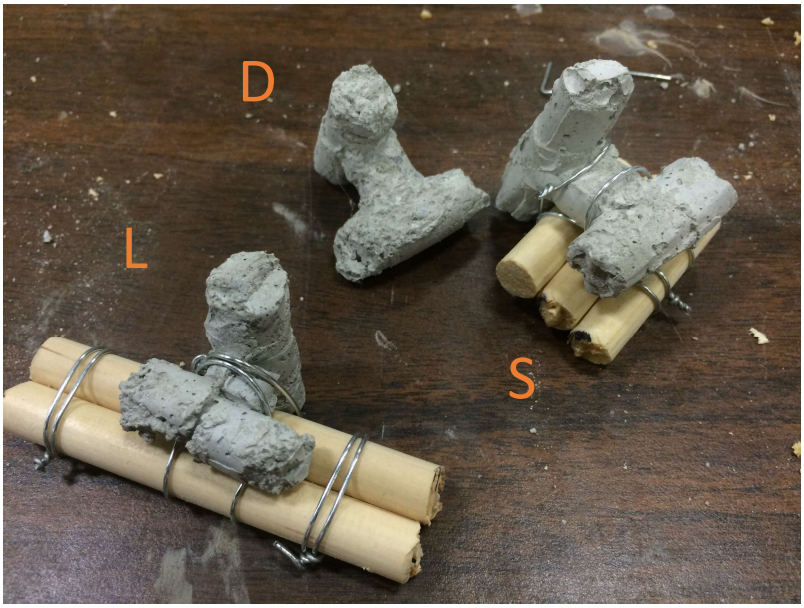

Dolo (no wood)	**D**
Type B Dolotimber (short logs)	**S**
Type A Dolotimber (long logs)	**L**

Figure 5.5. Model dolotimber configurations used in stacked matrix.

prediction for gravel bed rivers around porous structures, growing emphasis has been placed on closely matching structure surface area, volumetric proportions, porosity and their effects on drag force for improved structural stability and optimization of ecological benefit (Manners et al., 2007). A detailed volumetric analysis was completed to ensure that the model ELJs closely matched prototype proportions; they predominantly comprised of dolos (~60%), with the rest being made up of logs (~40%) and a small percentage of cobble ballasts (~1%). Tables 5.1 and 5.2 details these calculations, while Figure 5.6 illustrates the stacked dolotimber matrix used to achieve similar structure relative submergence at the tested discharges, while also maintaining comparable structure porosity. Figure 5.7 shows a closer view of the built ELJ3 structure, and Figure 5.8 shows the overall model test section.

In order to prevent artificial acceleration along the smooth flume plexiglass sidewalls, a bankline revetment was installed to more adequately mimic prototype roughness characteristics. Due to the extensive time and labor needed to adequately produce individual dolotimbers, as well as the significant number and fragility of dolotimbers needed for the length of the model revetment, alternatives were explored when considering the revetment construction methodology. As stated in the ELJ discussion, the primary parameter to match was the permeable nature of the revetment. In this regard, the use of coarse gravel was evaluated as a proxy for the dolotimber revetment. Utilizing studies on the Kozeny-Carman equation for permeability, we equated the porosity of the revetment structures calculated in Section 4.3 to a comparable permeability value of coarse gravel such that,

$$k = [\eta^3/(1-\eta)^2]*[d_{eff}^2/(C_{SH}^2 C_{PK})]$$

$$C_{PK} = 5\tau^n$$

$$K = k\mu/\rho g$$

where k is the permeability (m/s), η is the porosity, d_{eff} is the effective diameter (m), τ is the tortuosity, n is the tortuosity coefficient, C_{SH} is the shape coefficient, C_{PK} is the packing coefficient, K is the hydraulic conductivity (m/s), μ is the dynamic viscosity of water (kg/(m s)), and ρ is the density of water (kg/m^3) With the assumption of a packing factor equal to 9.5 and a tortuosity coefficient equal to 3, from the literature, a packing factor of 78 and an effective diameter of nearly 0.025 m were calculated to be used in the proxy gravel revetment (Judge, 2013; Svensson, 2014). More detailed calculations can be found in Appendix A. As noted prior in Section 3.1, chicken wire was used to form the gravel revetments and contributed to the surface roughness in order to further mimic the roughness elements in the prototype.

Table 5.1. Dimensions of model dolotimber ELJ components for volumetric calculations

Model Component Dimensions		
ELJ 3 Width	0.6329	ft
	7.5943	in
Dolo Width	1.2000	in
Trunk Length	0.4000	in
Trunk Diameter	0.4000	in
Trunk Volume	0.0503	in^3
Fluke Inner Diameter	0.1000	in
Fluke Outer Diameter	0.2000	in
Fluke Length	0.5150	in
Volume of Fluke	0.1510	in^3
Volume - Mid Fluke	0.0855	in^3
Dolo Volume	0.2867	in^3
Length of Logs	3.0000	in
Radius of Logs	0.1969	in
Volume of Logs	0.3652	in^3

Table 5.2. Calculations of structure component percentage between prototype and model for ELJ3.

ELJ 3 Prototype			
Component	**Volume (ft^3)**	**Percent Structure Volume (%)**	
Cobble	440	1.4	
Logs	12024	39.3	
Dolos	18118	59.2	
Total Solids	30582	**Porosity**	72.0
Total Volume	109312		
ELJ 3 Model			
Component	**Volume (in^3)**	**Percent Structure Volume (%)**	
Logs	16.4	40.3	
Dolos	24.4	59.7	
Total Solids	40.8	**Porosity**	72.0
Total Volume	145.7		

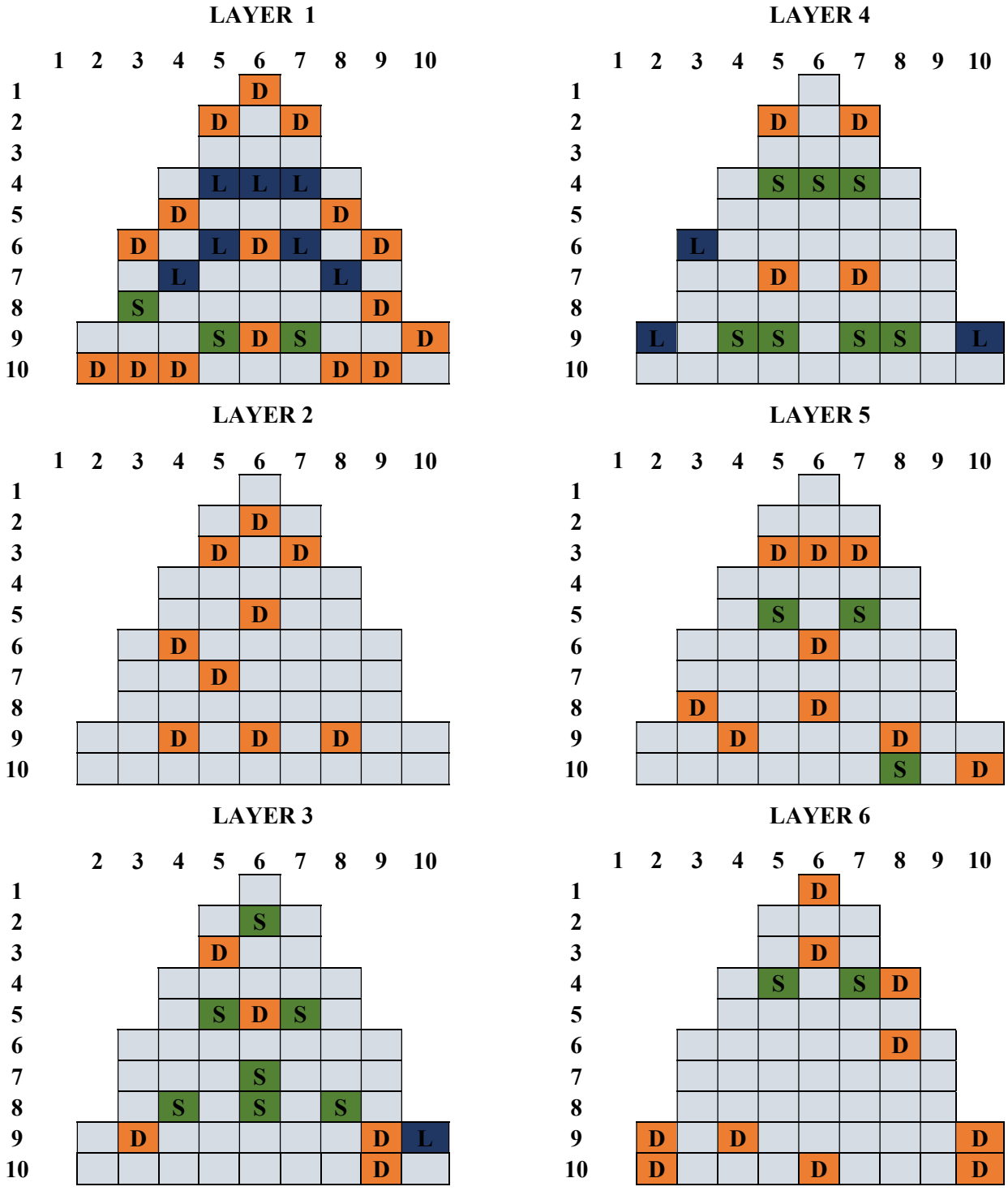

Figure 5.6. Model dolotimber matrix layout for ELJ3.

Figure 5.7. Oblique view of constructed ELJ3 model

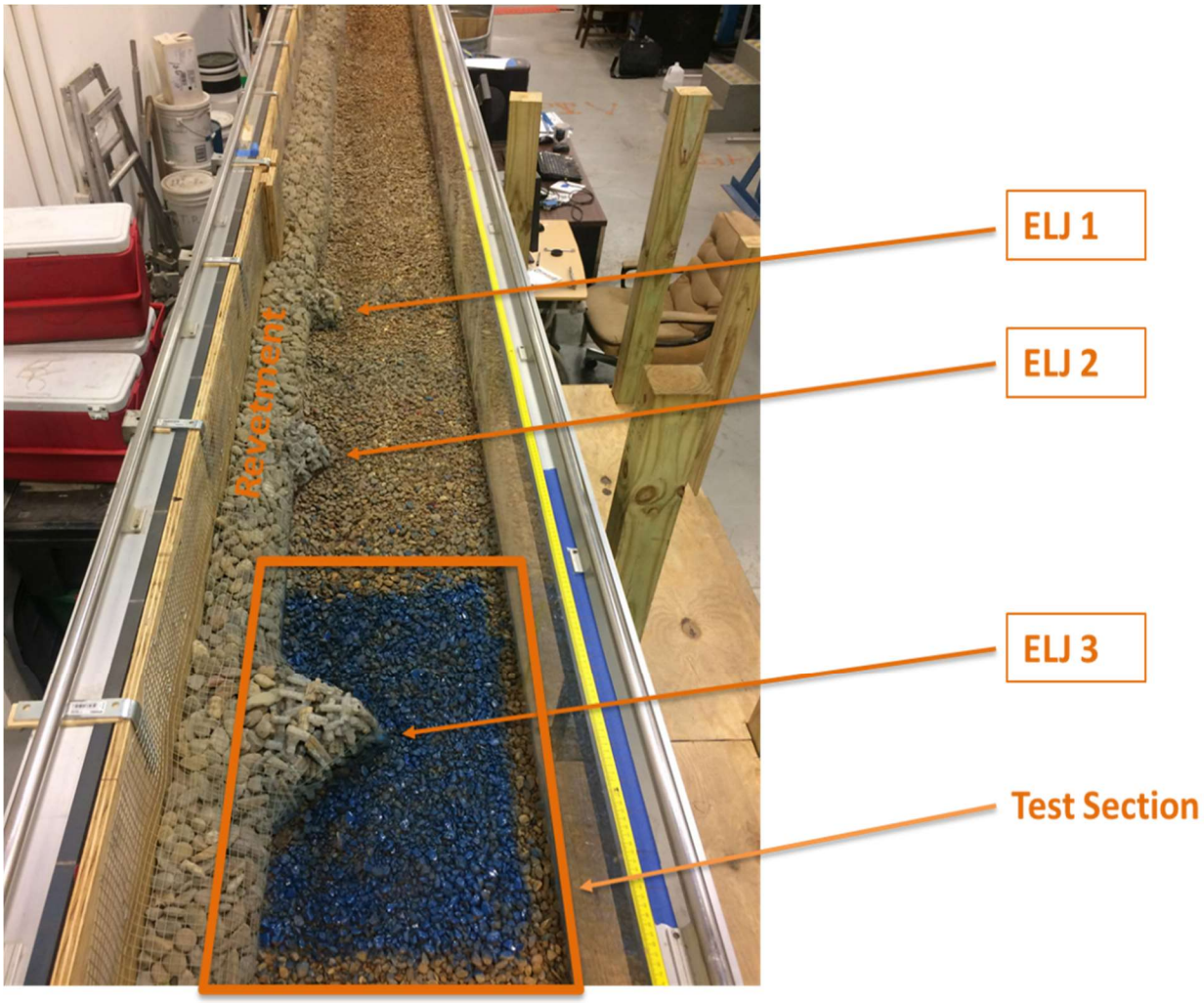

Figure 5.8. Plan-view of constructed model test section.

6. Experimental methodology

6.1. Critical condition

The presented experiments were conducted above the critical bed shear stress for clear water scour, which was estimated by carefully observing particle movement at the toe of the ELJ3 while incrementally increasing the flow conditions until scour occurred. Each flow stage was held constant and movement observed for 5-10 minutes before proceeding to the next condition if scour did not occur. The critical condition was defined as that which caused an initial group of particles to be mobilized near the toe of the ELJ, which thus led to the initiation of a scour hole growing over time. At this determined critical condition, the approach flow depth upstream of the ELJ section (H_{cr}) was used to determine the approach stress. To compare with previous literature investigations, the dimensionless critical shear stress (τ^*_{cr}) was computed by the equation:

$$\tau^*_{cr} = [H_{cr}S_0]/[(S.G. - 1)d_{50}]$$

where S_0 is the bed slope, $S.G.$ is the material specific gravity, and d_{50} is the median particle size of the material. Our testing produced an estimate that clear water scour was initiated near ELJ3 at about τ^*_{cr} = 0.034. This compares very closely with the results from Papanicolaou et al. (2004), who estimated the initiation of clear water scour to occur near a barb structure at an approach flow shear stress of about τ^*_{cr} = 0.033.

6.2. Clearwater experimental procedure

More than 50 repetition experiments above τ^*_{cr}, yet below the general scour threshold, were conducted to establish a consistent experimental methodology and to assess repeatability of the results. Sensitivity of location and rate of scour initiation in conjunction with equilibrium scour characteristics (maximum depth, location of maximum depth, scour hole shape, and scour volume) were factored into clearwater scour methodology development. The wealth of experimental information, in addition to methodological review from literature on mobile gravel bed scour experiments, yielded the experimental procedure listed here:

1. Tank reservoir depth measured to ensure constant head above pump for all experimental trials.
2. Bed material mixed thoroughly to ensure no artificial coarsened areas throughout flume, minimizing bias in scour initiation.

3. Areas of extensively roughened bed removed from flume and replaced with fresh bed gravel.
4. Bed re-leveled while mixing to establish initial bed height while also maintaining consistent roughness; bed height denoted.
5. Flume taken to desired bed slope mechanically; slope verified digitally.
6. Prior to initiating the flow condition, any excess air trapped in the pump was bled via the bleed-out valve with pump running at low frequency to ensure steady discharge during scour trials.
7. Rested perforated metal plate on top of motorized tailgate to provide increased resistance for experimental control.
8. Pump engaged, with slow increases in discharge to prevent energetic bursts that might prematurely initiate scour and to ensure slow filling of all voids in bed material to expel air.
9. Once flow condition reached, perforated plate systematically removed to allow water surface profile to equalize while also limiting experimental difficulties in observing scour initiation.
10. At point of scour initiation, water surface profile taken along entire flume length.
11. Experiments run until pseudo-equilibrium scour rate is achieved (nearly constant scour depth), approximately 90 minutes.
12. Pump powered down and all water drained from flume back to reservoir tank.
13. Using point gage, detailed bathymetric data taken in scour hole and surrounding test section for calculating scour volume.
14. Location and depth of maximum scour measured via point gage and recorded.
15. Bathymetric data utilized by Matlab code to calculate scour volume and create scour contour maps.

6.3. Frozen bed velocity measurements

As the scour hole develops and gains volume, flow over the depression becomes increasingly three-dimensional as the initial two-dimensional flow around the ELJ in the lateral and streamwise directions now also has a plunging component. As local clearwater scour is understood in terms of the threshold of critical beds shear and capacity for sediment transport, the measurement of local velocity magnitudes over the duration of scour evolution has great value in understanding the likelihood and magnitude of gravel-bed scour (Li and Guo, 2016). Multiple methods of particle-image velocimetry (PIV) have been investigated in prior flume studies utilizing laser instrumentation and discrete particle seeding for tracking flow structure in great detail (Fox and Belcher, 2011; Green, 2011; Nezu and Sanjou, 2011). A method

was needed that could allow visualization of flow around and through the porous structure that would not require stopping the test or that would potentially yield errors associated with seeding particles clogging the porous cavities of the ELJ structure. By using a thermal imaging camera and a seeding method of hot water, the individual diffusive droplets could be tracked due to their temperature differential (Admiraal, 2009; Papanicolaou et al., 2011).

To calibrate the thermal LSIV post-processing tools, velocity measurements were taken via ADV at both the flat bed and equilibrium scoured bed conditions and compared. In this study, a side-viewing SonTek ADV (10 MHz) with sampling rate 0.1-25 Hz and velocity resolution of 0.01 cm/s is used for initial comparisons of flat-bed and scoured-bed water surface velocities (Figure 6.1). An important advantage of the ADV is that it measures the flow in a small sampling volume (approximately 0.25 cm^3) that is 10 cm away from the transmitting transducer (Figure 6.2). As this model is a side-viewing ADV, this also enables use in shallow flows where down-looking ADVs may malfunction. Both of these features allow for the collection of turbulence measurements without interfering with the flow. During sampling, the ADV is mounted to a rigid beam on a motorized track, limiting vibrations.

In order to maintain an objectively flat bed at the clearwater flow condition, the gravel bed had to be immobilized to prevent scour. This was done by securing key groups of particles near the toe an along the shear layer glue administered with a hot glue gun (Figure 6.3). As opposed to methods used in other research, this approach allowed for bed freeing in a relatively short amount of time, while also minimizing effort need to spot-fix in between runs. To understand better the flow structures, numerous sampling points were taken in the approach section, in the shear layer, in the main core, and partially in the wake. This was then completed for the scoured-bed bathymetry for comparison. At the end of a preliminary scour test, the bed was frozen in the entirety of the scour region and part of the depositional region. The area was painted darker gray to show the full extents (Figure 6.4).

The ADV data was then post-processed using the *HorizonADV* software provided by SonTek and analyzed in Microsoft Excel. Data taken over roughly 1-minute intervals at each location was monitored for quality; the sound-to-noise ratio (SNR) was consistenty greater than 15 decibels (dB), and the correlation exceeded 70% on average. Sampling near the water surface exposed the upper prong on the ADV responsible for collecting the vertical velocity component, resulting in predominantly error returns. The streamwise and transverse components were deemed reliable. In conjunction with the longitudinal and transverse location, these magnitudes we compared at the same location from pre- to post-experiment. This comparison is done in Section 8.4.

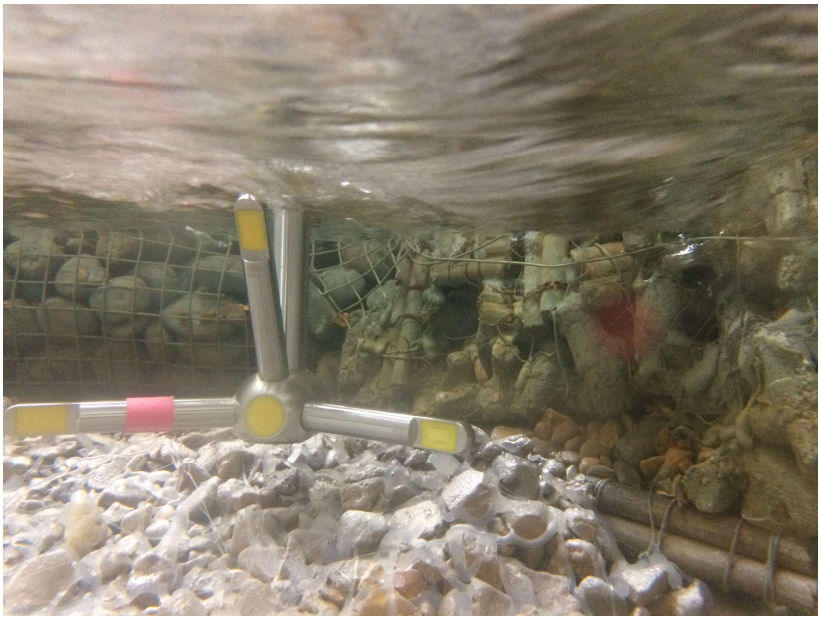

Figure 6.1. Side-looking SonTek ADV in flume.

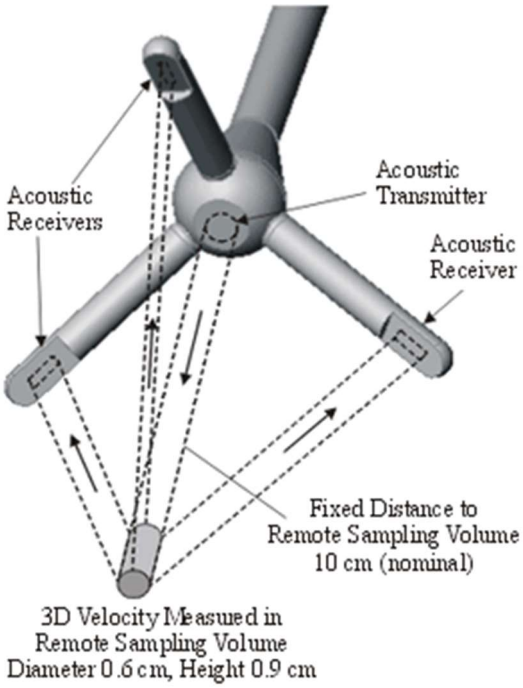

Figure 6.2. Schematic of ADV sampling volume (SonTek, 1998).

Figure 6.3. Frozen flat-bed bathymetry in gravel bed for ADV measurements.

Figure 6.4. Frozen scour bathymetry in gravel bed for ADV measurements.

6.4. Sonar continuous depth measurement

The most accurate and least intrusive manner of continuous depth measurements are with the use of sonar probes. When submerged, aquatic sonar probes can return an averaged number of depth readings over a short amount of time to track changes in bed elevation underneath the probe beam. While this method has shown success in tracking the migration of sand bedforms over time in a uniform bed (Friedrich, 2005), there is no comparable physical modelling information to the author's knowledge available for sonar depth experiments in non-uniform, gravel substrate. Before scour experiments were run, the accuracy of the probes must be validated using the Seatek 5MHz Ultrasonic Ranging System.

6.4.1. Single probe verification

In the conceptual phase of experimental design, the accuracy of the outputs collected by the sonar probes were verified by comparing the sonar returns with detailed point gage scour depth measurements along the same longitudinal transect of a scour hole at the equilibrium condition (i.e., after scour evolution had already occurred). This was done to ensure that the difference in elevation under the influence of the beam was consistently measured and had dependable results. This comparison yielded a Root Mean Square Error (RMSE) of approximately 2.4 mm, ($RMSE/d_{50} = 0.3$), illustrating the system's ability to take depth measurements over the non-uniform, mobile bed with high accuracy (Figure 6.5).

6.4.2. Sonar probe and testing array

A linear array of sonar probes was stationed along the thalweg transect of the expected scour extents in order to continuously capture scour evolution in the streamwise direction during the full scour trial duration. The experimental capabilities of the flume allowed for 4 (labeled 1 through 4) spaced 15 cm apart to be introduced to the flow at the water surface with minimal flow influence (Figure 6.6). Initial testing was completed with 8, but variability in scour depth and extents was minimized when reducing probe influence by increasing spacing. A zero-reading was gathered in stillwater conditions prior to test initiation, allowing for differential vertical placement to align with the rapidly varied water surface profile near the ELJ structure. During the trial, the sonar probes were stationed and activated for the full duration of scour development. These continuous sonar depth readings allow for a more complete understanding of the gravel-bed scouring process not otherwise gathered from comparison only of initial and equilibrium conditions.

6.4.3. Sonar data processing

With accuracy down to 0.1 mm, small incremental movement of gravel and gravel bedload movement at scour initiation created considerable noise in the data. The non-uniform water surface profile near the

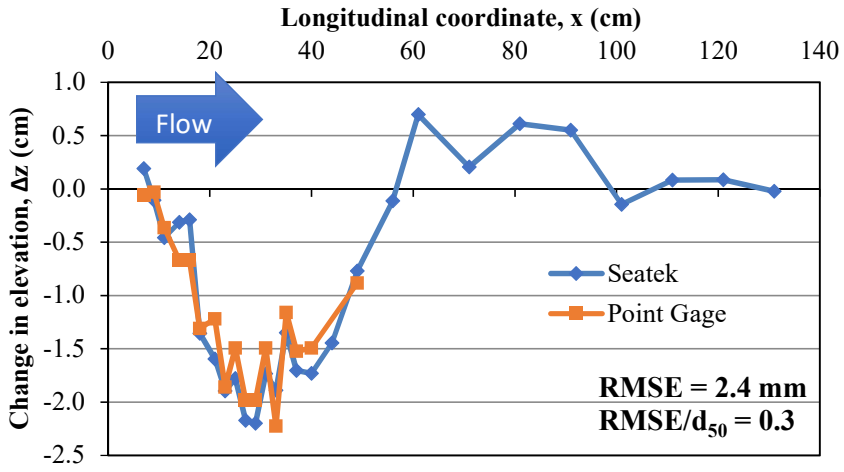

Figure 6.5. Verification comparison of point gage and sonar results for equilibrium scour hole.

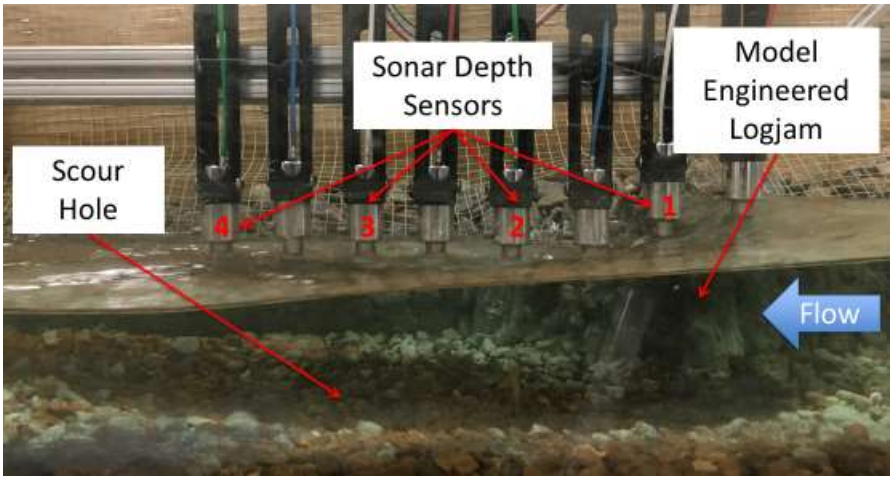

Figure 6.6. Profile view of sonar location relative to ELJ and developed scour hole.

structure created further experimental difficulties during data collection near the ELJ3 toe. As scour developed, the local water surface profile evolved, causing inconsistent probe submergence as the trial progressed. Chapter 7 illustrates the raw data outputs to the other three probes further downstream where the water surface profile was more consistent. This noise was removed using a filtering algorithm sequence in Matlab. A maximum/minimum threshold was used to immediately eliminate unrealistically large values. Median filtering and spike removal were employed to discern true depth measurements from bedload noise. Outlier removals were used to further remove data spikes a number of standard deviations away from window values. Linear interpolation was used at the end to fill in data gaps left by the previous steps. These filters were applied to the returns from each probe. This final time series attempts to capture the true scour evolution at that location while minimizing noise.

6.5. Semi-continuous velocity measurements

The flow depth during clearwater scour conditions was inadequate for intrusive velocity measurement (ADV) near the bed and along flume sidewalls. An indirect velocimetry method was needed to prevent the interruption of sediment transport processes co-evolving with localized water surface elevation near the ELJ structure. Readily-available non-intrusive imaging techniques, utilized in similar flume research (Admiraal, 2009), track discrete particles over known time and distance related to the physical model. Flow patterns can be qualitatively and quantitatively determined with techniques such as Large-Scale Image Velocimetry (LSIV) (Fujita et al., 1997), which capture water surface velocity patterns. The LSIV technique tracks particles (hot water in this experiment) using a pixelated interrogation radius and defined search area over which to correlate the particles in sequential images,

Hot water is poured into the reservoir shown in Figure 6.6 where it feeds at a constant rate though the hose and is distributed evenly across the flume width with the multi-nozzle sprinkler (Figure 6.7). The droplet movement, beginning approximately 0.50 m upstream of the test section, is recorded with an Infrared (IR) camera mounted above the observation area at a rate of 30 frames per second for a total of approximately 35 seconds (Figure 6.8). Images must be related to the physical model by relating physical and marks to pixel locations in the image; displacement of a known pixel distance as related to a known physical distance over a known time allows for unobstructed relative surface velocity measurements to be taken in 2D space. These correlated pixel movements yield instantaneous velocity vectors, which are averaged over the sequence duration and weighted to yield an averaged velocity field at the present state of scour hole evolution (Figure 6.9). This process is repeated periodically during the scour experiment to develop a timeline of spatial velocity distribution as bed topology evolves.

Figure 6.7. Hot water reservoir for supply during IR data collection.

Figure 6.8. Continuous, uniform hot water seeding during IR data collection.

Figure 6.9. IR camera mount for plan-view data collection at ELJ3.

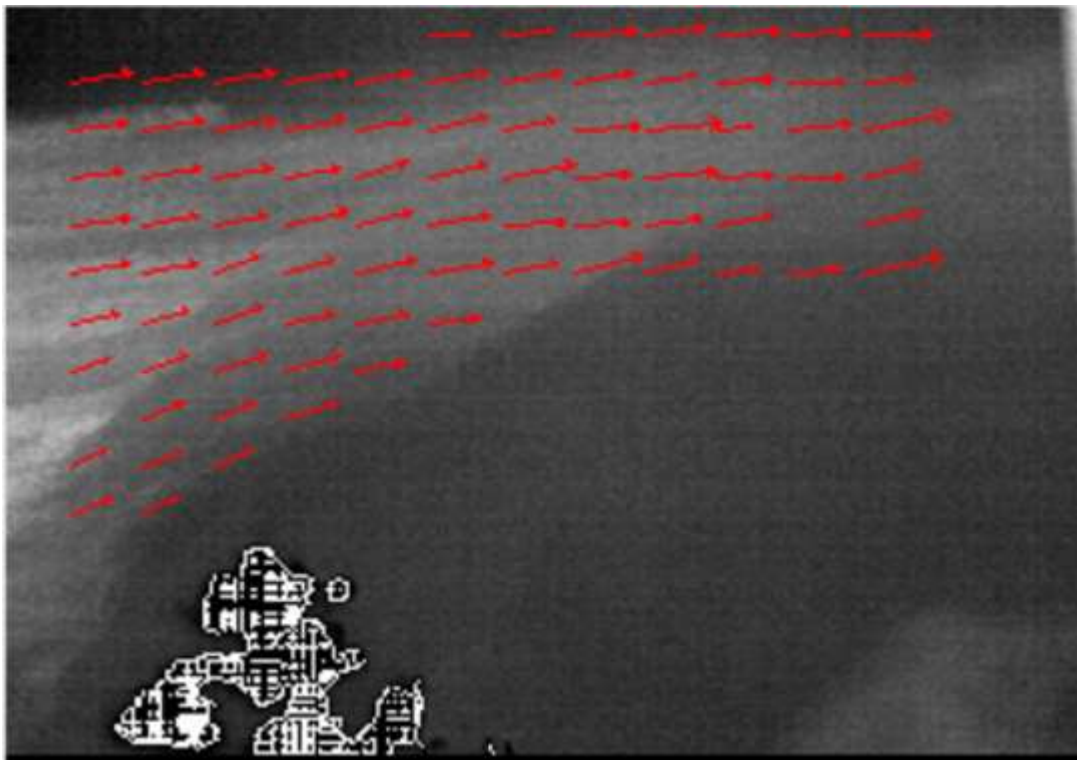

Figure 6.10. Example of surface velocity vectors at one point in scour evolution.

7. Results

7.1. Qualitative flow structure

To judge the model on its representation flow structure, qualitative dye tests were performed at the test flow conditions to visualize the characteristic flow structures at ELJ3. The dye met the upstream face, sending some flow downwards as the rest of the dye traveled via the primary vortex around the structure nose; the wake region was evident as wake vortices were shed inward back toward the bank in the region of slower flow (Figure 7.1). The shear layer illustrated where the dye in the secondary vortex and main core flow was repelled by the primary vortex (Figure 7.2). The wake area was most evident in Figure 7.3. where the dye was introduced with a single large pulse near the revetment. This dye plunged with the down flow, travelling around and through the permeable structure to reach the other side. This resulted in recirculation of dye in the wake region and an extended residence time.

7.2. Equilibrium scour hole geometry

Prior to investing effort into the complex sonar and infrared final measurements, we ensured that we could generate repeatable clearwater scour hole geometry using the methodological procedure detailed above. This methodological procedure, in conjunction with the discussion above on rigorous delineation of the critical condition, promotes consistency in the scour evolution results over the repeated 90-minute duration. Scour initiation was focused at the toe of the structure where streamlines are most constricted and erosive capacity is greatest (Koken and Constantinescu, 2014). Temporally, initiation was marked by an event moving larger clusters of particles that then reached a principal rate of scour commonly within the first 25 minutes of the test before approaching an equilibrium rate (Cardoso and Bettess, 1999). The maximum scour depth location at equilibrium developed predominantly downstream of the ELJ3 toe, similar to that of some wing-wall abutments with comparable structure protrusion length (Ettema et al., 2010). The maximum scour hole depths were consistently near 6 cm, yielding a variability of 6% that is near that of other accepted scour studies with a mobile bed (Papanicolaou et al., 2004). The equilibrium scour hole volumes, on average nearly 2850 cm^3, maintained an associated error of 7.1% that compares well with published values of scour volume (Kuhnle et al., 2002). Figure C.1-C.6. shows the point gage measurement grid and locations that scour depth data were taken for volumetric calculations. Using interpolation functions in Matlab, the bed contours were created (see Appendix C). Table 6.1 summarizes the scour volume and maximum scour depth of the preliminary trial runs.The preliminary clearwater scour tests show that a repeatable scour geometry is attainable. This ensured that we can generate reliable tests in terms of clear water scour formation and volume during the final runs where the detailed acquisition of flow and scour depth is attained.

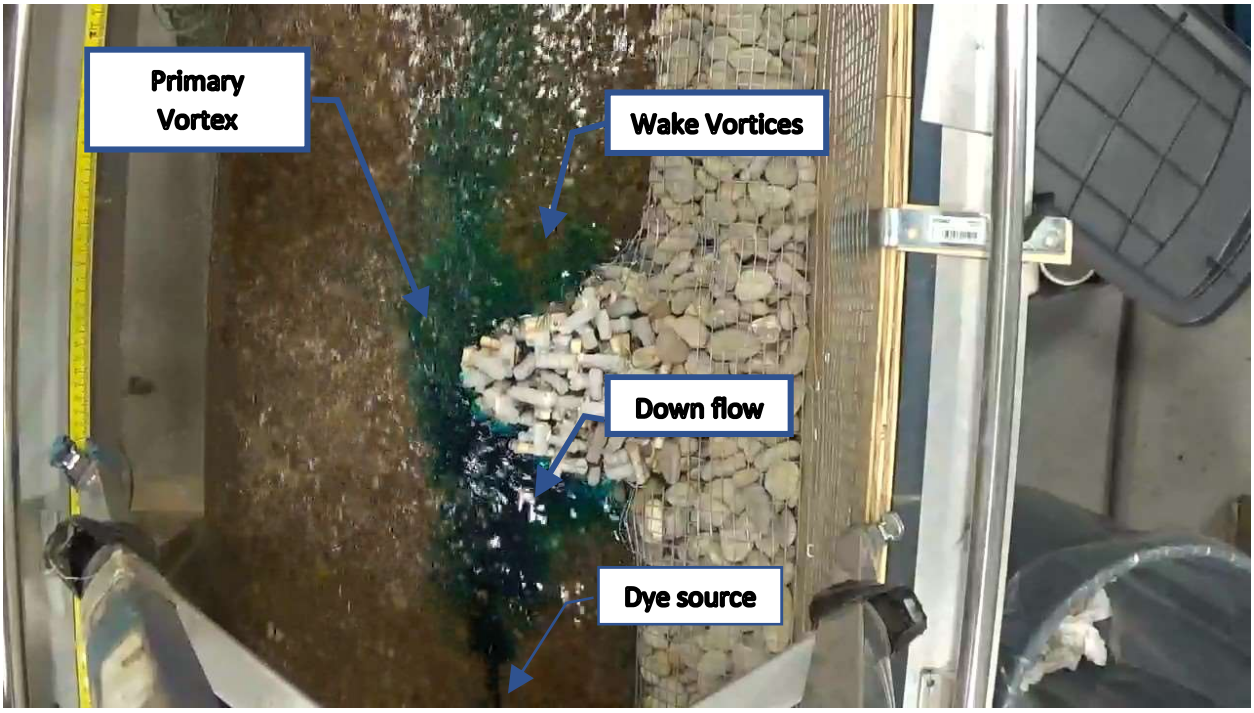

Figure 7.1. Model ELJ3 dye test illustrating location of down flow, primary vortex, and wake vortices.

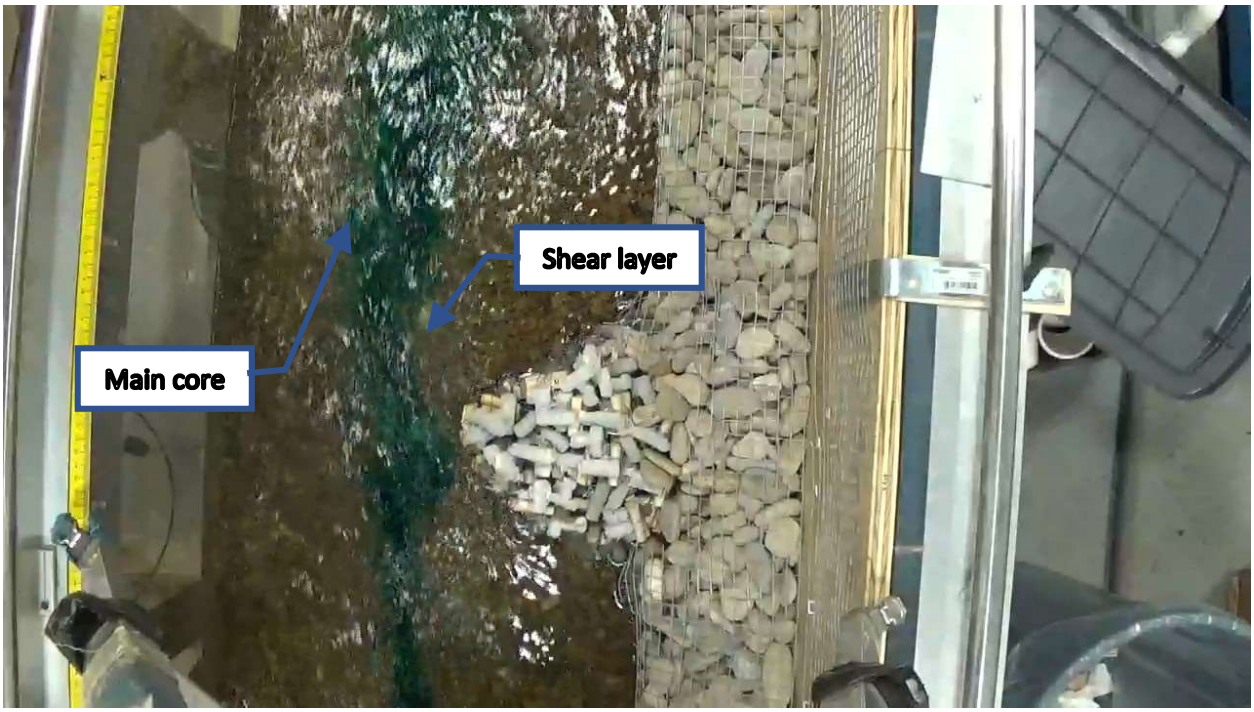

Figure 7.2. Model ELJ3 dye test illustrating shear layer formation and main core flow.

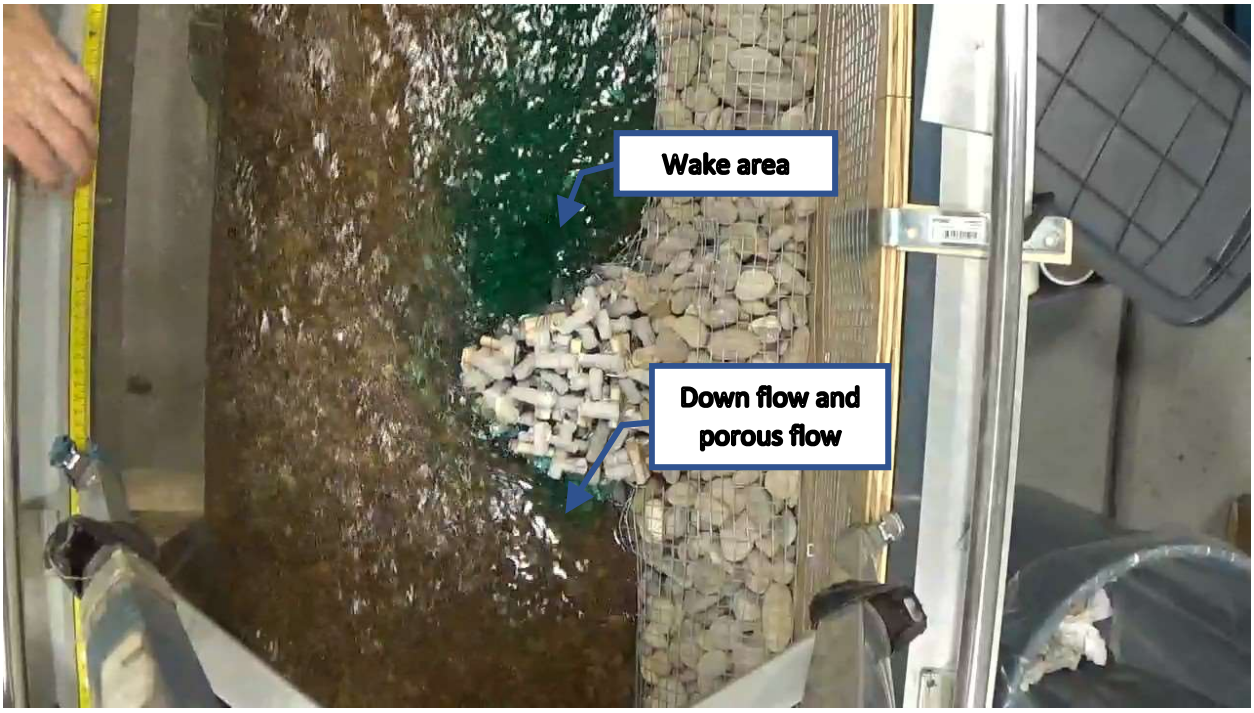

Figure 7.3. Model ELJ3 dye test showing down and porous flows that travel to wake area.

Table 7.1. Abbreviated test condition and scour results from Trials 1-5.

Trial #	Flow discharge, Q (m^3/s)	Approach flow depth, H (m)	Approach flow dimensionless shear stress, τ^* (-)	Maximum Scour Depth $d_{s,m}$ (cm)	Scour Hole Length (cm)	Scour Hole Volume (cm^3)
1	0.0205	0.082	0.0348	6.6	66.4	2923.7
2	0.0204	0.081	0.0344	6.2	69.5	2655.5
3	0.0205	0.083	0.0352	6.7	75.6	3033.8
4	0.0204	0.082	0.0348	5.9	65.2	2873.2
5	0.0206	0.082	0.0348	6.5	65.3	2831.0
Average				6.4	68.4	2863.4
Standard Deviation				0.3	4.4	138.8
Percent Variability (%)				6.3	8.0	7.1

7.3. Sonar continuous depth measurements

Discussed in previous literature, the scour rate curve is logarithmic in shape. Their scour depth reaches nearly 80% of the maximum within the first 20% of time (Kuhnle et al., 2002). Figure 7.4 details individual probe outputs during the test, with Probe 1 located right near the ELJ and Probe 4 approximately 40 cm downstream of the ELJ toe. Significant noise attributed to the evolving water surface elevation can be seen in the Probe 1 output as the readings toggled between two values for almost a third of the test duration. In Figure 7.5, the final readings from the continuous sonar outputs were overlaid on top of a point gauge longitudinal transect to validate the readings. Overall, the results were comparable to the stillwater tests with an RMSE = 2.1 mm ($RMSE/d_{50} = 0.25$).

These continuous measurements of scour depth at multiple locations in the scour hole have potential to improve the accuracy of decay functions in current scour approximation equations. Work has been done by other researchers (Li and Junke, 2016) in delineating a decay function (shear stress amplification vs. percent total expected maximum scour depth) of scour depth with respect to both time and stream power. However, these studies vary in applicability from the current project in that they utilize a limited number of points during scour evolution of a model sand bed to validate their decay envelope and CFD models. Utilizing a similar formulation approach, yet informing the data set with continuous scour measurements in a gravel bed, could lead to a more directly applicable understanding of gravel-bed scour processes and refined verification of hydrodynamic models that utilize the decay function.

7.4. Frozen bed velocity measurements

Displayed are ADV streamwise velocities in select location for the initial flatbed condition (Figure 7.6) and the equilibrium scoured bed condition (Figure 7.7). Velocities upstream of the ELJ increased during scour evolution as backwater effects were decreased due to the co-evolving water surface profile. Velocities downstream of the ELJ decreased as scour evolved, resulting in a local flow depth increase over time. This co-evolution of scour depth and velocity lends itself to temporal change in bed shear stress; combining both continuous depth-change readings and semi-continuous velocity readings may allow for the calculation of evolving bed shear stress at any point in scour evolution. This proof-of-concept exercise shows that utilizing non-invasive infrared velocity measurements, discussed in the following section, will allow for calculations of evolving bed shear stress and will further inform current understanding of shear stress decay in scour applications (Li and Guo, 2016).

7.5. Semi-continuous velocity measurements

The experiment was run at the initial flat-bed condition, where scour was then initiated and periodic measurements taken for surface velocity characterization until equilibrium was reached. Perspective

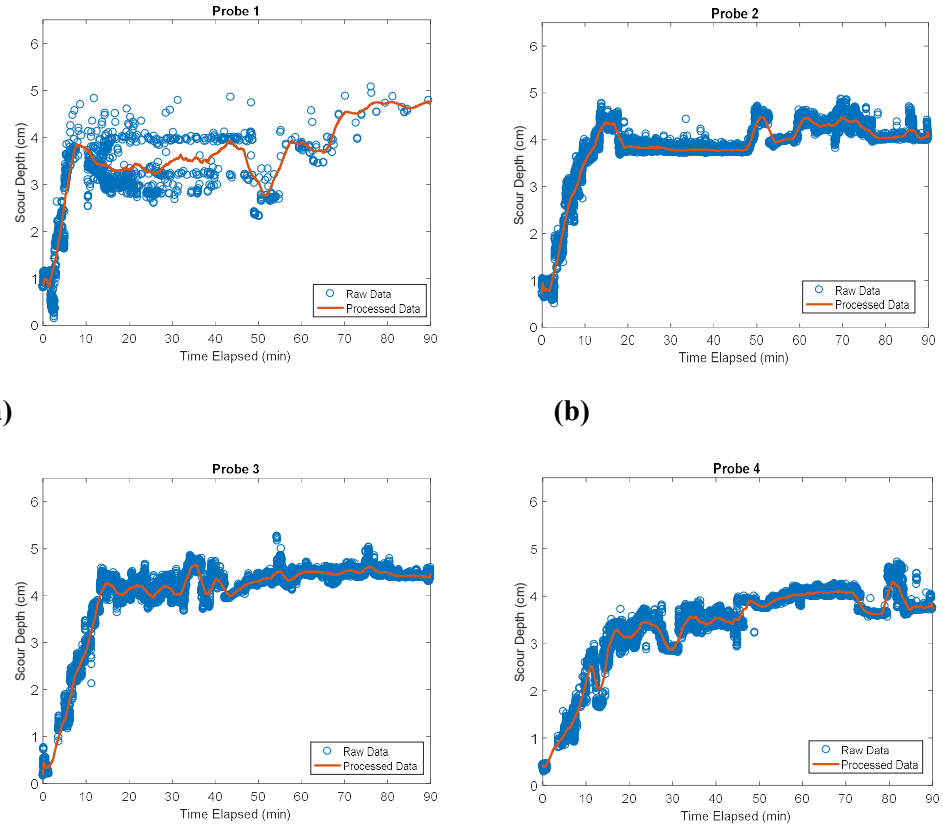

Figure 7.4. Raw and processed sonar depth returns for (a) Probe 1, (b) Probe 2, (c) Probe 3, and (d) Probe 4.

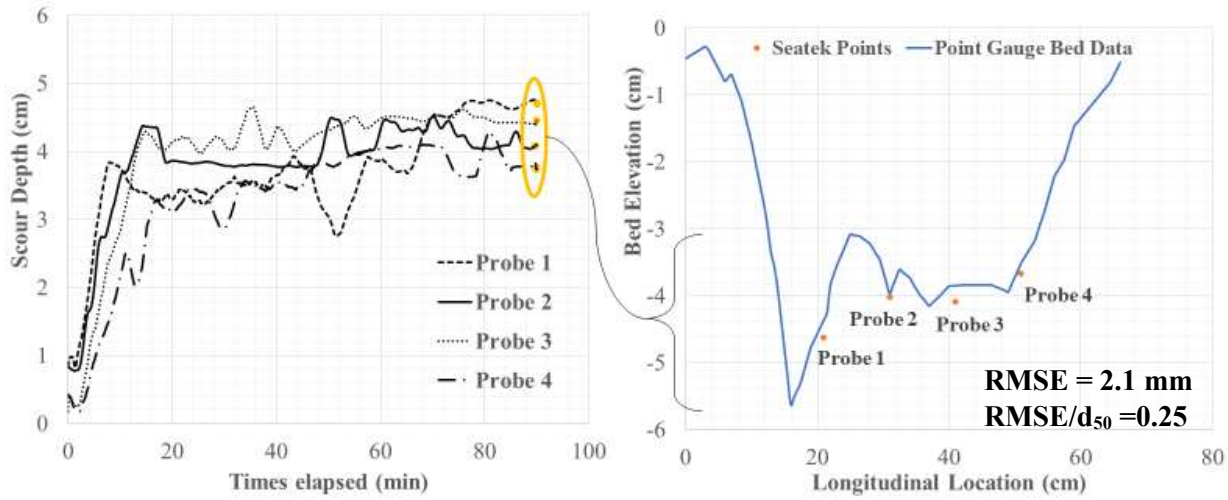

Figure 7.5 Sonar data for temporal monitoring during scour evolution compared with point gage scour hole transect at equilibrium.

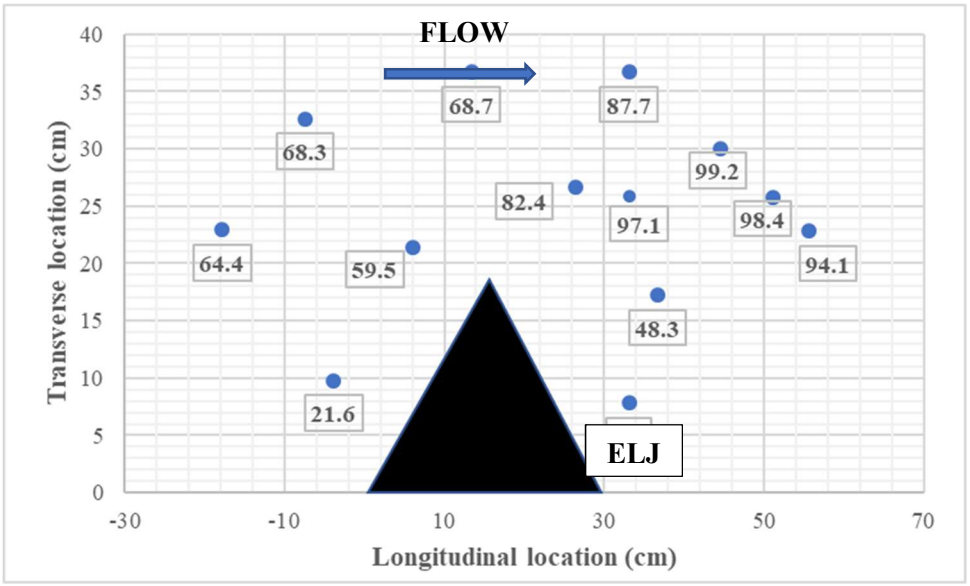

Figure 7.6. Measured ADV streamwise velocity values (cm/s) at select locations in test section pre-scour.

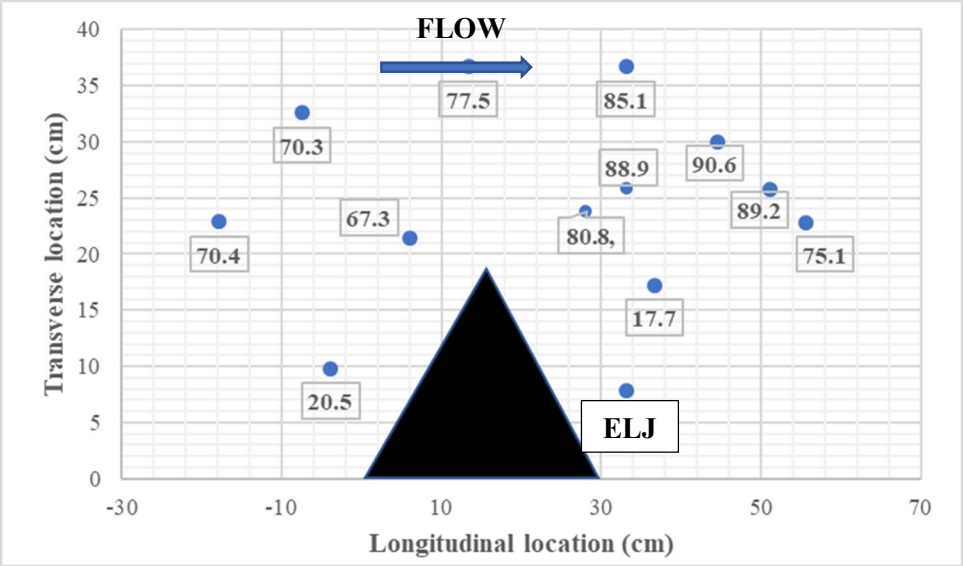

Figure 7.7. Measured ADV streamwise velocity values (cm/s) at select locations in test section at scour equilibrium.

photos were also taken of the scour hole evolution from initiation to equilibrium to relate the general scour bathymetry to the surface velocity measurements. The plots illustrate the overall trend of the faster moving streamlines (displayed as green and red contours) shifting as the scour hole develops and streamlines diverge (blue color contours) (Figure 7.8). The other LSIV outputs are shown in Appendix D. Table 7.2 illustrates that, on average, there was less than a 10% difference in ADV velocity magnitudes measured and the LSIV velocity returns. It was found during experimentation that the settings for LSIV software are crucial in getting a reliable output. Care should be given to input accurate velocity ranges and use a minimum acceptable correlation in post-processing in order to ensure quality. The conceptual proof of this methodology will allow for measurements of greater detail in future flow conditions. Considerations for the use of IR and LSIV over ADV measurements include potential instrument damage by highly mobile sediments in live-bed conditions, and increasingly complex sediment transport occurring during the scour process through cycles of both scour and deposition in the scour hole that may introduce a level of noise that yields inconclusive in-trial results.

Overall, it is shown that these semi-continuous IR velocity measurements, in conjunction with the continuous sonar scour depth measurements, can potentially yield a better understanding of the bed shear stress decay in gravel bed rivers as scour holes form. This understanding of stress change dependent upon current flow conditions rather than only the equilibrium condition is useful in parameterizing a robust scour depth estimation equation that can properly inform infrastructure risk with a more accurate scour depth estimation. The present study has illustrated physical methods of understanding bed shear stress decay and has set forth methods for upcoming work; the scour depth equation presented in this work evaluates the equilibrium condition only. Future work will benefit in using similar measurements in a live-bed condition to show a more complete picture of stress decay related to the scour evolution phenomenon seen in these gravel-bed experiments.

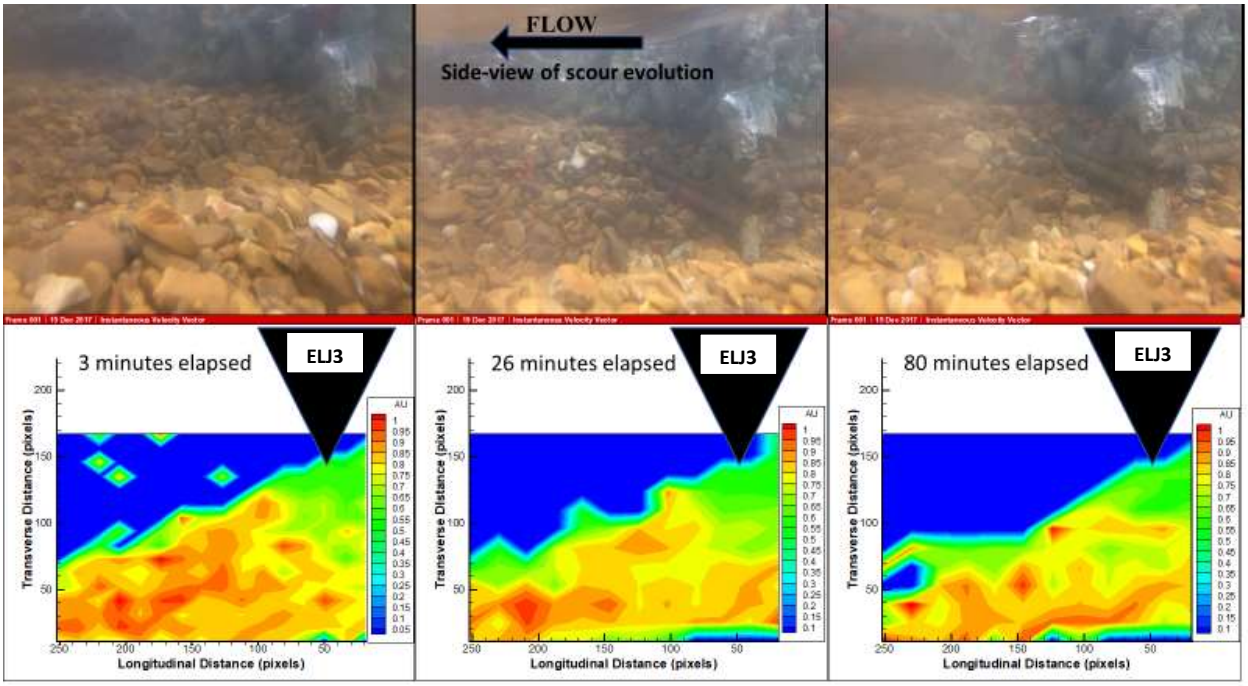

Figure 7.8. Relative velocity distributions from IR and side-view of scour evolution (AU in m/s).

Table 7.2. Comparison table of ADV and LSIV velocity magnitudes at same location.

ADV Velocity Value (cm/s)	LSIV Range (cm/s)	Maximum % Difference	Minimum % Difference
90.7	90 - 100	9.7	0.8
87.8	80 - 90	9.3	2.5
97.3	90 - 100	7.8	2.7
82.4	80 - 90	8.8	3.0
68.7	60 - 70	13.5	1.9

8. Discussion

8.1. Decay function formulation

Understanding the decay of bed shear stress as scour evolves is becoming an increasingly important factor in improving the accuracy of current scour equations. Tracking the changes in local flow depth, velocity, and bed shear stress during a flood event can provide valuable insight for forecasting scour depths when a certain vertical soil profile is known. With information on the critical soil resistance to shear in a river bed, flood plain, or substrate near hydraulic structure, there can be a more realistic gauge of scour capabilities or measure of structure failure likelihood at certain flows. While this work has been presently investigated in sand bed rivers, explaining this phenomenon in gravel bed rivers may be increasingly beneficial in preventing scour depth overestimation for the most widely occurring flow events at a location (Li and Guo, 2016). The findings of this study highlight the bed shear stress amplification at a permeable structure at a clearwater scour condition in a gravel bed.

The decay function is formulated using the total depth of flow and scour, y, near the location of maximum scour depth, as well as the surface velocity magnitudes, V, at the same location over the duration of the scour experiment. From these, a wall (bed) shear stress magnitude is calculated from the following equation detailed in Li and Guo (2016):

$$\tau_a = \rho g(V*n)^2/(R_h)^{1/3}$$

where τ_a is the wall shear stress and V is the local velocity. Using this equation, properties of the fluid, bed sediment roughness, and channel geometry are all considered in the delineation of bed shear. This bed shear stress is tracked throughout the entire evolution of the scour hole as surface velocity measurements are taken semi-continuously. In order to communicate the results in a dimensionless manner, the bed shear decay is put in terms of the minimum bed shear for the flow condition as scour equilibrium is reach. This is the bed shear amplification, τ_{amp}, shown in the equation below,

$$\tau_{amp} = \tau_a/\tau_{a,min}$$

where $\tau_{a,,min}$ is the minimum bed shear stress associated with the equilibrium condition. The evolution of bed shear is tracked with the paired dimensionless relationship of

$$Y/Y_{max}$$

Where Y is the temporally related maximum combined flow and scour depth, and Y_{max} is the maximum combined flow and scour depth associated with the experimental scour equilibrium. Assuming an

exponential decay in shear stress as is displayed by the work of Li and Guo (2016), the form of the bed shear stress decay function in terms of decreasing bed shear amplification should be in the form of

$$\tau_{amp} = a * exp\ (b * 100\%) = 1$$

$$\tau_{amp} = a * exp\ (b * 0\%) = a = 1.945$$

such that a is the bed shear amplification at the beginning of the test and that the bed shear amplification at the end of the test approaches the equilibrium condition of 1. Therefore, the decay function of bed shear stress in gravel beds around a permeable structure is

$$\tau_{amp} = 1.945 * exp\ (-0.665 * Y/Y_{max})$$

In Table 8.1, results are summarized for the relationship of τ_{amp} and Y/Y_{max}. The comparison of experimental data (HSL Data), the above bed shear stress decay function (HSL Decay), and an exponential trendline for the data are shown in Figure 8.1 and agree well with one another. To compare with a present study by Li and Guo (2016) on bed shear stress decay around a rectangular bridge pier in a sand bed model, the experimental data (Li Data) was included in Figure 8.2 to illustrate the difference in evolution from a uniform sand bed (Li Decay) to non-uniform gravel bed (HSL Decay). Overall, the bed shear stress decayed at a significantly slower rate in this study as compared to that Li and Guo (2016). This may be due to the increased particle interlocking of non-uniform gravel particles, leading to armoring as smaller particles are initially transported out of the scour hole at a faster rate. The use of a porous structure, as denoted in the literature review to decrease acceleration and scour at the structure toe, may also limit the bed shear amplification. Ultimately, this co-evolving relationship of scour depth and bed shear stress as scour occurs shows that the temporal evolution of scour in gravel bed rivers is likely overestimated over time when assumptions of a uniform bed or impermeable structure are made.

8.2. Formulation of Gravel Bed Scour Equations

8.2.1. Model Parameterization and Projected Prototype Scour

In order to use model results to project to prototype conditions at the Skagit River, we utilize the parameterization of Maxwell and Papanicolaou (2000) to nondimensionalize both the flow conditions and the maximum scour depth as follows. During the scour tests, values of volumetric discharge (Q), average flow depth (H), mean particle diameter (d_{50}), and geometric particle standard deviation (σ_g) were taken during each trial. These parameters were dimensionally consolidated in order to scale the model flow

Table 8.1. Measurements of scour depth and shear stress over duration of experiment.

Time	Normalized Time	Percentage of total scour depth	LSIV Surface Velocities	Wall shear stress	Dimensionless bed shear stress	Bed Shear Amplification
T_i (min)	T_i/T_t	Y/Y_{max}	V (cm/s)	τ_a (Pa)	τ^*	τ_a/τ_{min}
0.0	0.00	0	65	8.79	0.067	1.94
2.5	0.03	26	58.7	7.07	0.054	1.56
6.3	0.07	68	54.7	6.02	0.046	1.33
9.8	0.11	79	53.9	5.82	0.044	1.29
13.5	0.15	73	55.7	6.23	0.047	1.38
17.0	0.19	69	52.4	5.52	0.042	1.22
21.3	0.24	72	51.5	5.33	0.040	1.18
25.5	0.28	68	56.4	6.40	0.049	1.42
30.0	0.33	73	55.9	6.28	0.048	1.39
35.0	0.39	74	51.3	5.28	0.040	1.17
40.0	0.44	77	53.9	5.83	0.044	1.29
44.0	0.49	81	52.4	5.50	0.042	1.22
50.0	0.56	64	56.5	6.44	0.049	1.42
57.0	0.63	80	50.6	5.13	0.039	1.14
65.0	0.72	77	50.1	5.03	0.038	1.11
72.0	0.80	95	52	5.39	0.041	1.19
80.0	0.89	99	52	5.38	0.041	1.19
90.0	1.00	100	50.1	5.00	0.038	1.11

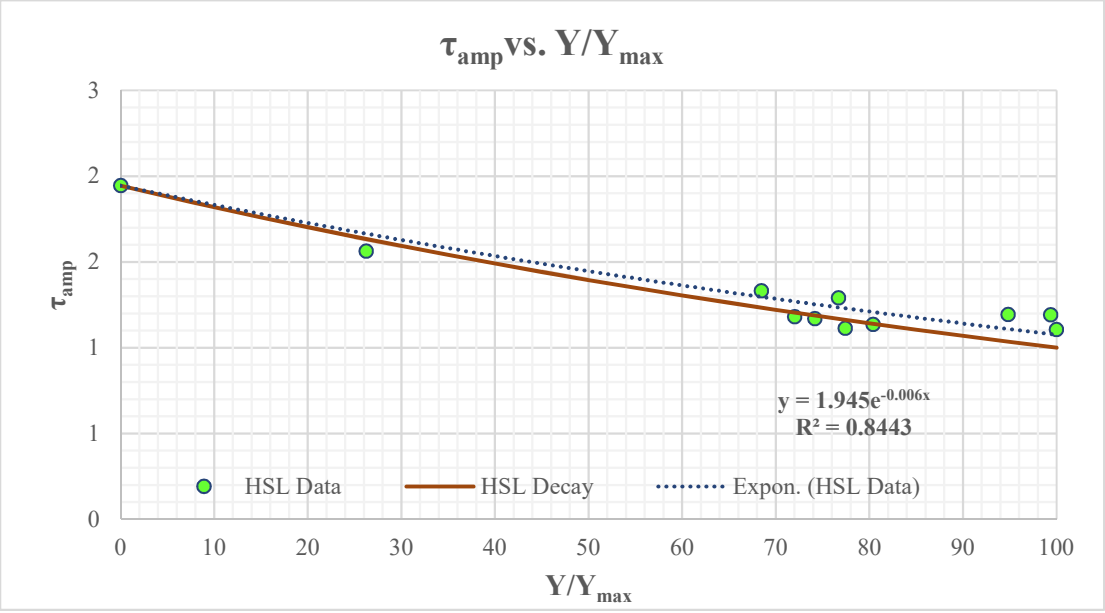

Figure 8.1. Decay Function of wall shear stress around permeable ELJs in gravel bed.

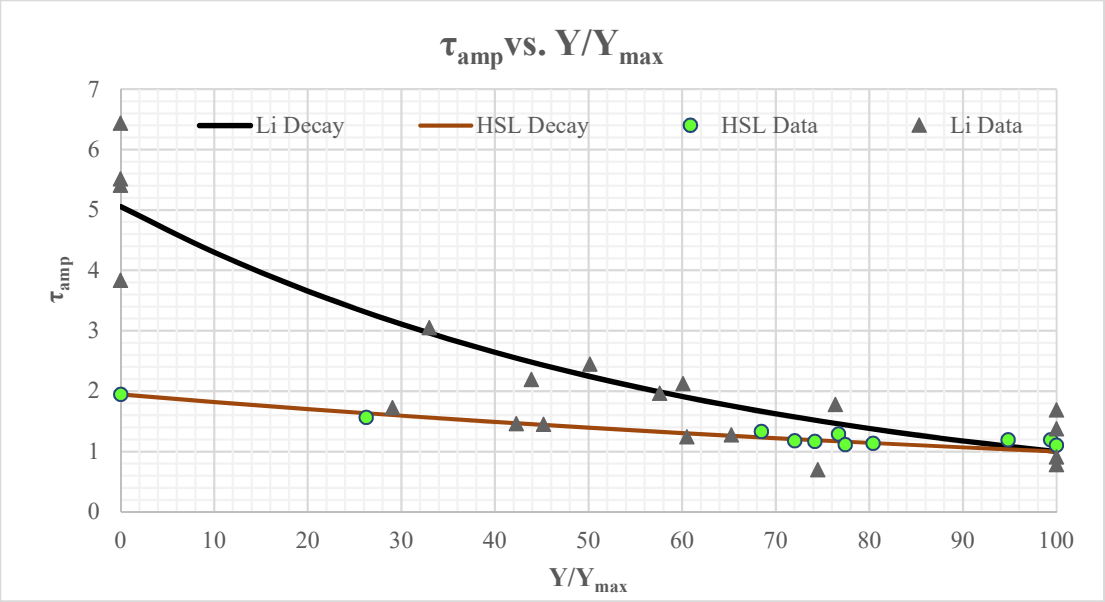

Figure 8.2. Decay function of wall shear stress around permeable ELJs in gravel bed including data of Li and Guo (2016).

depth by relating to discharge intensity, expressed as $\frac{Q}{\sqrt{gH^5}}$. Analysis of the data yield the conclusion that the scour depth is function of the following parameters: the ratio of mean particle diameter and depth, the discharge intensity, and the geometric standard deviation of the gravel bed. This relationship is illustrated below:

$$\frac{d_{sm}}{H}\sigma_g{}^{0.25} = f\left(\frac{d_{50}}{H}, \frac{Q}{\sqrt{gH^5}}\right)$$

The substitution of the model flow depth, particle size distribution, and discharge yielded a dimensionless parameter shown above as value 0.1009. To relate these test conditions to prototype conditions, the two dimensionless ratios must be equivalent. Scaling of the physical model and its outputs was based upon the flow depth, particle size distribution, and discharge from the prototype ELJ field installation. Using provided cross-sectional GIS data and hydrologic information included in the hydraulic analysis report provided by Northwest Hydraulic Consultants as inputs, a stage-discharge curve was developed at the ELJ3 location using the HydroCalc software (Figure 8.3). This curve includes only data from USGS gauging station #12184700 from the Skagit River at Rockport and may decrease in accuracy when extrapolating outside of these flow conditions.

By utilizing the fitted polynomial equation in Figure 8.3, the corresponding prototype stage (H_p) is nearly 6.8 ft and the corresponding discharge (Q_p) is 21,300 cfs. This value is lower than the published prototype bankful discharge value of 33,000 cfs put forth by USGS.

A ratio of geometric standard deviations of the particle size distributions of the model are used as a parameterization of the pertinent sediment properties also necessary to qualitatively scale the model results to prototype scour depths. From field pebble counts and laboratory bed size distributions, the geometric standard deviations were calculated to be 1.47 and 1.46, respectively. The ratio of flow depths during comparable flow discharge is set as the calculated prototype flow depth divided by the measured model flow depth, $\frac{H_p}{H_m}$. This value, multiplied by the root of the geometric standard deviation relationship and the measured model scour depth, yield this qualitatively scaled prototype scour depth equation below. Tables 8.2 and 8.3 show the qualitatively scaled prototype scour depths related to selected model scour trials using the equation below. The resultant scour depths maintain a level of experimental variability of ±6% as seen similarly in other gravel bed scour studies (Papanicolaou et al., 2004).

$$\boldsymbol{d_{s,p} = d_{s,m}\left(\frac{H_p}{H_m}\right)\left(\frac{\sigma_{g,m}}{\sigma_{g,p}}\right)^{0.5}}$$

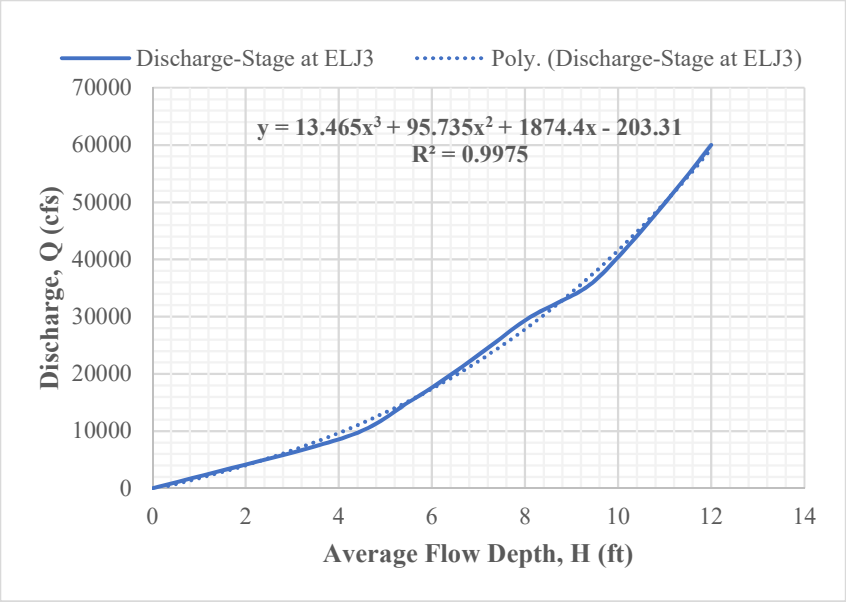

Figure 8.3. Prototype discharge-stage relationship at ELJ3.

Table 8.2. Summary table of model results related to prototype scour conditions and results.

Model Test Conditions			Prototype Projected Conditions			
Flow discharge, Q_m (m^3/s)	**Approach flow depth, H_m (m)**	**Maximum Scour Depth $d_{s,m}$(cm)**	**Flow discharge , Q_p (ft^3/s)**	**Approach Flow Depth, H_p (ft)**	**H_p/H_m**	**Maximum Scour Depth $d_{s,p}$ (ft)**
0.0204 +/- 0.5%	8.1 +/- 1.2%	6.3 +/- 6.3%	21,300	6.8	25.3	5.2 +/- 6.5%

Table 8.3. Experimental testing conditions and associated prototype results.

Trial #	Flow rate, Q_m (m^3/s)	Approach flow depth, H_m (m)	Max. Scour Depth, $d_{s,model}$(cm)	Scour Hole Volume, (cm^3)	Approach Flow Depth, H_m (ft)	H_p/H_m	Max.Scour Depth, $d_{s,prototype}$ (ft)
1	0.0205	0.082	6.6	2923.7	0.269	25.4	5.5
2	0.0204	0.081	6.2	2655.5	0.266	25.7	5.2
3	0.0205	0.083	6.7	3033.8	0.272	25.0	5.5
4	0.0204	0.082	5.9	2873.2	0.269	25.4	4.9
5	0.0206	0.082	6.5	2831.0	0.269	25.4	5.4

9. Conclusion

9.1. Observations

This research project has provided unique insights about the feedbacks between an ELJ structure, flow, and gravel bed under clearwater scour conditions. The findings in this research show that the scour hole in the vicinity of the ELJ obtains a conical shape and that the average time to reach an equilibrium state for the model is about 20 minutes. Although time to equilibrium cannot currently be directly related to that of the prototype without some efforts on prototype scour data reconciliation, the overall trend of logarithmic scour growth over time match that of other gravel bed scour studies (Papanicolaou et al., 2017). Flow measurements complemented the scour measurements and provided rare data about the decay function of the bed shear stress in gravel-bed rivers as the scour hole develops. Analysis of the rate of scour hole growth and the rate of the shear stress decay shows nearly identical rates. The strong correspondence between scour growth and bed shear stress decay substantiated the central hypothesis of this research pertinent to the interplay between flow and gravel bed grains. The parameterization of scour from Maxwell and Papanicolaou (2000) was adopted to predict maximum scour depth under equilibrium conditions for the clearwater case in the following equation:

$$d_{s,p} = d_{s,m}\left(\frac{H_p}{H_m}\right)\left(\frac{\sigma_{g,m}}{\sigma_{g,p}}\right)^{0.5}$$

The scour formula accounts for grain size gradation and changes in the flow depth between the approach flow and the flow in the vicinity of the ELJ. In addition, consideration of Ettema et al., 2010 for the experimental conditions yielded values similar values (1.52 and 1.95, respectively) for the maximum bed shear stress amplification that accounts for the excess shear stress development around the structure in the Ettema and HSL experiments. Analysis of the velocity measurements obtained in this study showed that the increase in magnitude of the bed shear stress along the shear layer is comparable to the shear stress increase reported in the literature (Ettema et al., 2010).

This research was not only a fundamental contribution to the state of current knowledge, but also some practical outcomes. First, it was shown by visual and quantitative tests that the ELJ structure effectively deflected the flow away from the bankline, the toe of the structure remained intact, and the maximum scour hole depth formed away from the structure. These findings suggest that a permeable structure similar to the ELJ can be an effective flow deflector in gravel bed rivers as an alternative to impermeable hydraulic structures that would otherwise have minimal porosity, increased acceleration around, increased capacity for scour, and decreased interstitial space for ecological benefit.

9.2. Future work

The findings of this research show the value and importance of conducting a detailed experimental design that considers aspects of hydraulic-dynamic similarity for flow and sediment. Although the setup of the proposed experiments was not an exact replication of the prototype, nonetheless, the study ensured that the submergence of the structure, average structure layering and porosity, as well as bed sediment grain size distribution mimicked the prototype conditions. Flume limitations such as channel width did not permit the exact replication of the plan-form geometry found in the case study location (i.e. Skagit River). Future research should consider the use of a wider flume facility to enable a closer replication of the prototype conditions in terms of plan-form geometry and minimize the role of wall effects.

Future research should also extend this work from clearwater scour conditions to live-bed scour conditions. A comparative study between the two phases of scour (clearwater and live-bed) will lead to the development of a more generic scour formula that considers the effect of incoming sediment on scour volume under live-bed scour conditions.

As well, more work may be done understanding the clogging of ELJ pores with sediment and wood debris and the associated flow structures around and though the ELJ as it begins to increasingly behave like an abutment.

This research is a first step in utilizing nearly synchronous flow and depth measurements and can become the keystone for future experimental work in scour and gravel bed rivers.

Bibliography

Abbe, Timothy B., and David R. Montgomery. "Large woody debris jams, channel hydraulics and habitat formation in large rivers." Regulated Rivers Research & Management 12.23 (1996): 201-221.

Abbe, Tim, et al. “New Innovative, Habitat-Creating Bank Protection Method.” World Environmental and Water Resources Congress 2011, 2011, doi:10.1061/41173(414)211.

Ahmed, Ferdous, and N. Rajaratnam. "Observations on flow around bridge abutment." Journal of Engineering Mechanics 126.1 (2000): 51-59. Allan, J.D., and A.S. Flecker. 1993. Biodiversity conservation in running waters. Bioscience 43:32–43.

Anderson, Alvin G., Amreek S. Paintal, and John T. Davenport. "Tentative design procedure for riprap-lined channels." (1970).

Bagočius, Donatas. “Piling Underwater Noise Impact on Migrating Salmon Fish during Lithuanian LNG Terminal Construction (Curonian Lagoon, Eastern Baltic Sea Coast).” Marine Pollution Bulletin, vol. 92, no. 1-2, 2015, pp. 45–51., doi: 10.1016/j.marpolbul.2015.01.002.

Barbhuiya, Abdul Karim, and Subhasish Dey. "Vortex flow field in a scour hole around abutments." International Journal of Sediment Research 18.4 (2003): 310-325.

Barbhuiya, Abdul Karim, and Subhasish Dey. "Local scour at abutments: A review." Sadhana 29.5 (2004): 449-476.

Bennett, Sean J., et al. "Flow, turbulence, and drag associated with engineered log jams in a fixed-bed experimental channel." Geomorphology 248 (2015): 172-184.

Bettess, R., et al. "DISCUSSION. TECHNICAL NOTE. INITIATION OF SEDIMENT TRANSPORT IN GRAVEL STREAMS." Proceedings of the Institution of Civil Engineers 77.4 (1984): 523-524.Blodgett, J.C. 1986. Rock riprap design for protection of stream channels near highway structures, Vol. 1—Hydraulic characteristics of open channels. U.S. Geological Survey. Water-Resources Investigations Report 86–4127. Denver, CO.

Bocchiola, D. "Hydraulic characteristics and habitat suitability in presence of woody debris: a flume experiment." Advances in water resources 34.10 (2011): 1304-1319.

Bolton, S., A. Watts, T. Sibley, and J. Dooley. 1998. A pilot study examining the effectiveness of engineered large woody debris (ELWD TM) as an interim solution to lack of LWD in streams. EOS, Trans. of the Amer. Geophysical Union 79(45): F346.

Brownlie, William R. "Prediction of flow depth and sediment discharge in open channels." (1981).

Buffington, John M. Effects of hydraulic roughness and sediment supply on surface textures of gravel-bedded rivers. MS thesis. University of Washington, 1995.

Buffington, John M., and David R. Montgomery. "A systematic analysis of eight decades of incipient motion studies, with special reference to gravel-bedded rivers." Water Resources Research 33.8 (1997): 1993-2029.

Buffington, John M. "The legend of AF Shields." Journal of Hydraulic Engineering 125.4 (1999): 376-387.

Bunte, Kristin, and Steven R. Abt. "Sampling surface and subsurface particle-size distributions in wadable gravel-and cobble-bed streams for analyses in sediment transport, hydraulics, and streambed monitoring." (2001).

Cardno Entrix. “Skagit River Bank Protection 90% Design Support: SR 20 at Milepost 100.7.” Draft Design Report (November 2011).

Cardoso, A. H., and R. Bettess. "Effects of time and channel geometry on scour at bridge abutments." Journal of Hydraulic Engineering 125.4 (1999): 388-399.

Castro, J., and R. Sampson. "Incorporation of large wood into engineering structures." Natural Resource Conservation Service Engineering Technical Note no 15 (2001).

Cederholm, C. J., et al. "Response of juvenile coho salmon and steelhead to placement of large woody debris in a coastal Washington stream." North American Journal of Fisheries Management 17.4 (1997): 947-963.

Chang, H. H. Fluvial processes in river engineering, Krieger Publishing Company, Malabar, Florida (1998).

Chow, Ven Te. Open-Channel Hydraulics. The Blackburn Press, 2009.

“Cle Elum River Instream Habitat and Side Channel Restoration Project.” Kittitas Conservation Trust, ENTRIX Environmental Consultants, 31 Jan. 2008, kittitasconservationtrust.org/cle-elum-river.php.

Coleman, Stephen E., Christine S. Lauchlan, and Bruce W. Melville. "Clear-water scour development at bridge abutments." Journal of Hydraulic Research 41.5 (2003): 521-531.

D'Aoust, Stephane G. Large woody debris fish habitat structure performance and ballasting requirements. Diss. University of British Columbia, 1998.

D'Aoust, Stéphane G., and Robert G. Millar. "Stability of ballasted woody debris habitat structures." Journal of Hydraulic Engineering 126.11 (2000): 810-817.

Dey, Subhasish, and Abdul Karim Barbhuiya. "Clear-Water Scour at Abutments in Thinly Armored Beds." Journal of Hydraulic Engineering, vol. 130, no. 7, 2004, pp. 622–634., doi:10.1061/(asce)0733-9429(2004)130:7(622).

Dey, Subhasish, and Abdul Karim Barbhuiya. "Flow Field at a Vertical-Wall Abutment." Journal of Hydraulic Engineering, vol. 131, no. 12, 2005, pp. 1126–1135., doi:10.1061/(asce)0733-9429(2005)131:12(1126).

Diab, Reda, Oscar Link, and Ulrich Zanke. "Geometry of developing and equilibrium scour holes at bridge piers in gravel." Canadian Journal of Civil Engineering 37.4 (2010): 544-552.

Duan, Jennifer G., et al. "Mean flow and turbulence around experimental spur dike." Advances in Water Resources 32.12 (2009): 1717-1725.

Elhakeem, Mohamed, et al. "A Probabilistic Model for Sediment Entrainment: The Role of Bed Irregularity." International Journal of Sediment Research, vol. 32, no. 2, 2017, pp. 137–148., doi:10.1016/j.ijsrc.2016.11.001.

Ettema, R., Nakato, T., and Muste, M., NCHRP Report 24-20: ESTIMATION OF SCOUR DEPTH AT BRIDGE ABUTMENTS. Transportation Research Board of the National Academies, Washington D.C., 2010.

Eubanks, C., and Dexter Meadows. A soil bioengineering guide for streambank and lakeshore stabilization. Vol. 683. US Dept. of Agriculture Forest Service, Technology and Development Program, 2002.

Ferro, Vito. "ADV measurements of velocity distributions in a gravel-bed flume." Earth Surface Processes and Landforms 28.7 (2003): 707-722.

Fetherston, Kevin L., Robert J. Naiman, and Robert E. Bilby. "Large woody debris, physical process, and riparian forest development in montane river networks of the Pacific Northwest." Geomorphology 13.1-4 (1995): 133-144.

Finney, K. "History of soil bioengineering." Eleventh annual California salmonid restoration federation conference, Eureka, CA. 1993.

Fox, James F., et al. "Fluid-sediment dynamics around a barb: an experimental case study of a hydraulic structure for the Pacific Northwest." Canadian Journal of Civil Engineering 32.5 (2005): 853-867.

Fox, James F., and Brian J. Belcher. "Comparison of macroturbulence measured using decomposition of PIV, ADV and LSPIV data." Journal of Hydraulic Research 49.1 (2011): 122-126.

Friedrich, H., Melville, B. W., Coleman, S. E., Nikora, V. I., and Clunie, T. M. Three-dimensional measurement of laboratory submerged bed forms using moving probes. In Proceedings of XXXI International Association of Hydraulic Engineering and Research Congress (pp. 396-404). 2005.

Friedrich, H., Melville, B. W., Coleman, S. E., Clunie, T. M., Nikora, V. I., and Goring, D. G. Three-dimensional properties of laboratory sand waves obtained from two-dimensional autocorrelation analysis. In Int. Conf. on Fluvial Hydraulics, River Flow 2006, Lisbon, Portugal, 6-8 September 2006 (pp. 1013-1022). 2006.

Frissell, Christopher A., and Richard K. Nawa. "Incidence and causes of physical failure of artificial habitat structures in streams of western Oregon and Washington." North American Journal of Fisheries Management 12.1 (1992): 182-197.

Fujita, Ichiro, Marian Muste, and Anton Kruger. "Large-scale particle image velocimetry for flow analysis in hydraulic engineering applications." Journal of hydraulic Research 36.3 (1998): 397-414.

Gallisdorfer, Michael S., et al. “Physical-Scale Model Designs for Engineered Log Jams in Rivers.” *Journal of Hydro-Environment Research*, vol. 8, no. 2, 2014, pp. 115–128., doi:10.1016/j.jher.2013.10.002.

Gessler, Johannes. "Beginning and ceasing of sediment motion." River mechanics 1 (1971): 7-1.

Ghodsian, Masoud, and SM Hoseini Tehrani. "Scour around groins." International Journal of Sediment Research 16.1 (2001): 60-68.

Giri, S. and Shimizu, Y. “A method for local scour prediction at river structures considering time factor.” *Annual Journal of Hydraulic Engineering*, JSCE, 49, (2005), 781-786.

Green, T. PIV in practice (Doctoral dissertation, Luleå tekniska universitet), 2011.

Guan, Dawei, Bruce W. Melville, and Heide Friedrich. "Live-bed scour at submerged weirs." Journal of Hydraulic Engineering141.2 (2014): 04014071.

Hall, Megan, and Steve Moler. “Mimicking Mother Nature.” Public Roads, Federal Highway Administration, 1 Jan. 2006, www.fhwa.dot.gov/publications/publicroads/06jan/05.cfm.

House, Robert, and Val Crispin. Economic analyses of the value of large woody debris as salmonid habitat in coastal Oregon streams. Bureau of Land Management, 1990.

Ismael, Adnan, et al. “Effect of Bridge Pier Position on Scour Reduction According to Flow Direction.” Arabian Journal for Science and Engineering, vol. 40, no. 6, 2015, pp. 1579–1590., doi:10.1007/s13369-015-1625-x.

Jackson, E., Admiraal, D., Alexander, D., Stansbury, J., Guo, J., Rundkuist, D., Drain, M. Thermal imaging for discharge and velocity measurements in open channels. In: 33rd International Association of Hydraulic Research Symposium. International Association for Hydro-Environment Engineering and Research, Vancouver, Canada, 2009.

Judge, Aaron. Measurement of the hydraulic conductivity of gravels using a laboratory permeameter and silty sands using field testing with observation wells. University of Massachusetts Amherst, 2013.

Justice, Casey, et al. "Can stream and riparian restoration offset climate change impacts to salmon populations?" Journal of environmental management 188 (2017): 212-227.

Kennedy, John F. "The Albert Shields Story." Journal of Hydraulic Engineering 121.11 (1995): 766-772.

Kimmerer, Robin Wall, and T. F. H. Allen. "The role of disturbance in the pattern of a riparian bryophyte community." American Midland Naturalist (1982): 370-383.

Koken, Mete, and George Constantinescu. “Flow and Turbulence Structure around Abutments with Sloped Sidewalls.” Journal of Hydraulic Engineering, vol. 140, no. 7, 2014, p. 04014031., doi:10.1061/(asce)hy.1943-7900.0000876.

Komar, Paul D. "Selective gravel entrainment and the empirical evaluation of flow competence." Sedimentology 34.6 (1987): 1165-1176.

Kothyari, Umesh C., Ram Chandra J. Garde, and Kittur G. Ranga Raju. "Temporal variation of scour around circular bridge piers." Journal of Hydraulic Engineering 118.8 (1992): 1091-1106.

Kothyari, U. C., and K. G. Ranga Raju. "Scour around spur dikes and bridge abutments." Journal of hydraulic research 39.4 (2001): 367-374.

Kuhnle, R. A., Incipient motion of sand-gravel sediment mixtures, J. Hydraul. Eng., 119, 1400-1415, 1993.

Kuhnle, Roger A., Carlos V. Alonso, and F. Douglas Shields Jr. "Local scour associated with angled spur dikes." Journal of Hydraulic Engineering 128.12 (2002): 1087-1093.

Kwan, Tek Fei. "A study of abutment scour." (1988).

Lai, Yong G., et al. "Three-Dimensional Computational Modeling of Flows through an Engineered Log Jam." World Environmental and Water Resources Congress 2017, 2017, doi:10.1061/9780784480625.003.

Landers, Mark, and David Mueller. "Evaluation of Selected Pier-Scour Equations Using Field Data." *Transportation Research Record: Journal of the Transportation Research Board*, vol. 1523, 1996, pp. 186–195., doi:10.3141/1523-23.

Latterell, Joshua J. The natural history and dynamics of large wood in the Queets River, Washington. Diss. University of Washington, 2005.

Leu, Jan-Mou, et al. "Hydraulic Characteristics of Flow over a Highly Permeable Porous Structure." World Environmental and Water Resources Congress 2008, 2008, doi:10.1061/40976(316)211.

Lewis, Lisa. Soil Bioengineering: An alternative for Roadside Management: A Practical Guide. San Dimas Technology & Development Center, 2000.

Li, Chen, and Junke Guo. "CFD Study of Decay Function of Wall Shear Stress with Scour around Complex-Shape Bridge Pier." University of Nebraska - Lincoln, 2016.

Littell, Jeremy S., et al. "Forest Ecosystems, Disturbance, and Climatic Change in Washington State, USA." Climatic Change, vol. 102, no. 1-2, 2010, pp. 129–158., doi:10.1007/s10584-010-9858-x.

"Lower Germany Creek Fish Assessment and Restoration." Lower Germany Creek Fish Assessment and Restoration — Wild Fish Conservancy, Wild Fish Conservancy Northwest, 1 Sept. 2012, wildfishconservancy.org/projects/germany-creek.

Manners, R. B., et al. "Structure and Hydraulics of Natural Woody Debris Jams." Water Resources Research, vol. 43, no. 6, 2007, doi:10.1029/2006wr004910.

Mantz, Peter A. "Incipient transport of fine grains and flakes by fluids-extended shield diagram." Journal of the Hydraulics division 103.ASCE 12992 (1977).

McHenry, M., et al. "The physical and biological effects of engineered logjams (ELJs) in the Elwha River, Washington." Report to Salmon Recovery Funding Board and Interagency Committee for Outdoor Recreation, Port Angeles, WA (2007): 82.

McQuivey, Raul S. Summary of Turbulence Data from Rivers, Conveyance Channels, and Laboratory Flumes: Turbulence in Water. Vol. 802. US Government Printing Office, 1973.

Meffe, Gary K. "Effects of abiotic disturbance on coexistence of predator-prey fish species." Ecology 65.5 (1984): 1525-1534.

Melville, Bruce W. "Closure to "Local Scour at Bridge Abutments" by BW Melville (April, 1992, Vol. 118, No. 4)." Journal of Hydraulic Engineering 119.9 (1993): 1071-1073.

Melville, Bruce W., and Stephen E. Coleman. Bridge scour. Water Resources Publication, 2000.

Montgomery, D R, et al. "Stream-Bed Scour, Egg Burial Depths, and the Influence of Salmonid Spawning on Bed Surface Mobility and Embryo Survival." *Canadian Journal of Fisheries and Aquatic Sciences*, vol. 53, no. 5, 1996, pp. 1061–1070., doi:10.1139/f96-028.

Montgomery, David R., and Tim B. Abbe. "Influence of logjam-formed hard points on the formation of valley-bottom landforms in an old-growth forest valley, Queets River, Washington, USA." Quaternary Research 65.1 (2006): 147-155.

Mosher, M.M. and K. Lunnum. Trees of Washington. Washington State University Extension Bulletin EB0440, 2003.

Neill, C. R. "Note on initial movement of coarse uniform bed-material." Journal of Hydraulic Research 6.2 (1968): 173-176.

Nezu, Iehisa, and Hiroji Nakagawa. "Investigation on Three-Dimensional Turbulent Structure in Uniform Open-Channel and Closed Duct Flows." Doboku Gakkai Ronbunshu, no. 369, 1986, pp. 89–98., doi:10.2208/jscej.1986.369_89.

Nezu, Iehisa, and Michio Sanjou. "PIV and PTV Measurements in Hydro-Sciences with Focus on Turbulent Open-Channel Flows." Journal of Hydro-Environment Research, vol. 5, no. 4, 2011, pp. 215–230., doi:10.1016/j.jher.2011.05.004.

NHC. Hydrology Technical Memorandum for SR 20/Skagit River CED (MP 100.7), Northwest Hydraulic Consultants, Inc., October 12, 2010.

Oliveto, Giuseppe, and Willi H. Hager. "Temporal evolution of clear water pier and abutment scour." Journal of Hydraulic Engineering 128.9 (2002): 811-820.

Papanicolaou, A. N., and A. R. Maxwell. "Equilibrium geomorphological conditions for high gradient bed streams." Washington State Department of Transportation, Technical Report T9902-27, Olympia, WA (2000).

Papanicolaou, A. N., L. Kjos, and J. F. Fox. Investigation of flow and local scour characteristics around a partially submerged permeable WSDOT barb. Rep. WA-RD 581.1, Washington State Department of Transportation (TRAC), (2004).

Papanicolaou, A. N., et al. "Surface roughness effects in near-bed turbulence: Implications to sediment entrainment." Journal of Engineering Mechanics 127.3 (2001): 211-218.

Papanicolaou, A. N., et al. "Depositional Patterns in Steep Mountainous Streams under Low Relative Submergence (LRS) Regime." World Environmental and Water Resources Congress 2011: Bearing Knowledge for Sustainability. 2011.

Papanicolaou, A. N., et al. “Role of Structure Submergence on Scour Evolution in Gravel Bed Rivers: Application to Slope-Crested Structures.” Journal of Hydraulic Engineering, vol. 144, no. 2, 2017, doi:10.1061/(asce)hy.1943-7900.0001411.

Parker, Gary, et al. “Effect of Floodwater Extraction on Mountain Stream Morphology.” Journal of Hydraulic Engineering, vol. 129, no. 11, 2003, pp. 885–895., doi:10.1061/(asce)0733-9429(2003)129:11(885).

Parker, Gary, and Peter R. Wilcock. “Sediment Feed and Recirculating Flumes: Fundamental Difference.” Journal of Hydraulic Engineering, vol. 119, no. 11, 1993, pp. 1192–1204., doi:10.1061/(asce)0733-9429(1993)119:11(1192).

Pattison, M. J. “Friction Velocity.” A-To-Z Guide to Thermodynamics, Heat and Mass Transfer, and Fluids Engineering, 2 Feb. 2011, doi:10.1615/atoz.f.friction_velocity.

Prancevic, Jeff P., and Michael P. Lamb. “Particle Friction Angles in Steep Mountain Channels.” Journal of Geophysical Research: Earth Surface, vol. 120, no. 2, 2015, pp. 242–259., doi:10.1002/2014jf003286.

Raikar, Rajkumar V., and Subhasish Dey. "Clear-water scour at bridge piers in fine and medium gravel beds." Canadian Journal of Civil Engineering 32.4 (2005): 775-781.

Raudkivi, Arved J. “Functional Trends of Scour at Bridge Piers.” *Journal of Hydraulic Engineering*, vol. 112, no. 1, 1986, pp. 1–13., doi:10.1061/(asce)0733-9429(1986)112:1(1).

Raudkivi, Arved J., and Robert Ettema. "Clear-water scour at cylindrical piers." Journal of Hydraulic Engineering 109.3 (1983): 338-350.

Reyff, James A. “A Brief History of Underwater Construction Noise.” *The Journal of the Acoustical Society of America*, vol. 141, no. 5, June 2017, pp. 3846–3846., doi:10.1121/1.4988574.

Rice, C. E., K. C. Kadavy, and K. M. Robinson. "Roughness of loose rock riprap on steep slopes." Journal of Hydraulic Engineering 124.2 (1998): 179-185.

Robinson, L. The lowdown on riprap: option for preventing erosion in channels and streambanks. In Erosion Control. Forester Communications, Inc. Santa Barbara, CA, 2002.

Rosgen, David L. "The cross-vane, w-weir and j-hook vane structures... their description, design and application for stream stabilization and river restoration." Wetlands engineering & river restoration 2001. 2001. 1-22.

Rouse, Hunter. "An analysis of sediment transportation in the light of fluid turbulence." (1939).

Schultz, R. C., Collettil, J. P., Isenhart, T. M., Simpkins, W. W., Mize, C. W., and Thompson, M. L. “Design and placement of a multi-species riparian buffer strip system”. Agroforestry Systems, 29(3), (1995):201-226.

Shields, Albert. "Application of similarity principles and turbulence research to bed-load movement." CalTech library (1936).

Shields Jr, F. Douglas, and Christopher J. Gippel. "Prediction of effects of woody debris removal on flow resistance." Journal of Hydraulic Engineering 121.4 (1995): 341-354.

Shields Jr, F. Douglas, C. M. Cooper, and S. Testa. "Towards greener riprap: environmental considerations from microscale to macroscale." River, coastal and shoreline protection: Erosion control using riprap and armourstone (1995): 557-574.

Shields, Jr. F. Douglas, et al. “Effect of Large Woody Debris Structures on Stream Hydraulics.” Wetlands Engineering and River Restoration 2001, 2001, doi:10.1061/40581(2001)76.

Smith, M. E. “Noise-Induced Stress Response and Hearing Loss in Goldfish (Carassius Auratus).” Journal of Experimental Biology, vol. 207, no. 3, Jan. 2004, pp. 427–435., doi:10.1242/jeb.00755.

Sommerfeld, Arnold. "Ein beitrag zur hydrodynamischen erklaerung der turbulenten fluessigkeitsbewegungen." Atti del 4 (1908): 116-124.

Song, T., W. H. Graf, and U. Lemmin. "Uniform flow in open channels with movable gravel bed." Journal of Hydraulic Research 32.6 (1994): 861-876.

SonTek. “Acoustial Doppler VelocimeterR (ADV): Sampling Volume Size and Velocity Accuracy.” SonTek Technical Notes, 1998.

Streeter, V. L., and E. B. Wylie. "Fluid Mechanics, 562 pp." (1979).

Sturm, Terry W. Open Channel Hydraulics. McGraw-Hill, (2010).

Suaznabar, Oscar, Li Chen, and Kornel Kerenyi. "Feather River Bridge Pier Scour Study." (2014).

Svensson, A. "Estimation of Hydraulic Conductivity from Grain Size Analyses." Chalmers University of Technology: Gothenburg, Sweden (2014).

Svoboda, C. D., and K. Russell. "Flume analysis of engineered large wood structures for scour development and habitat." World Environmental and Water Resources Congress 2011: Bearing Knowledge for Sustainability. 2011.

Thompson, Douglas M. "Long-term effect of instream habitat-improvement structures on channel morphology along the Blackledge and Salmon rivers, Connecticut, USA." Environmental Management 29.2 (2002): 250-265.

U.S. Department of Agriculture, Natural Resources Conservation Service. Fish Passage and Screening Design. National Engineering Handbook, part 654, Stream Restoration Design, Technical Supplement 14N. Washington, DC, (2007a).

U.S. Department of Agriculture, Natural Resources Conservation Service. Project Implementation. National Engineering Handbook, part 654, Stream Restoration Design, Chapter 15. Washington, DC, (2007b).

Vanoni, Vito A., and Norman H. Brooks. "Laboratory studies of the roughness and suspended load of alluvial streams." (1957).

Vanoni, V. A., et al. "Sediment transportation mechanics: Initiation of motion." J. Hydraul. Div. Am. Soc. Civ. Eng 92.2 (1966): 291-314.

Wallerstein, Nicholas P., et al. “Distorted Froude-Scaled Flume Analysis of Large Woody Debris.” Earth Surface Processes and Landforms, vol. 26, no. 12, 2001, pp. 1265–1283., doi:10.1002/esp.271.

Wallerstein, N. P. “Dynamic Model for Constriction Scour Caused by Large Woody Debris.” Earth Surface Processes and Landforms, vol. 28, no. 1, 2003, pp. 49–68., doi:10.1002/esp.426.

Ward, Carl. "Engineered logjams: an alternative bank-protection method for US 101 along the Hoh River, Washington." Road Ecology Center (2006).

Washington State Recreation and Conservation Office. “Elwha River Engineered Log Jams.” HWS, North Olympic Peninsula LE for Salmon, 31 May 2000, hws.ekosystem.us/project/180/10995.

Washington State Recreation and Conservation Office. “South Fork Nooksack (Mouth to Skookum Cr.) Restoration.” HWS, WRIA 1 Salmon Recovery Board (LE), 1 July 2011, hws.ekosystem.us/project/360/7004.

White, F. M. "Fluid mechanics MaGraw-Hill." New York (1994).

Whitehouse, R. J. S. "Scour at marine structures: a manual for engineers and scientists." Res. Rep. SR417, HR Wallingford Limited, Wallingford, UK, 216p (1997).

Wolman, M. Gordon. "A method of sampling coarse river-bed material." EOS, Transactions American Geophysical Union 35.6 (1954): 951-956.

WSDOT. (*Roadside Manual. Publication M25-30*. Washington State Department of Transportation, 2003.

WSDOT. *Standard Specifications for Roads, Bridge, and Municipal Construction.Publication M41-10.* Washington State Department of Transportation, 2010a.

WSDOT. *Design Manual. Publication M22-01.07*. Washington State Department of Transportation, 2010b.

WSDOT. *Hydraulics Manual. Publication M23-03.03*. Washington State Department of Transportation, 2010c.

WSDOT. *Biological Assessment State Route 20: Milepost 100 to 101 Skagit River Chronis Environmental Deficiency-Permanent Restoration,* Northwest Region Environmental Services Biology Program, Washington State Department of Transportation, January 2011.

Yalin, Mehmet Selim, and Emin Karahan. "Inception of sediment transport." Journal of the hydraulics division 105.11 (1979): 1433-1443.

Zeller, J. Introduction into the sediment transport of open channels (Reprint). Switzerland. Bauzeitung, 81. (1963): 3-19.

Appendices

Appendix A: Prototype dolotimber ELJ details

Table A.1. Prototype ELJ1 layering detail.

ELJ 1				
Layer 1				
Dolo Type	**Count**	**Dolo (Y/N)**	**Log**	
			Type	**Count**
A	1	Y	c	3
B	29	Y	c	2
P	0	Ballasted Bundle		
Q	0	Y	e	1
Layer 2				
Dolo Type	**Count**	**Dolo (Y/N)**	**Log**	
			Type	**Count**
B	18	Y	c	3
O	1	Y	d	2
P	7	Ballasted Bundle		
L	0	N	Racking Logs	
Q	6	Y	e	1
Layer 3				
Dolo Type	**Count**	**Dolo (Y/N)**	**Log**	
			Type	**Count**
E	0	Y	h	1
			d	2
J	1	Y	f	1
L	5	N	Racking Logs	
M	0	N	j	11
S	11	Y	e	1
V	5	Ballasted Bundle		

Table A.2. Prototype ELJ2 layering detail.

ELJ 2				
Layer 1				
Dolo Type	**Count**	**Dolo (Y/N)**	**Log**	
			Type	**Count**
A	3	Y	c	3
B	48	Y	c	2
Layer 2				
Dolo Type	**Count**	**Dolo (Y/N)**	**Log**	
			Type	**Count**
B	24	Y	c	3
O	8	Y	d	2
P	5	Ballasted Bundle		
E	4	Y	h	1
			d	2
Q	5	Y	e	1
Layer 3				
Dolo Type	**Count**	**Dolo (Y/N)**	**Log**	
			Type	**Count**
E	5	Y	h	1
			d	2
J	0	Y	f	1
L	7	N	Racking Logs	
M	0	N	j	11
S	17	Y	e	1
V	4	Ballasted Bundle		

Table A.3. Prototype Revetment 1 layering detail.

Revetment 1				
Layer 1				
Dolo Type	**Count**	**Dolo (Y/N)**	**Log**	
			Type	**Count**
A	3	Y	c	3
B	48	Y	c	2
D	42	Y	m	3
Layer 2				
Dolo Type	**Count**	**Dolo (Y/N)**	**Log**	
			Type	**Count**
B	21	Y	c	3
O	16	Y	d	2
C	21	Y	a	1
			i	1
E	21	Y	h	1
			d	2
K	16	N	f	3
M	5	N	n	4
			o	4
			p	3
Layer 3				
Dolo Type	**Count**	**Dolo (Y/N)**	**Log**	
			Type	**Count**
E	0	Y	h	1
			d	2
A	21	Y	c	3
H	21	Y	g	1
Y	0	N	j	11
S	0	Y	e	1
V	0	Ballasted Bundle		

Table A.4. Prototype Revetment 2 layering detail.

Revetment 2				
Layer 1				
Dolo Type	**Count**	**Dolo (Y/N)**	**Log**	
			Type	**Count**
A	21	Y	c	3
B	29	Y	c	2
D	34	Y	m	3
Layer 2				
Dolo Type	**Count**	**Dolo (Y/N)**	**Log**	
			Type	**Count**
H	1	Y	g	1
O	20	Y	d	2
T	10	Ballasted Bundle		
G	13	Y	a	1
			b	1
E	24	Y	h	1
			d	2
K	8	N	18" DIA	3
F	9	Y	b	2
Layer 3				
Dolo Type	**Count**	**Dolo (Y/N)**	**Log**	
			Type	**Count**
E	0	Y	h	1
			d	2
A	0	Y	c	3
H	0	Y	g	1
Y	0	N	j	11
S	0	Y	e	1
V	0	Ballasted Bundle		

Table A.5 Prototype Revetment 3 layering detail.

Revetment 3				
Layer 1				
Dolo Type	**Count**	**Dolo (Y/N)**	**Log**	**Count**
			Type	3
A	21	Y	c	2
B	41	Y	c	3
D	36	Y	m	
Layer 2				
Dolo Type	**Count**	**Dolo (Y/N)**	**Log**	
			Type	**Count**
H	27	Y	g	1
O	11	Y	d	2
T	8	Ballasted Bundle		
G	18	Y	a	1
			b	1
E	11	Y	h	1
			d	2
K	6	N	18" DIA	3
F	15	Y	b	2
A	3	Y	c	3
B	11	Y	c	2
L	3	N	Racking Logs	
M	4	N	n	4
			o	4
			p	3
Layer 3				
Dolo Type	**Count**	**Dolo (Y/N)**	**Log**	
			Type	**Count**
E	1	Y	h	1
			d	2
A	4	Y	c	3
D	1	Y	m	3
O	1	Y	d	2
S	0	Y	e	1
V	0	Ballasted Bundle		

Table A.6. Prototype Revetment 1 component breakdown and porosity.

Prototype Revetment 1			
Component	**Volume (ft^3)**	**Percent Structure Volume (%)**	
Cobble	0.0	0.0	
Logs	17782.2	46.2	
Dolos	20733.6	53.8	
Total Solids	38515.8	**Porosity**	78.6
Total Volume	180000.0		

Table A.7. Prototype Revetment 2 component breakdown and porosity.

Prototype Revetment 2			
Component	**Volume (ft^3)**	**Percent Structure Volume (%)**	
Cobble	314.2	1.1	
Logs	12426.6	45.4	
Dolos	14629.7	53.5	
Total Solids	27370.5	**Porosity**	76.8
Total Volume	117876.0		

Table A.8. Prototype Revetment 3 component breakdown and porosity.

Prototype Revetment 3			
Component	**Volume (ft^3)**	**Percent Structure Volume (%)**	
Cobble	251.3	0.7	
Logs	15738.4	44.4	
Dolos	19474.0	54.9	
Total Solids	35463.7	**Porosity**	80.8
Total Volume	185115.0		

Table A.9. Prototype ELJ1 component breakdown and porosity.

ELJ 1 Prototype			
Component	**Volume (ft^3)**	**Percent Structure Volume (%)**	
Cobble	785.4	8.2	
Logs	2271.8	23.8	
Dolos	6491.3	68.0	
Total Solids	9548.6	**Porosity**	78.6
Total Volume	44640.0		

Table A.10. Prototype ELJ2 component breakdown and porosity.

ELJ 2 Prototype			
Component	**Volume (ft^3)**	**Percent Structure Volume (%)**	
Cobble	571.8	3.4	
Logs	5228.4	31.0	
Dolos	11045.0	65.6	
Total Solids	16845.1	**Porosity**	77.2
Total Volume	73944.0		

Appendix B: Model dolotimber ELJ details

Table B.1. Calculations of structure component percentage between prototype and model for ELJ1.

ELJ 1 Prototype			
Component	**Volume (ft^3)**	**Percent Structure Volume (%)**	
Cobble	785.4	8.2	
Logs	2271.8	23.8	
Dolos	6491.3	68.0	
Total Solids	9548.6	**Porosity**	78.6
Total Volume	44640.0		
ELJ 1 Model			
Component	**Voume (in^3)**	**Percent Structure Volume (%)**	
Logs	3.7	28.5	
Dolos	9.2	71.5	
Total Solids	12.8	**Porosity**	78.4
Total Volume	59.5		

Table B.2. Calculation of structure component percentage between prototype and model for ELJ2.

ELJ 2 Prototype			
Component	**Volume (ft^3)**	**Percent Structure Volume (%)**	
Cobble	571.8	3.4	
Logs	5228.4	31.0	
Dolos	11045.0	65.6	
Total Solids	16845.1	**Porosity**	77.2
Total Volume	73944.0		
ELJ 2 Model			
Component	**Volume (in^3)**	**Percent Structure Volume (%)**	
Logs	7.3	32.5	
Dolos	15.2	67.5	
Total Solids	22.5	**Porosity**	77.2

Table B.3. Calculation of model revetment porosity with proxy gravel.

Symbol	Parameter	Location		
		Revetment 1	**Revetment 2**	**Revetment 3**
n	Porosity [-]	0.785	0.765	0.807
d_{eff}	effective diameter (mm)	25	25	25
	effective diameter (m)	0.025	0.025	0.025
C_{SH}	shape factor [-]	9.5	9.5	9.5
τ	tortuosity {-}	2.5	2.5	2.5
C_{PK}	packing factor [-]	78.125	78.125	78.125
k	permeability (m^2)	9.28E-07	7.19E-07	1.25E-06
K	hydraulic conductivity (m/s)	9.08E+00	7.04E+00	1.22E+01

Appendix C: Equilibrium clearwater scour results

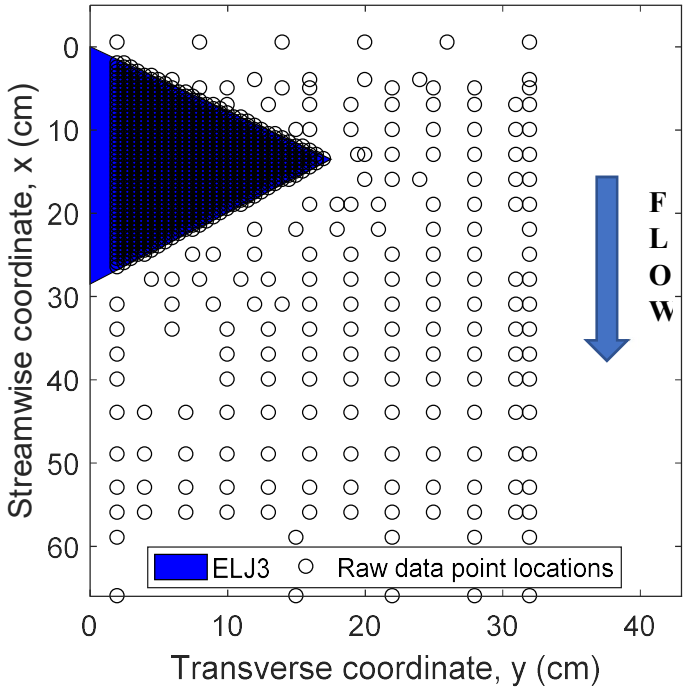

Figure C.1. Location of point gauge measurements in scour test section used in volume calculations.

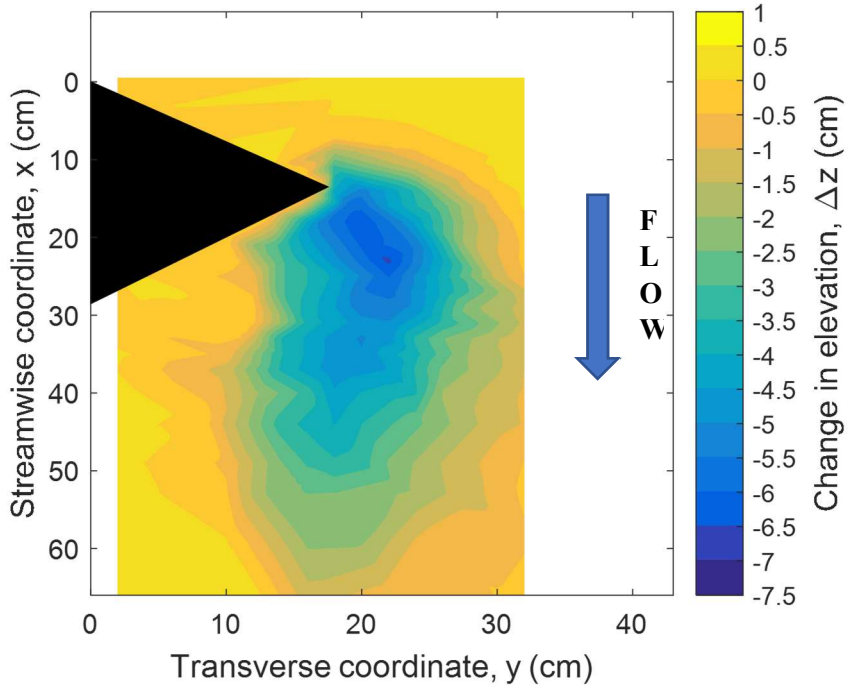

Figure C.2. Scour contour plots of Trials 1 in ELJ test section.

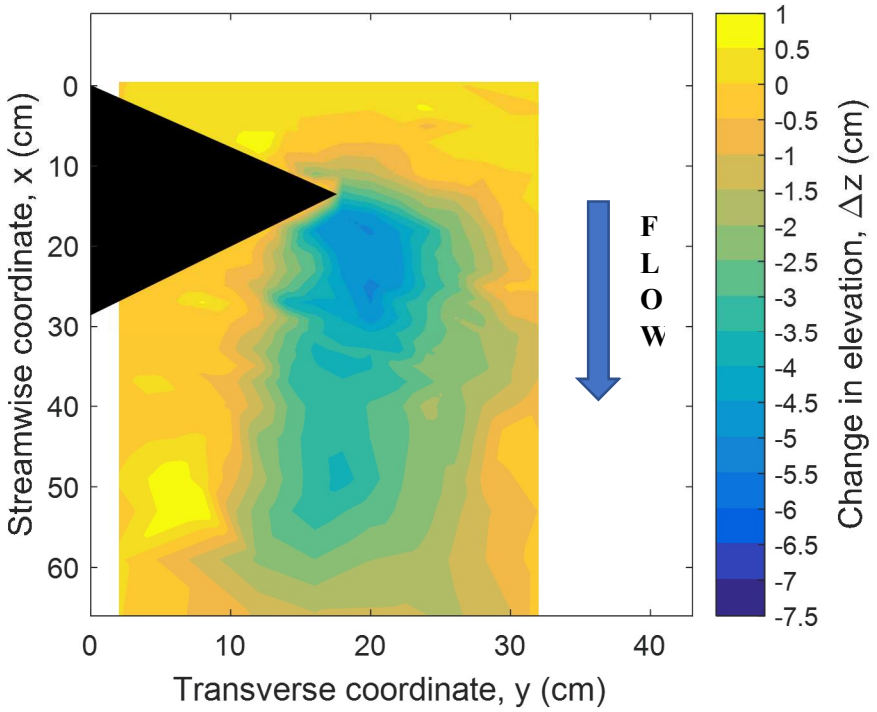

Figure C.3. Scour contour plots of Trial 2 in ELJ test section.

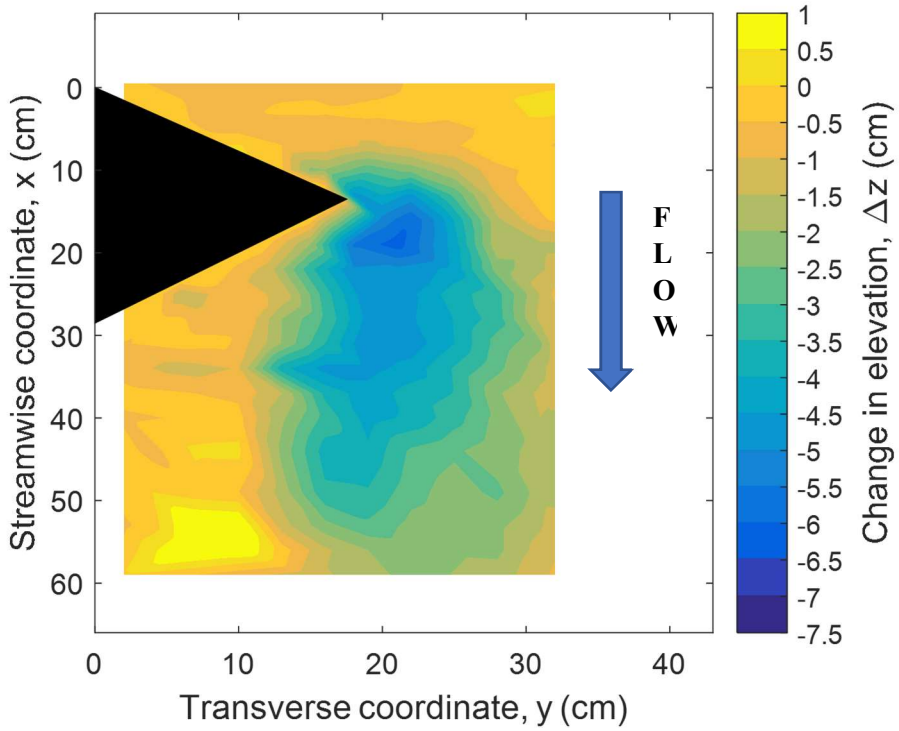

Figure C.4. Scour contour plots of Trial 3 in ELJ test section.

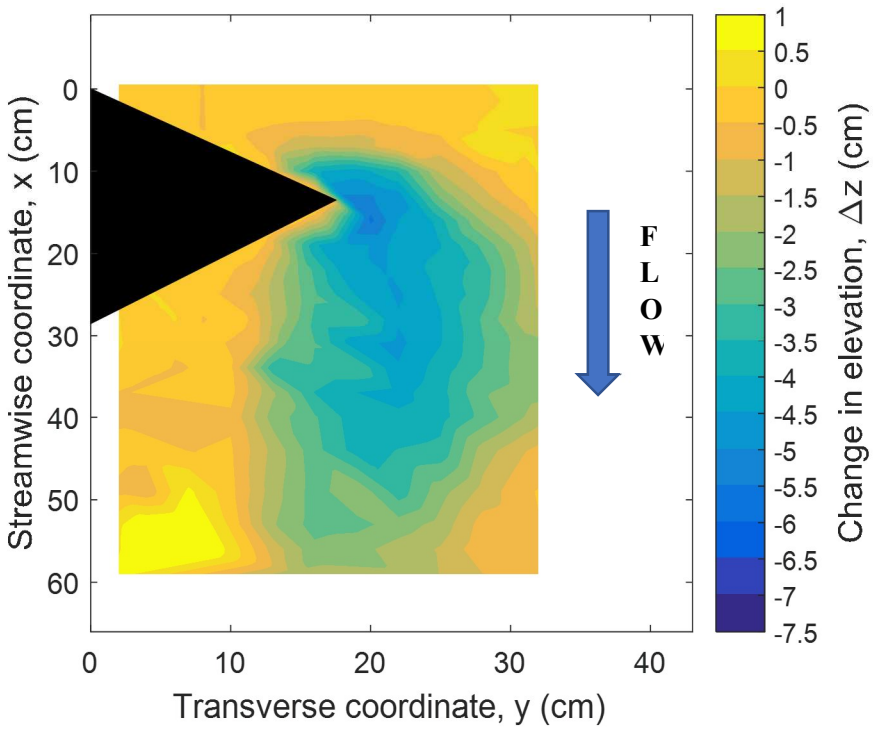

Figure C.5. Scour contour plots of Trials 4 in ELJ test section.

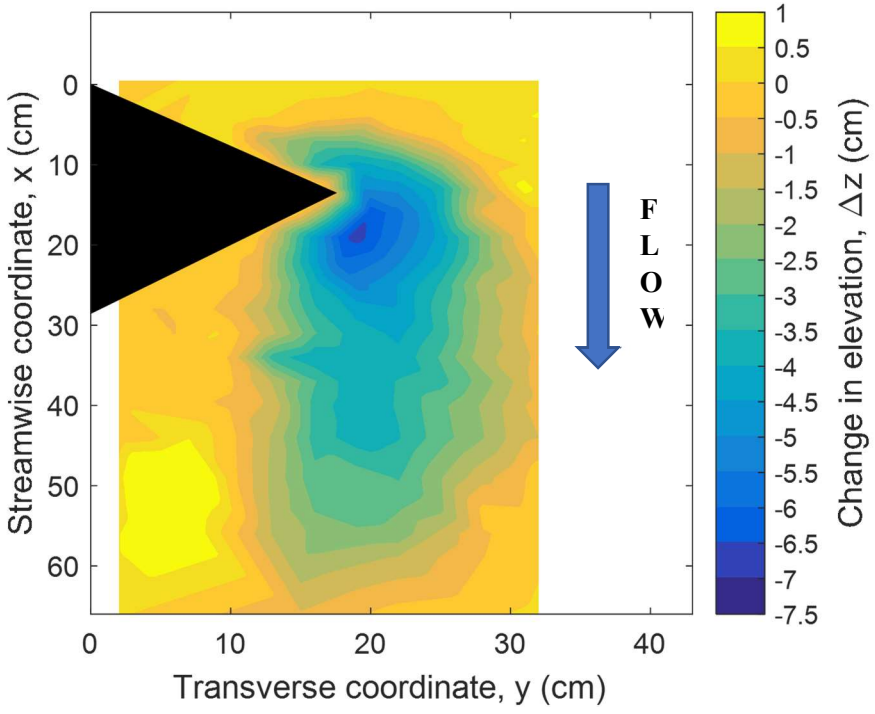

Figure C.6. Scour contour plots of Trial 5 in ELJ test section.

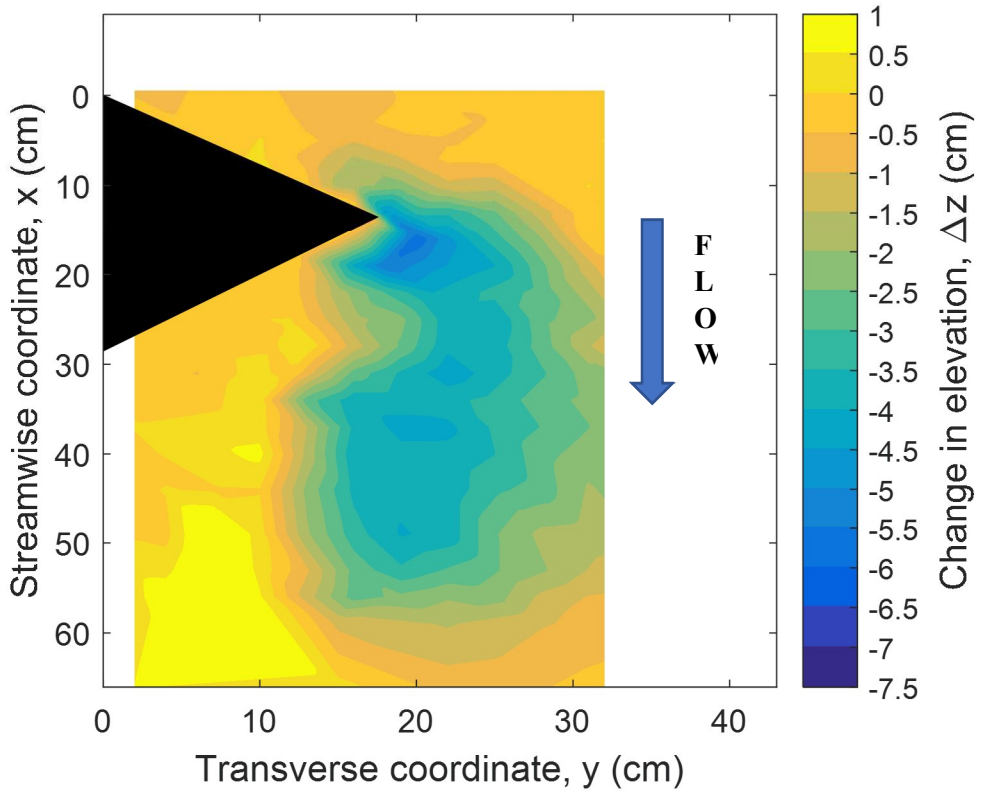

Figure C.7. Scour contour plot of sonar trial in ELJ test section.

Table C.1. Summary table of scour equilibrium conditions for sonar trial.

Trial #	Flow discharge, Q (m^3/s)	Approach flow depth, H (m)	Approach flow dimensionless shear stress, τ^* (-)	Maximum Scour Depth (cm)	Scour Hole Length (cm)	Scour Hole Volume (cm^3)
Sonar	0.0205	0.083	0.0352	6.0	65.4	2823.9

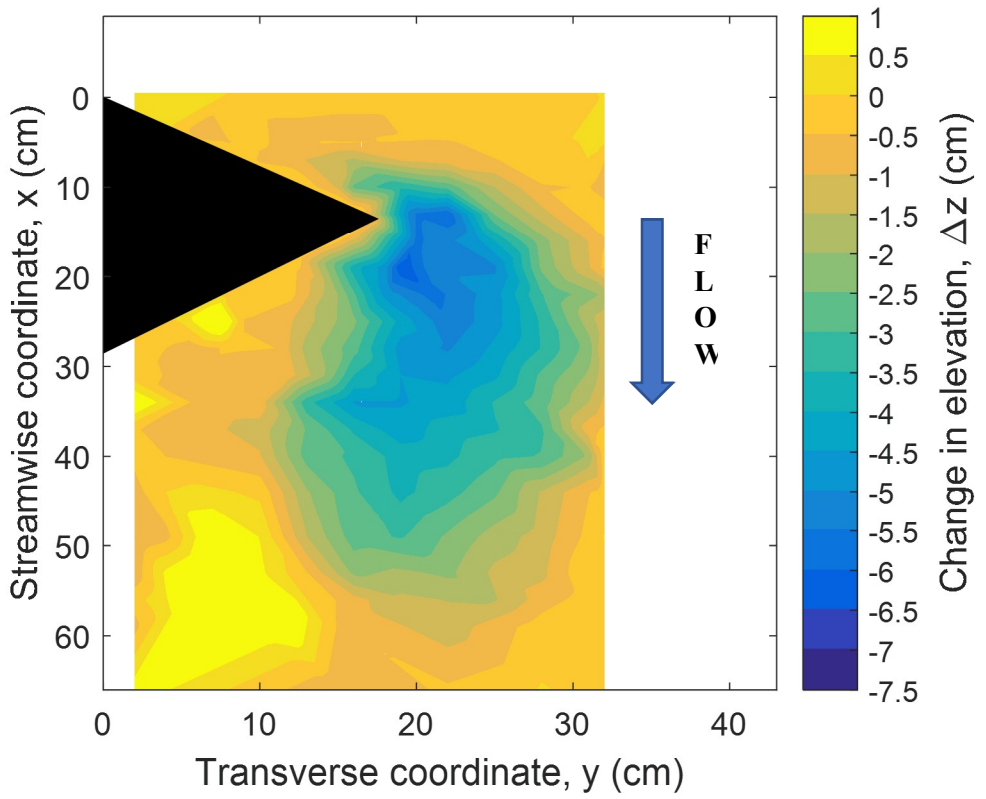

Figure C.8. Scour contour plot of IR trial in ELJ test section.

Table C.2. Summary table of scour equilibrium conditions for infrared trial.

Trial #	Flow discharge, Q (m^3/s)	Approach flow depth, H (m)	Approach flow dimensionless shear stress, τ^* (-)	Maximum Scour Depth (cm)	Scour Hole Length (cm)	Scour Hole Volume (cm^3)
Infrared	0.0205	0.082	0.0352	6.5	61.2	2830.7

Appendix D: Complete LSIV results

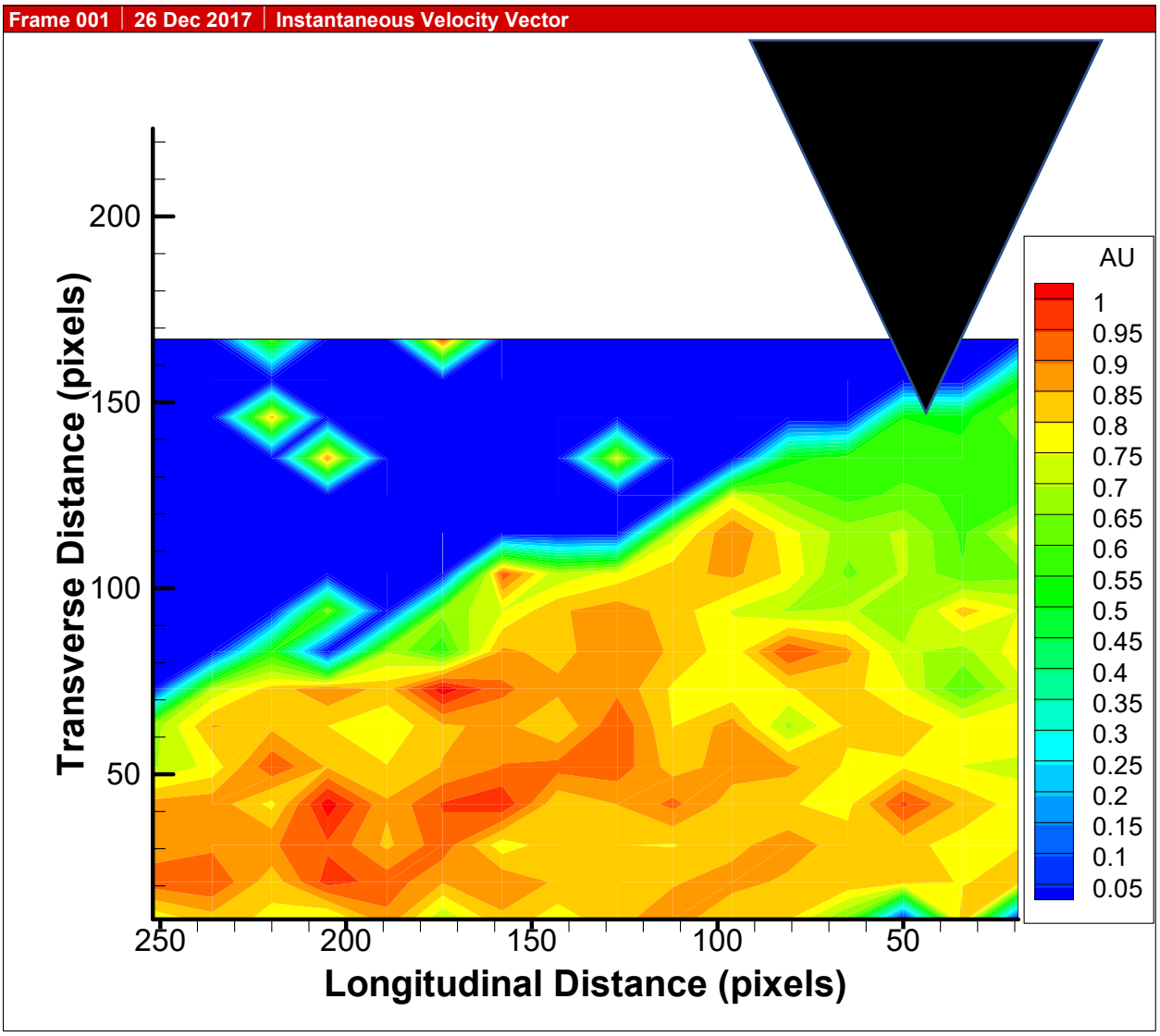

Figure D.1. LSIV results at 2.5 minutes elapsed.

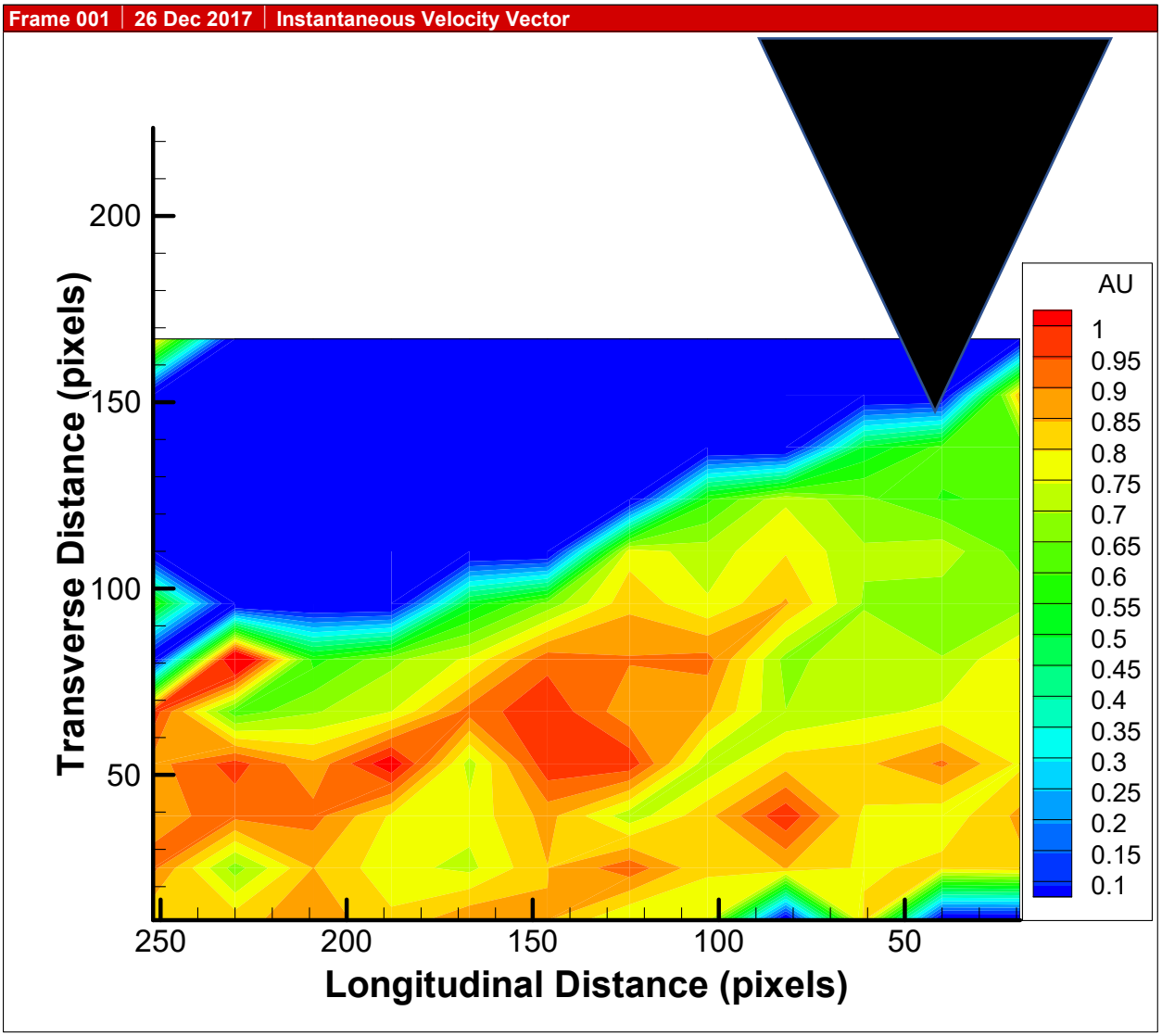

Figure D.2. LSIV results at 6.25 minutes elapsed.

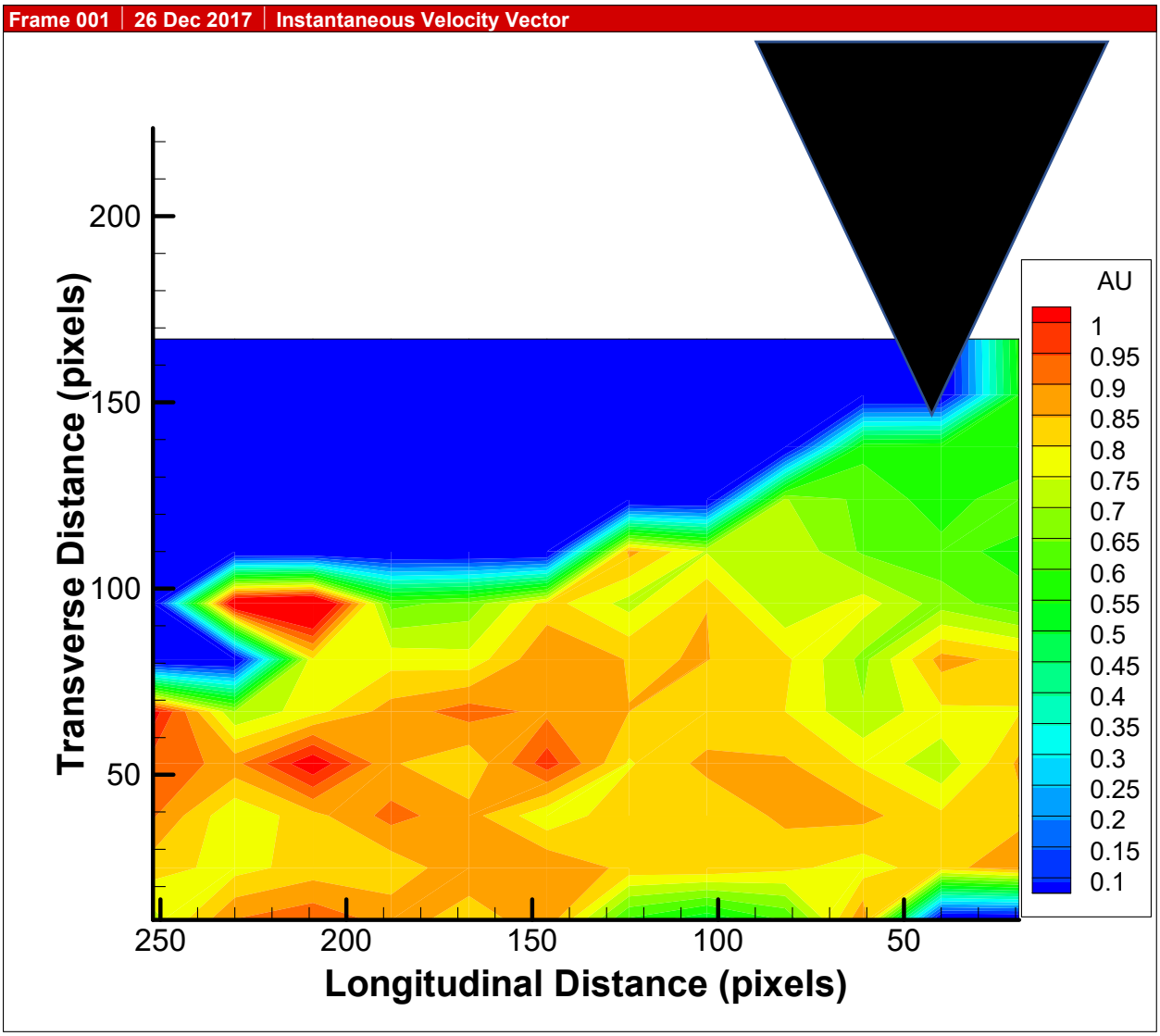

Figure D.3. LSIV results at 9.75 minutes elapsed.

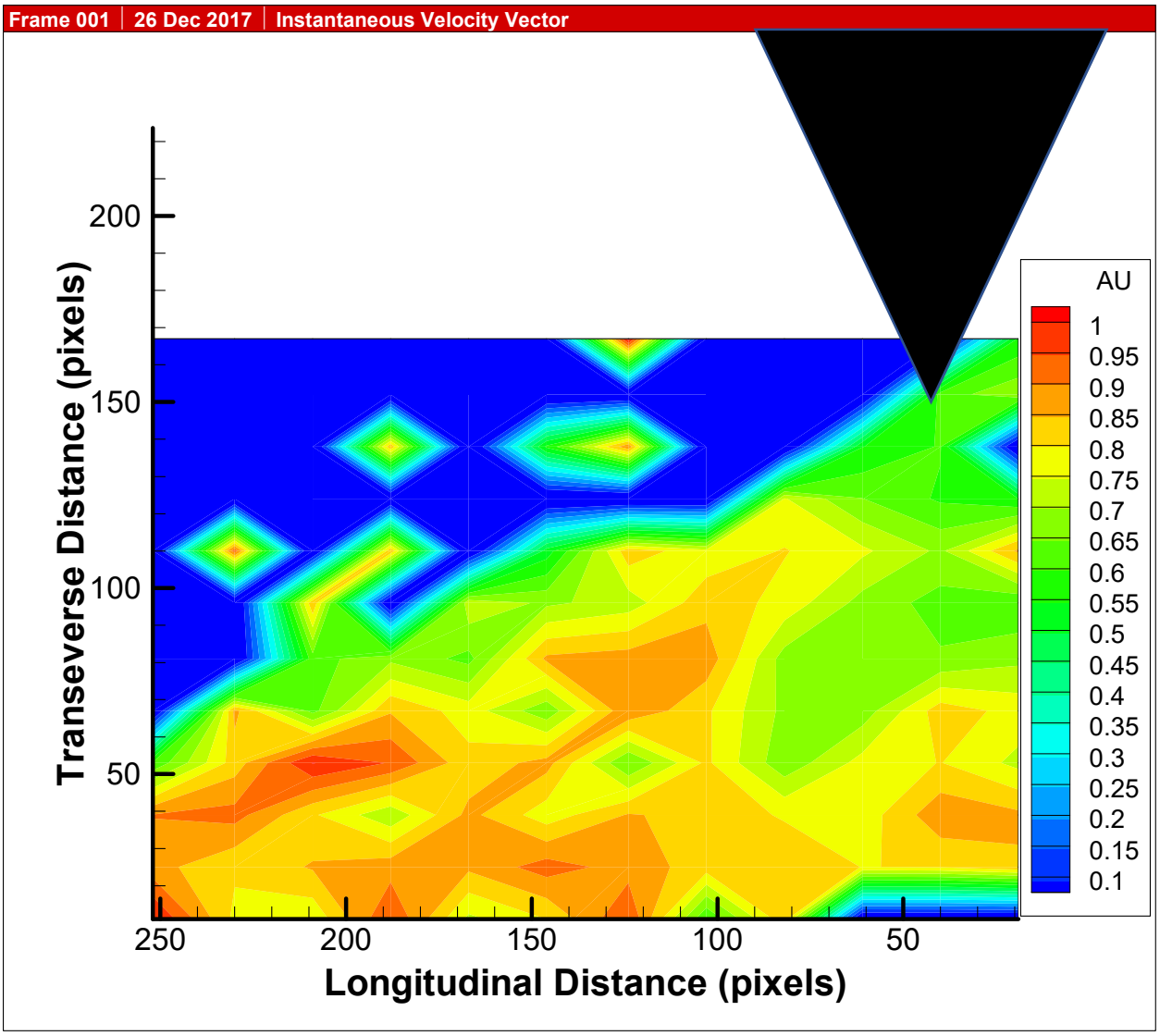

Figure D.4. LSIV results at 13.5 minutes elapsed.

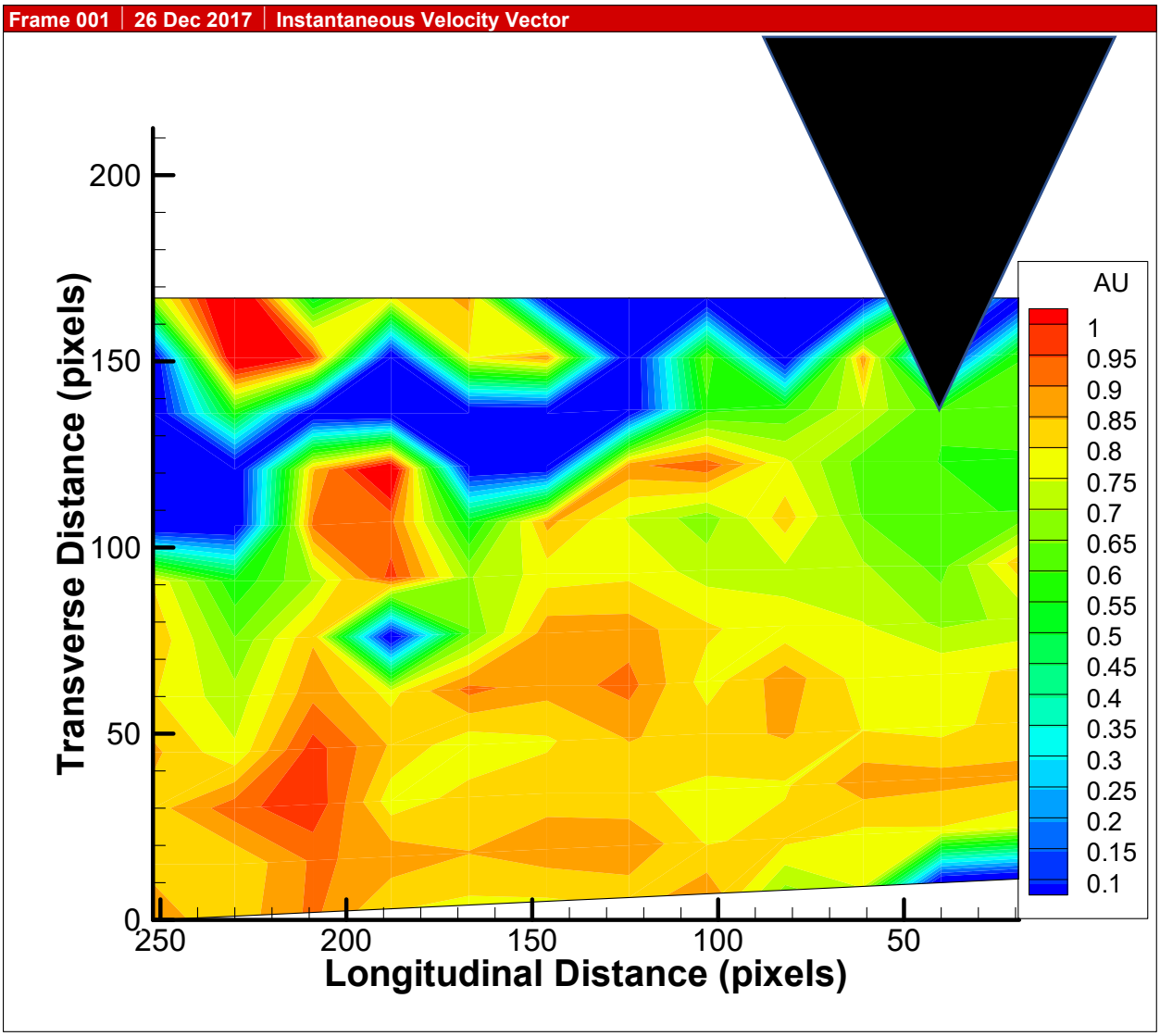

Figure D.5. LSIV results at 17 minutes elapsed.

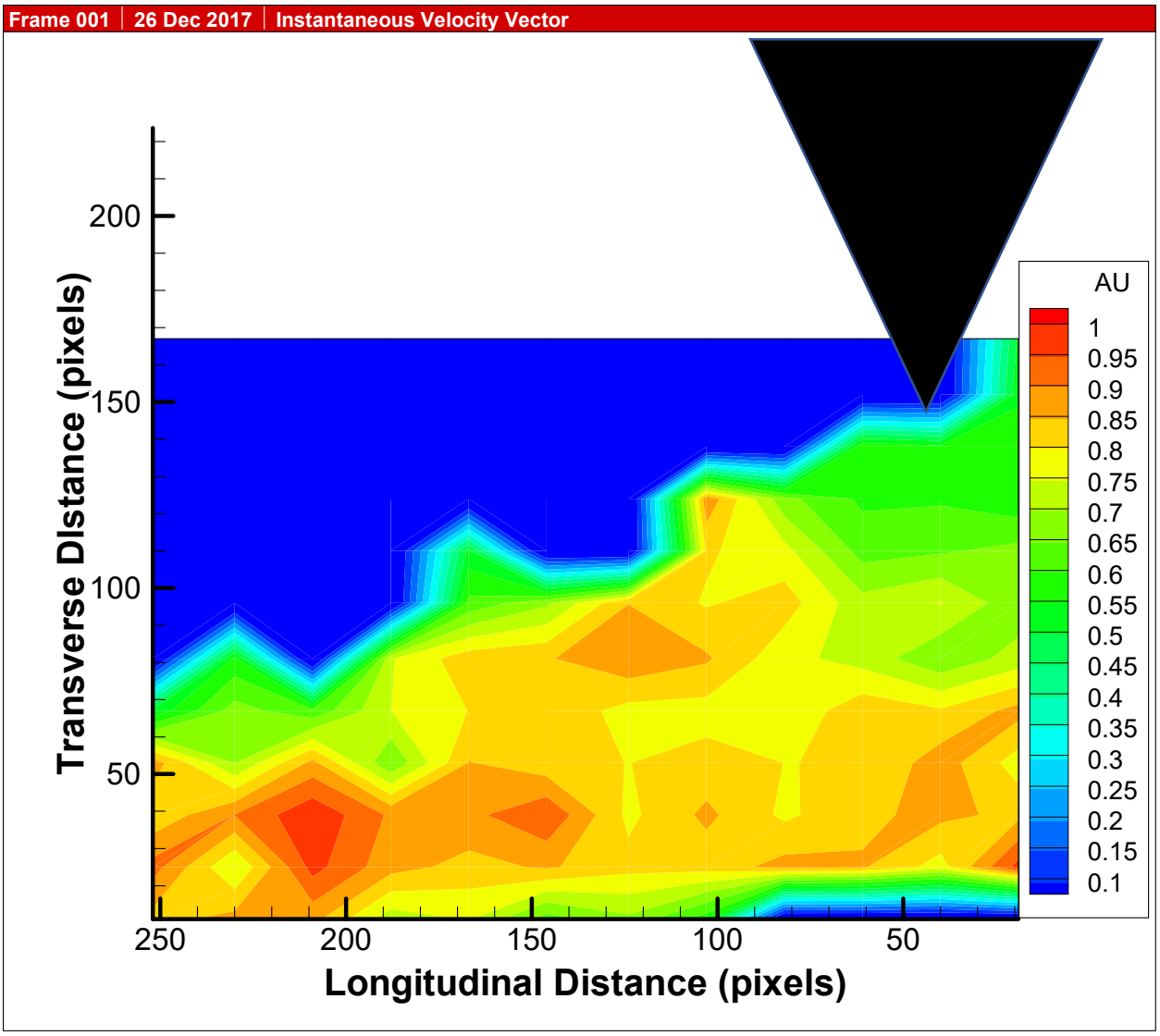

Figure D.6. LSIV results at 21.25 minutes elapsed.

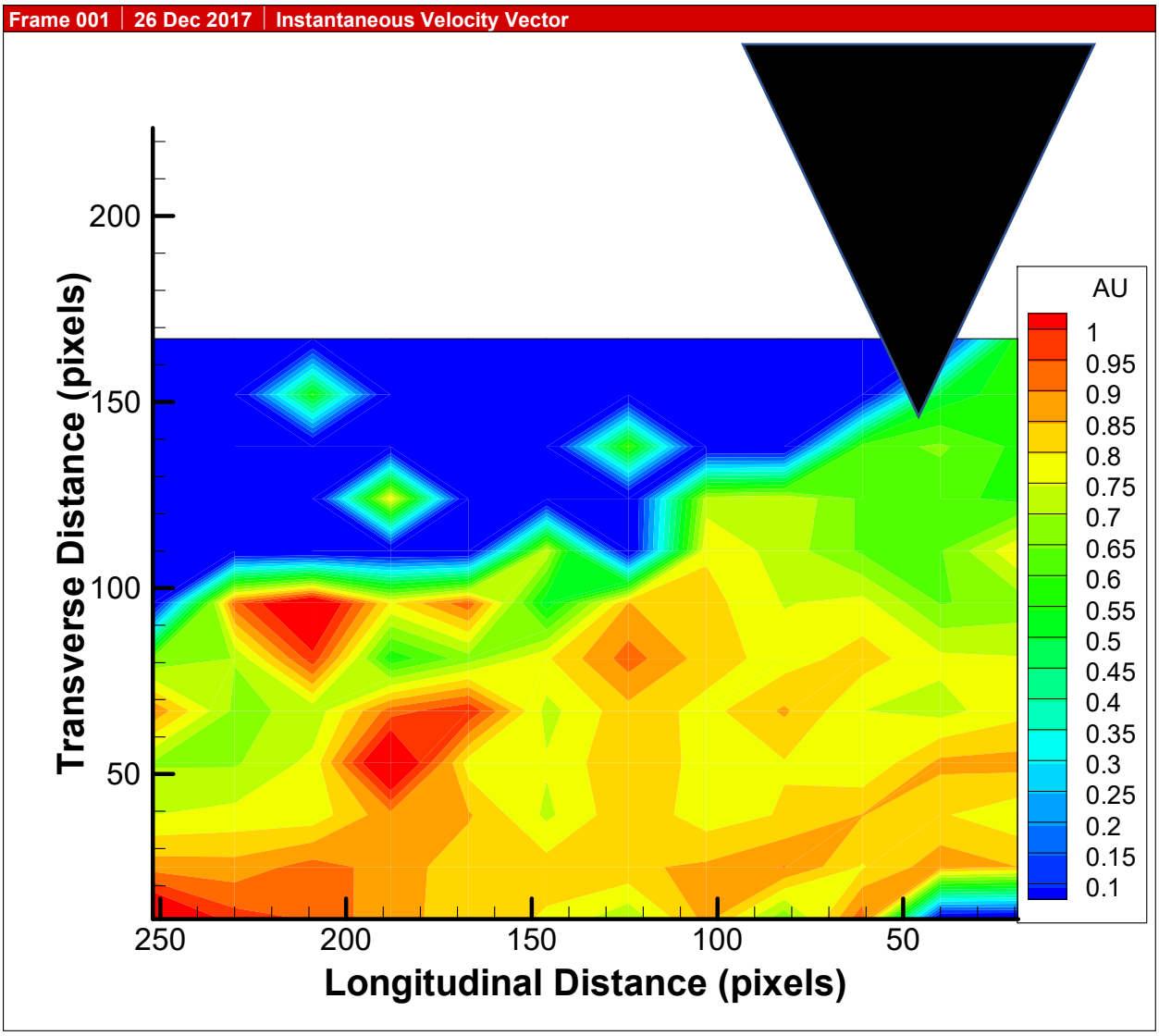

Figure D.7. LSIV results at 25.5 minutes elapsed.

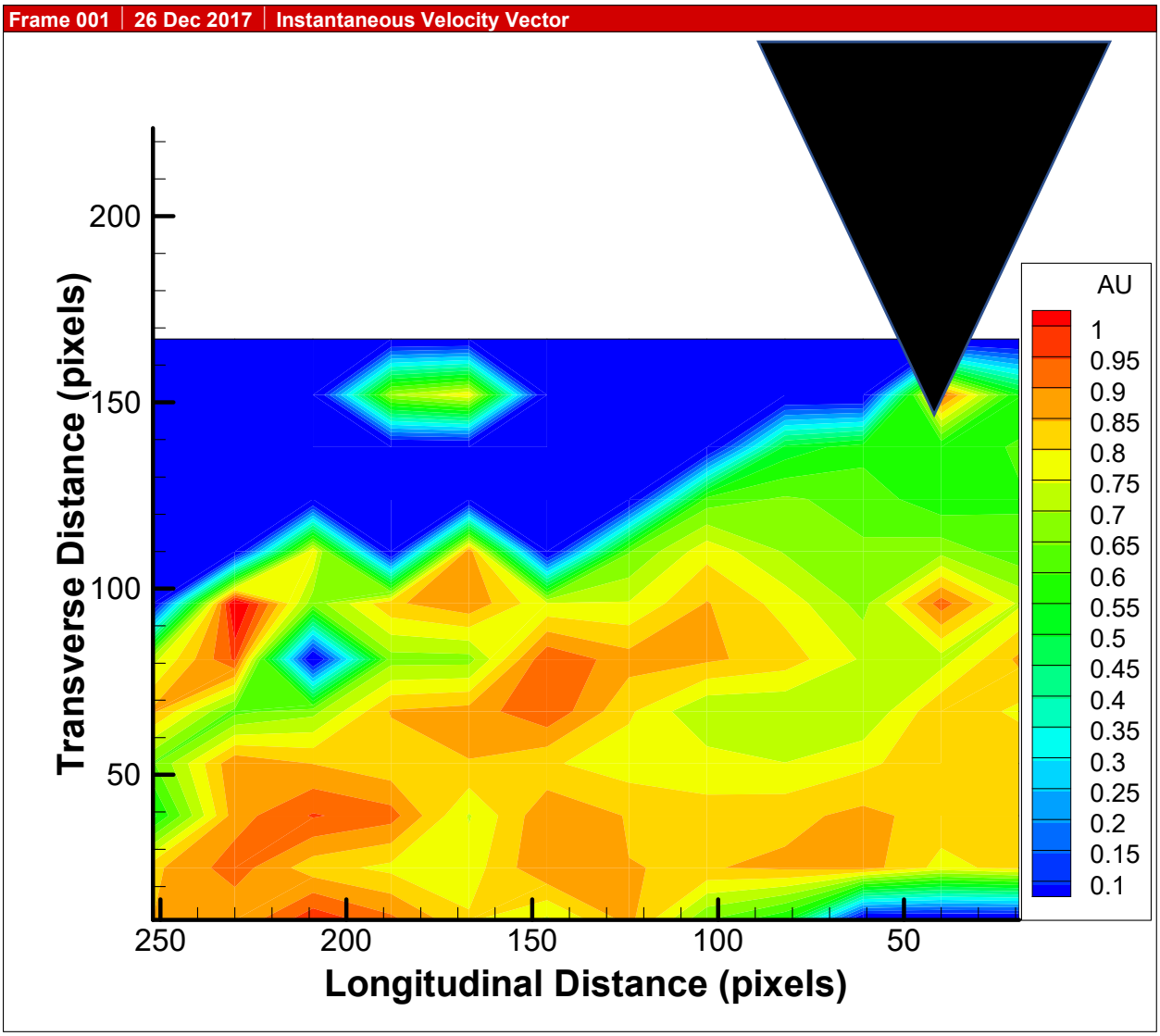

Figure D.8. LSIV results at 30 minutes elapsed

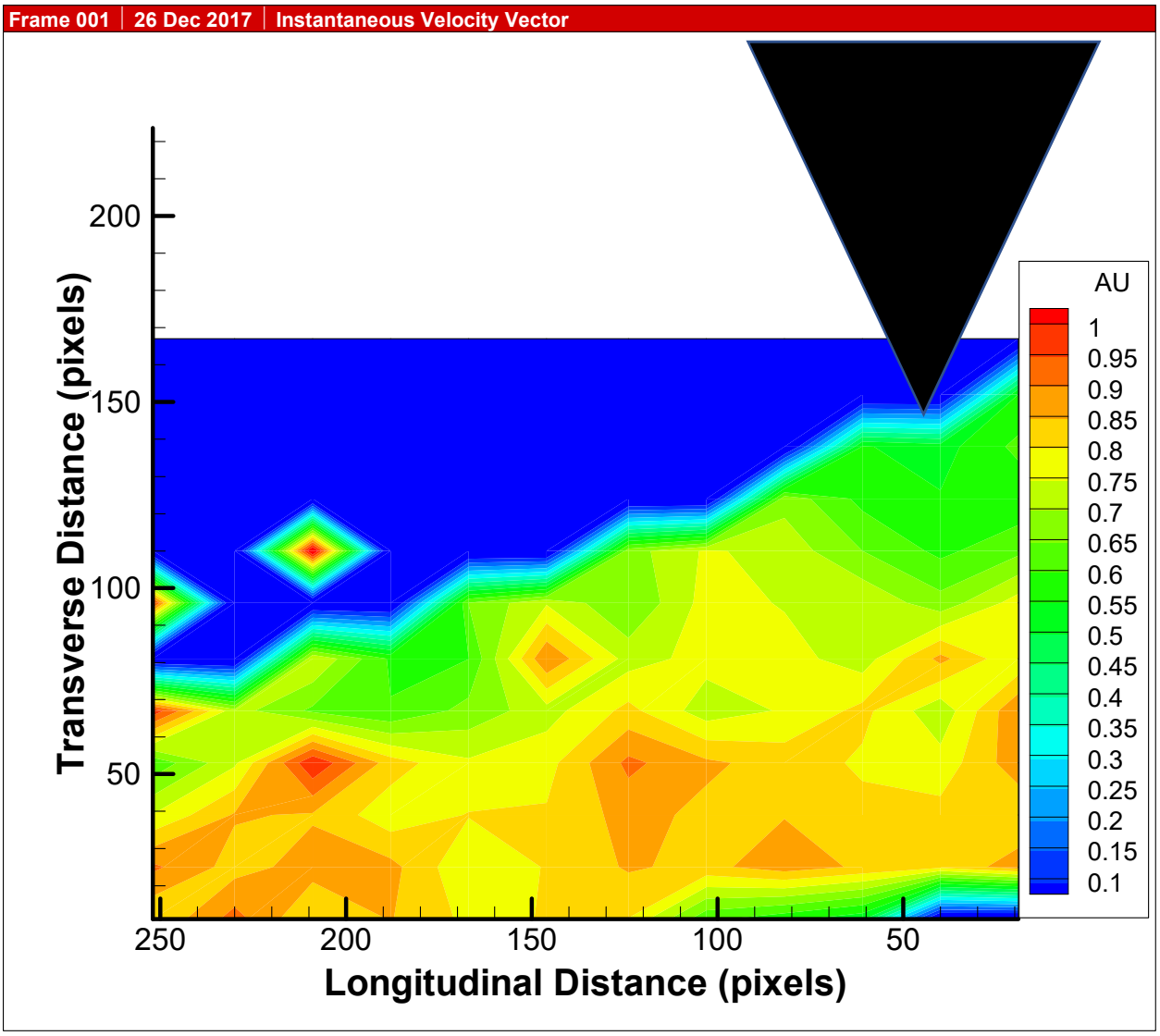

Figure D.9. LSIV results at 35 minutes elapsed

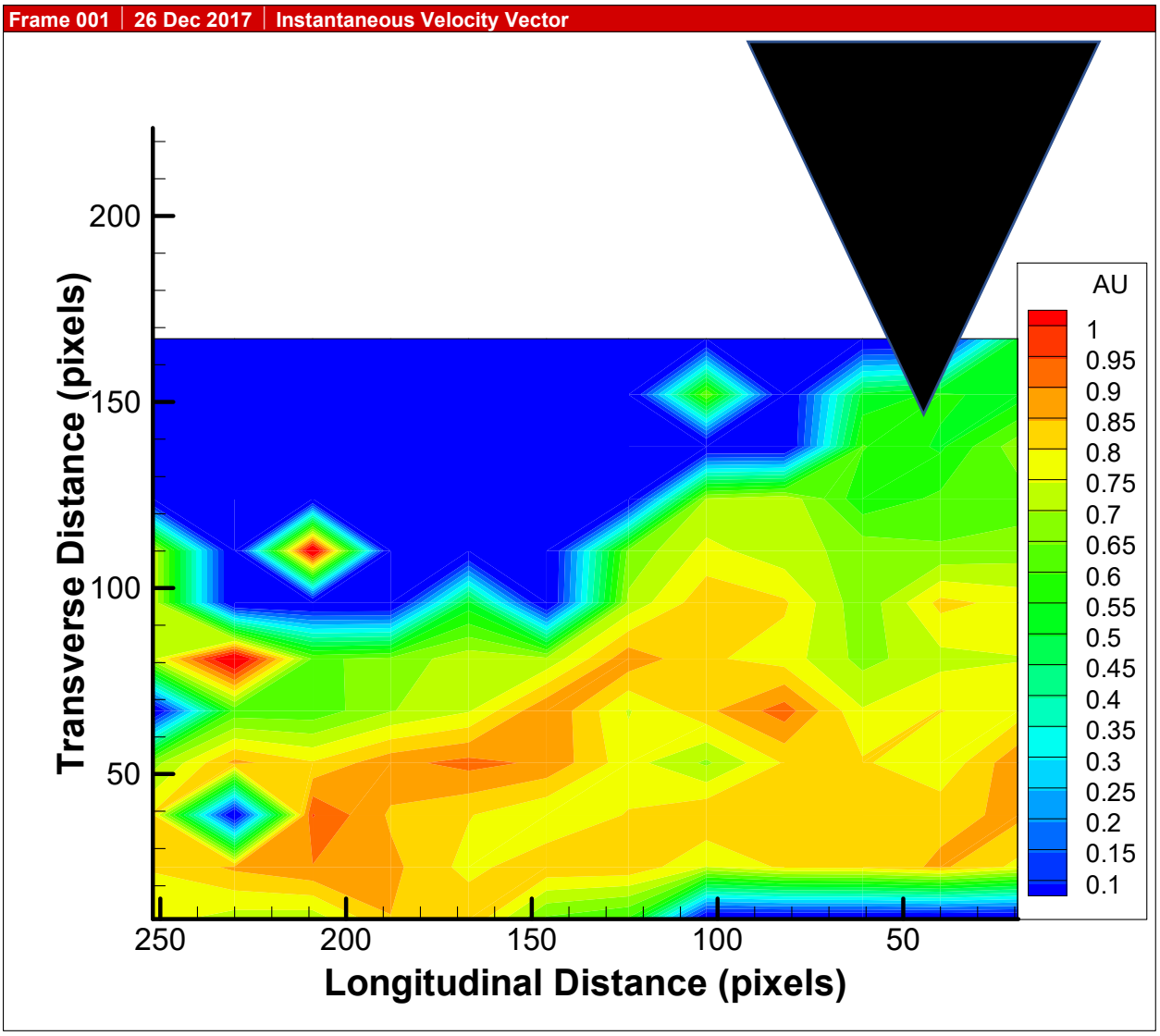

Figure D.10. LSIV results at 40 minutes elapsed.

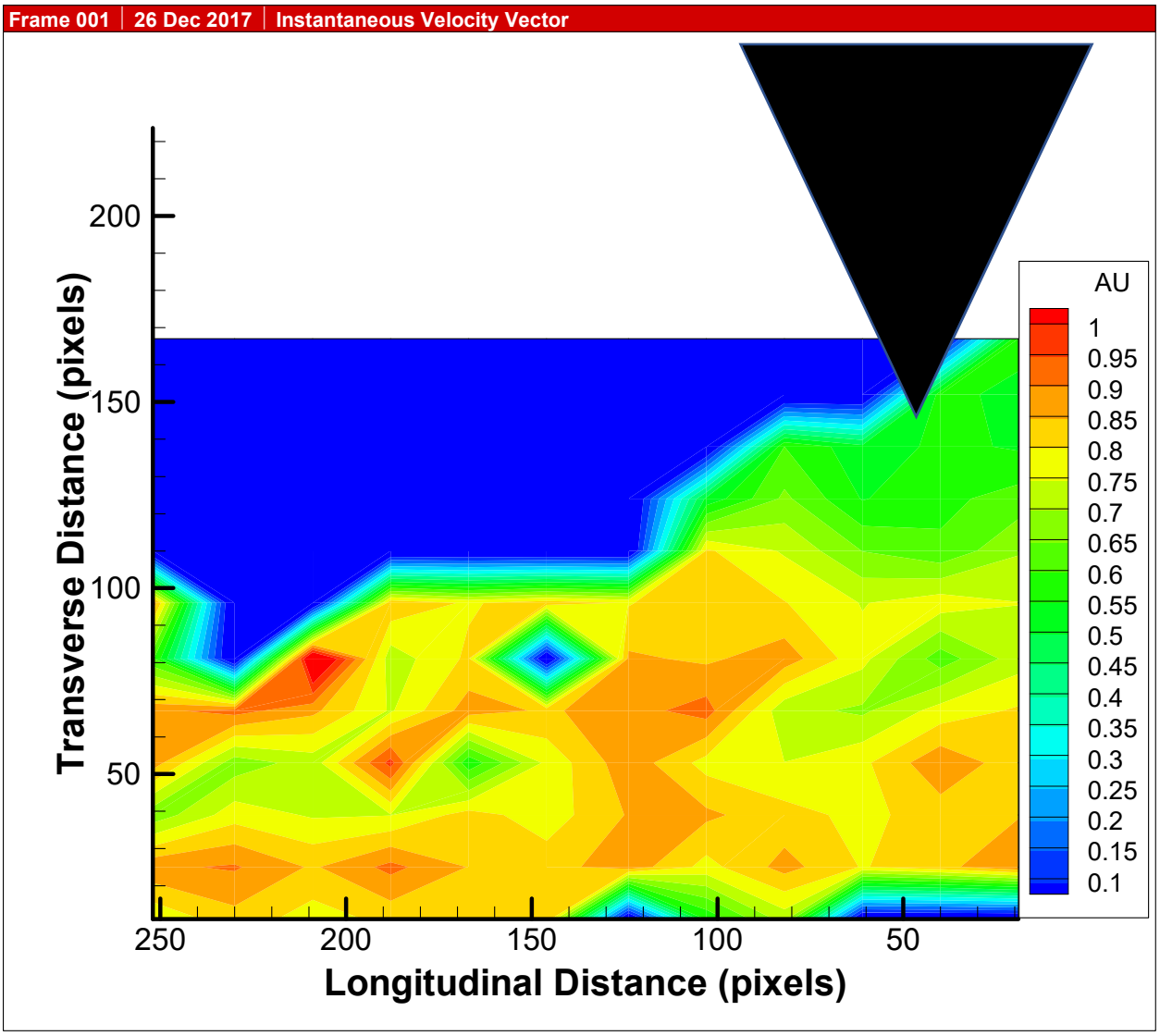

Figure D.11. LSIV results at 44 minutes elapsed.

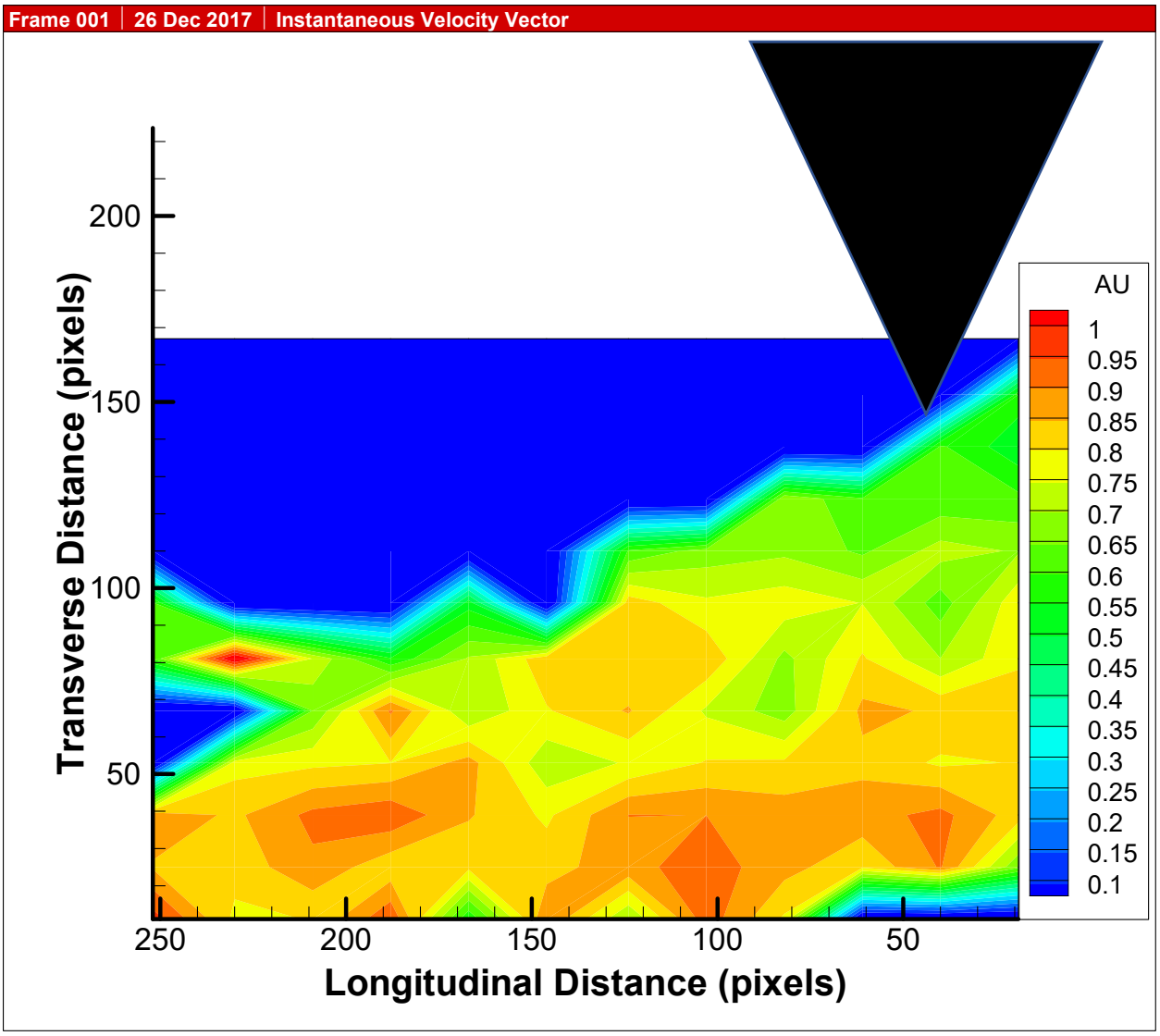

Figure. D.12. LSIV results at 50 minutes elapsed.

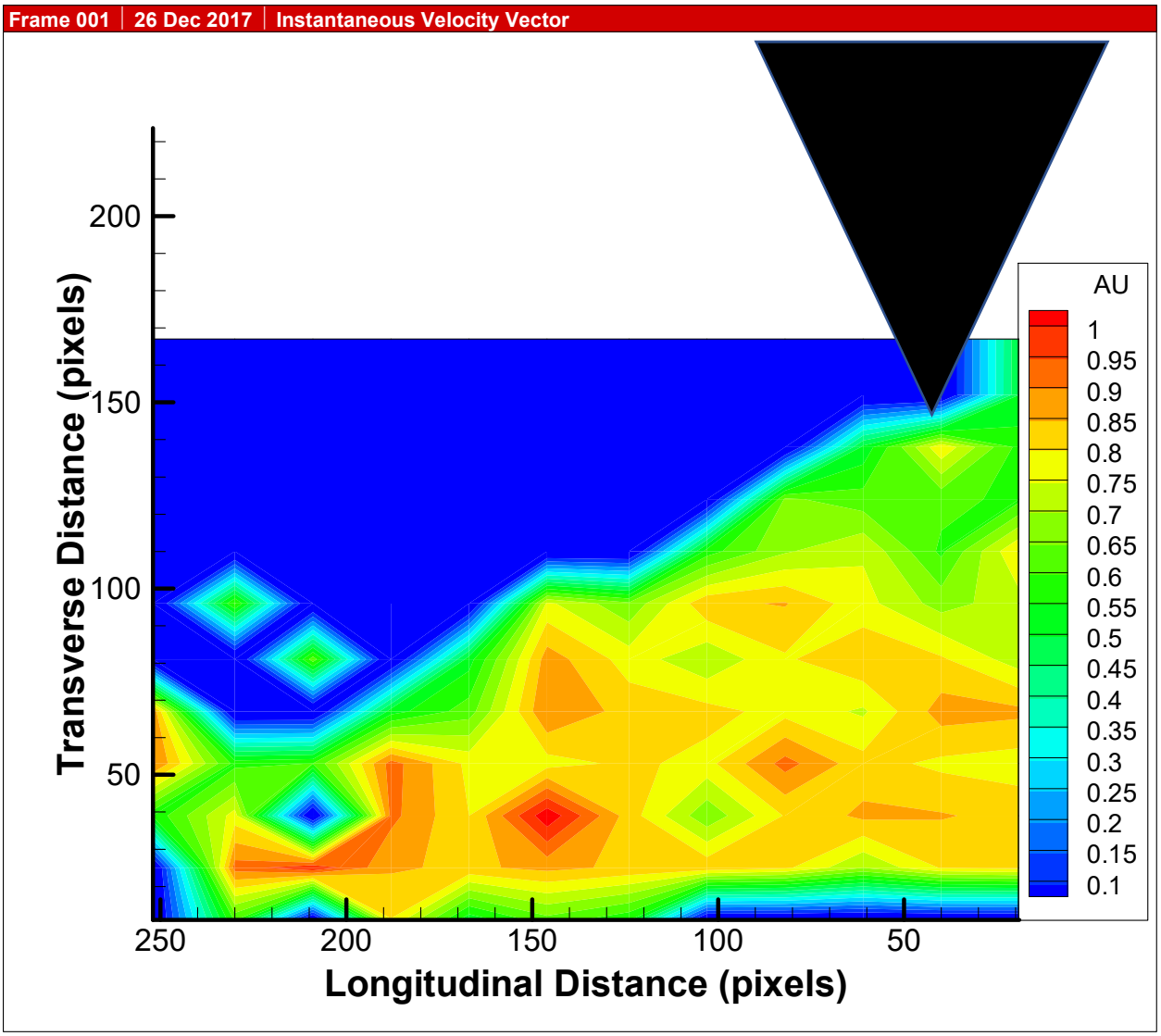

Figure D.13. LSIV results at 57 minutes elapsed

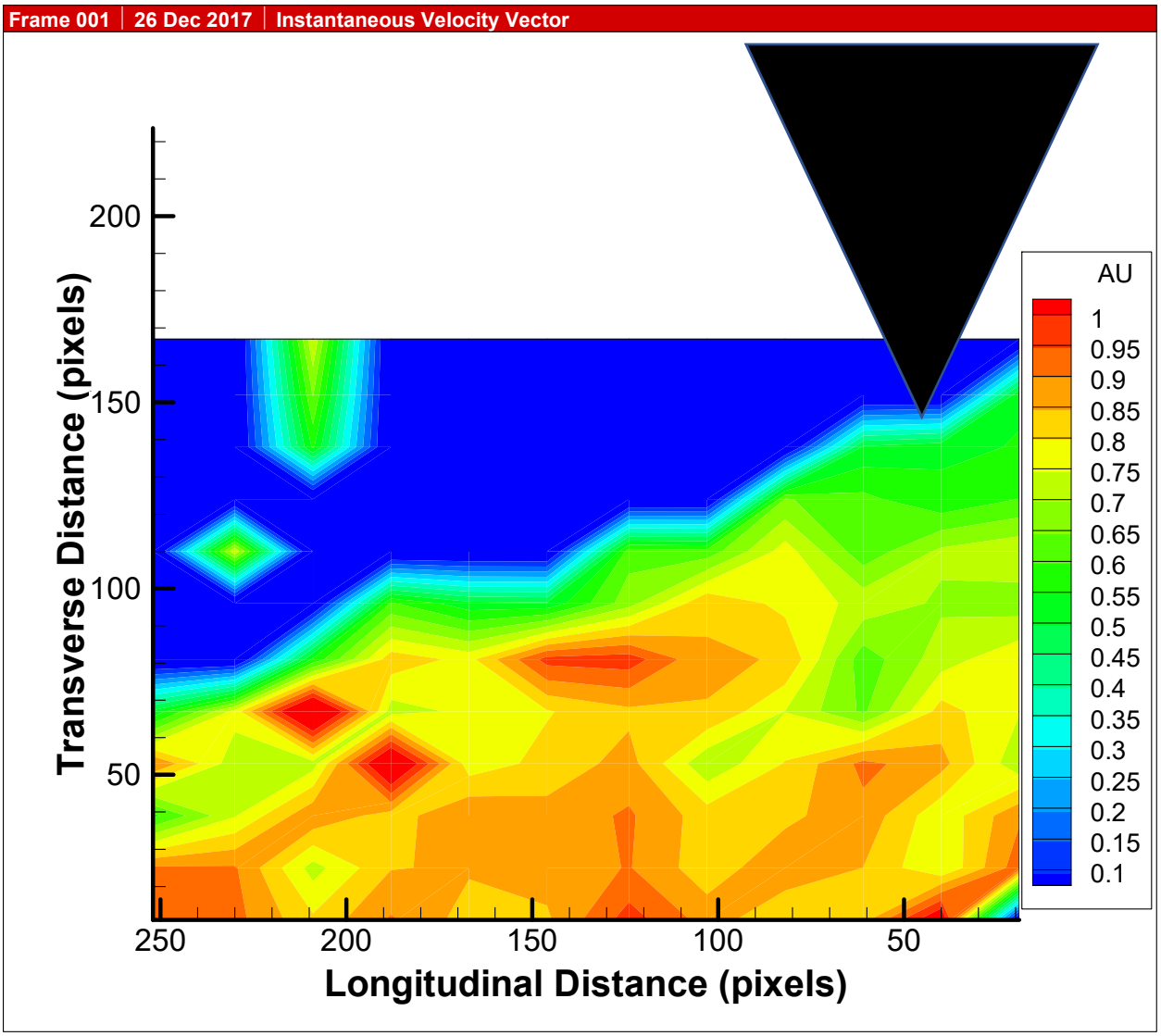

Figure D.14. LSIV results at 65 minutes elapsed.

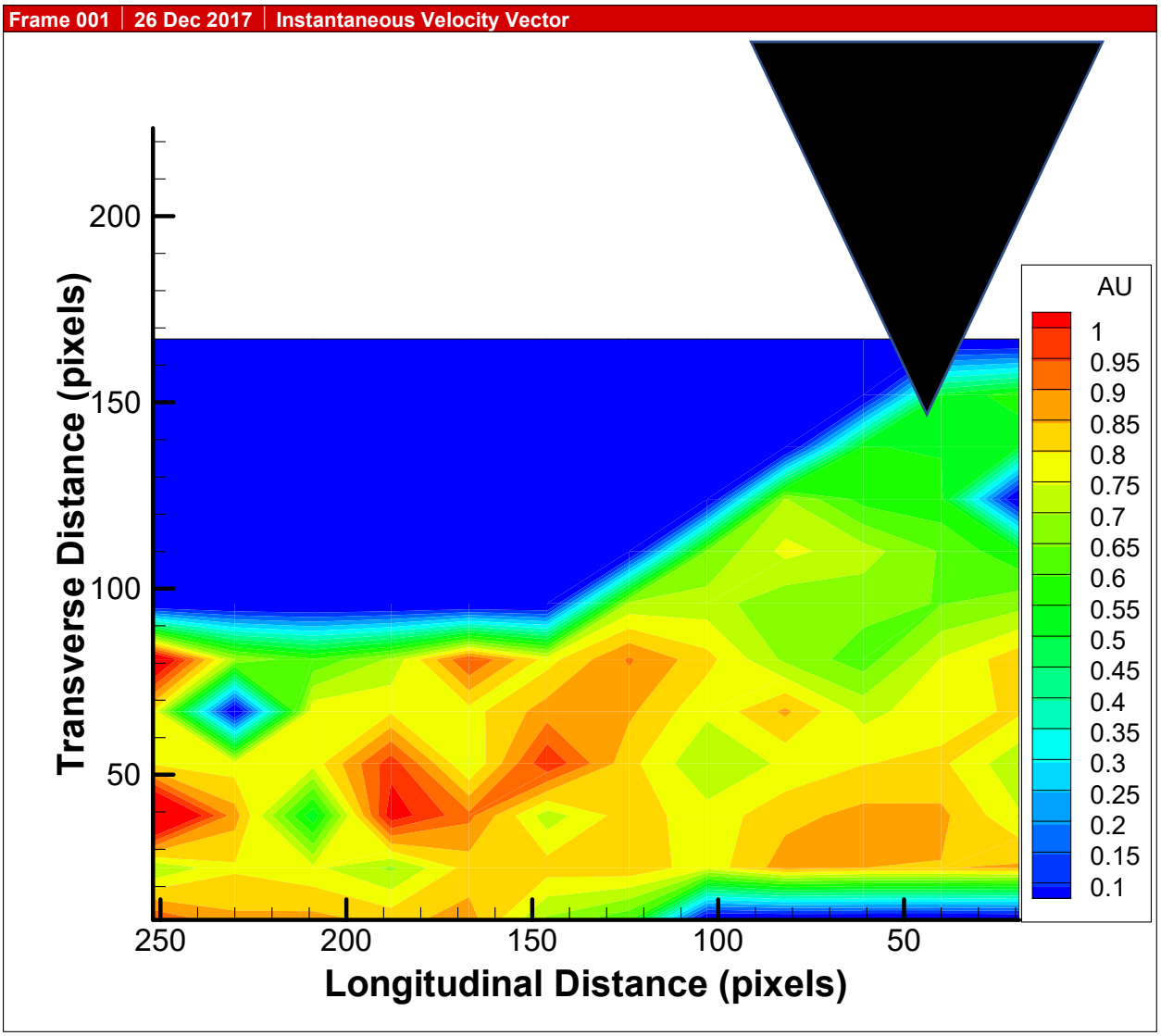

Figure D.15. LSIV results at 72 minutes elapsed

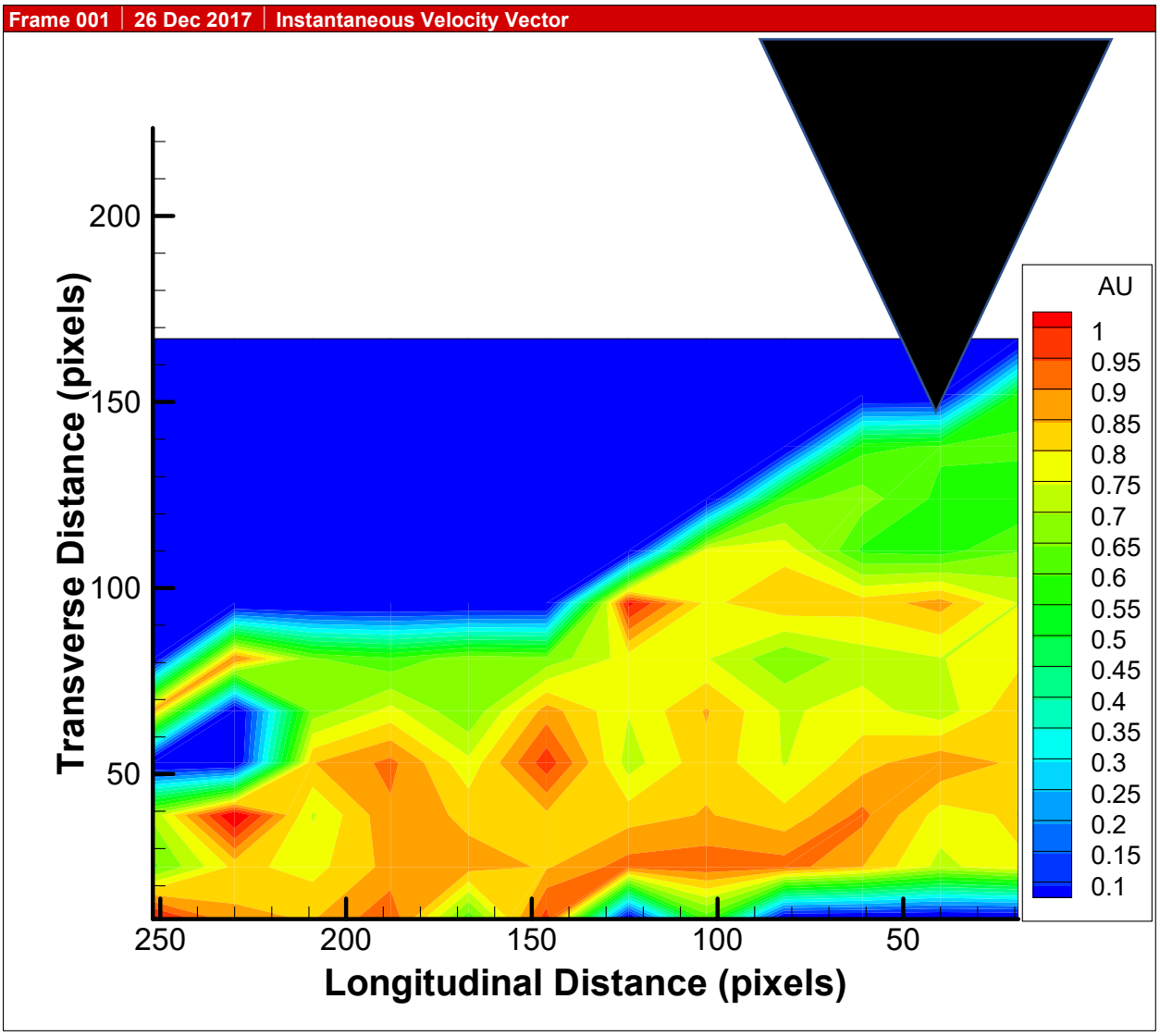

Figure D.15. LSIV results at 80 minutes elapsed

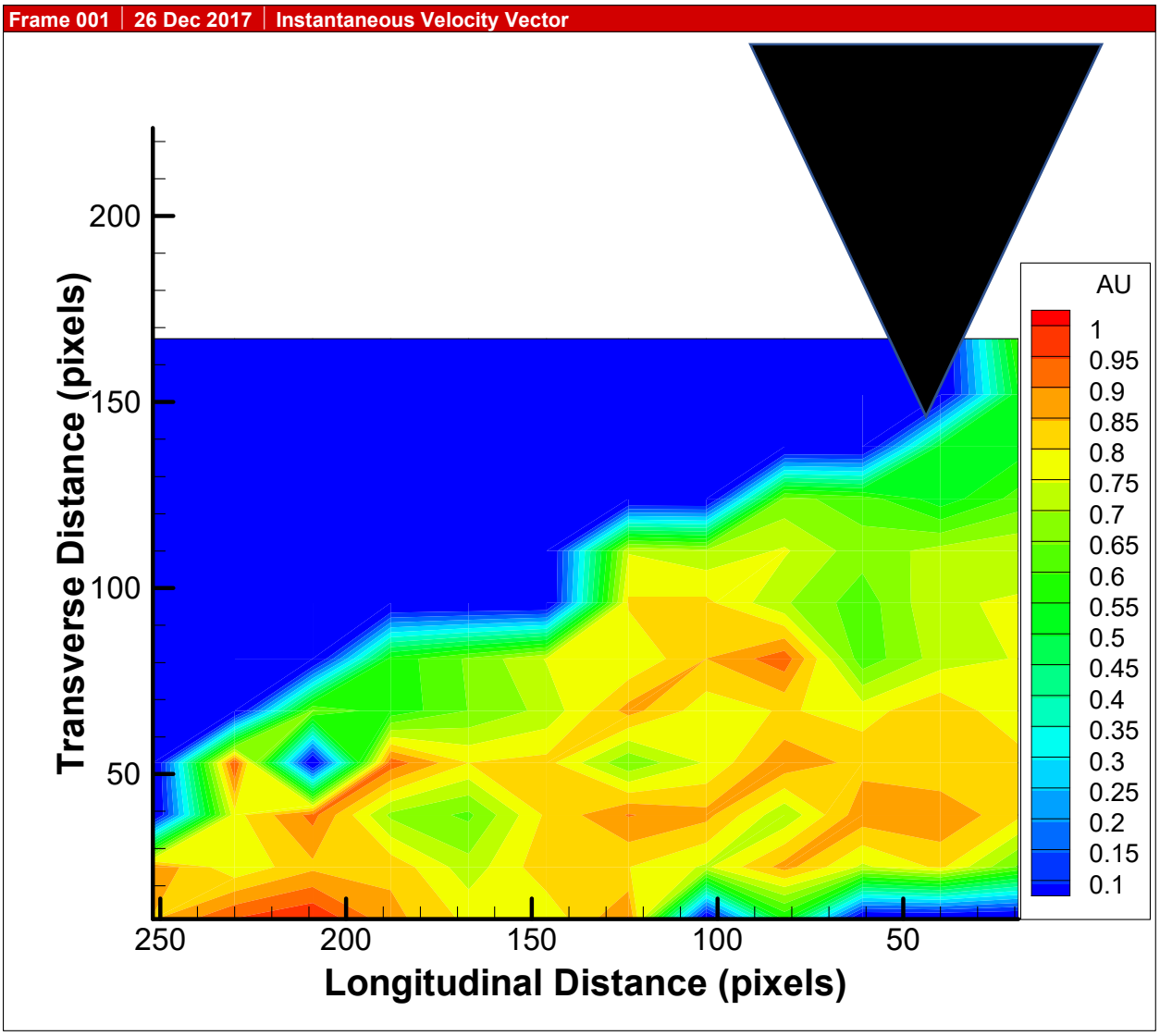

Figure D.16. LSIV results at 90 minutes elapsed

Appendix E: Decay function calculations.

Table E.1. Decay function calculations.

T_i (min)	T_i/T_t	Y (cm)	dY/dt (cm/min)	y (cm)	R_h (cm)	Y/Y_{max}	V (cm/s)	$\tau_{b,}$ (Pa)	τ_a	dτ/dt (Pa/min)	τ_*	τ_a/τ_{min}
0.0	0.00	0.0		9.1	6.20	0	65	5.06	8.79		0.067	1.945
2.5	0.03	1.2	0.50	10.3	6.47	26	58.7	5.76	7.07	0.689	0.054	1.564
6.3	0.07	3.3	0.54	12.3	6.84	68	54.7	6.88	6.02	0.278	0.046	1.333
9.8	0.11	3.8	0.15	12.9	6.92	79	53.9	7.17	5.82	0.057	0.044	1.289
13.5	0.15	3.5	-0.08	12.6	6.88	73	55.7	7.01	6.23	-0.109	0.047	1.379
17.0	0.19	3.3	-0.06	12.4	6.85	69	52.4	6.90	5.52	0.202	0.042	1.223
21.3	0.24	3.4	0.03	12.5	6.87	72	51.5	6.98	5.33	0.046	0.040	1.180
25.5	0.28	3.2	-0.05	12.3	6.84	68	56.4	6.87	6.40	-0.252	0.049	1.417
30.0	0.33	3.5	0.06	12.6	6.88	73	55.9	7.01	6.28	0.028	0.048	1.389
35.0	0.39	3.5	0.01	12.6	6.89	74	51.3	7.03	5.28	0.198	0.040	1.170
40.0	0.44	3.7	0.02	12.7	6.90	77	53.9	7.10	5.83	-0.109	0.044	1.290
44.0	0.49	3.9	0.06	13.0	6.94	81	52.4	7.23	5.50	0.082	0.042	1.217
50.0	0.56	3.0	-0.14	12.1	6.80	64	56.5	6.76	6.44	-0.156	0.049	1.424
57.0	0.63	3.8	0.11	12.9	6.93	80	50.6	7.20	5.13	0.187	0.039	1.135
65.0	0.72	3.7	-0.02	12.8	6.91	77	50.1	7.12	5.03	0.012	0.038	1.114
72.0	0.80	4.5	0.12	13.6	7.03	95	52	7.58	5.39	-0.051	0.041	1.193
80.0	0.89	4.7	0.03	13.8	7.07	99	52	7.70	5.38	0.001	0.041	1.191
90.0	1.00	4.8	0.00	13.8	7.07	100	50.1	7.72	5.00	0.039	0.038	1.106

Vita

Adam Thomas Merook was born on December 11th, 1992 in Sevierville, Tennessee, eventually growing up in Morristown, TN where he graduated from Morristown West High School in May 2011. Upon graduation, Mr. Merook attended the University of Tennessee at Knoxville where he participated in academic clubs, internships and undergraduate research under Dr. Dayakar Penumadu. After graduating Summa Cum Laude with a Bachelor of Science in Civil and Environmental Engineering in December 2015, Adam continued his education in graduate school under Dr. Thanos Papanicolaou at the Hydraulics and Sedimentation Laboratory studying open channel hydraulics, sediment transport, and gravel-bed rivers. Mr. Merook will receive his Masters of Science in Environmental Engineering in May 2018.